Pacific Northwest
NATIONAL LABORATORY

PNNL-39679

Power Fluidics & Online Spectroscopy for Reprocessing Plant: Development of Online Monitoring System (CRADA 605) Final Report

August 2026

Adan Schafer Medina
Heather M. Felmy
Tim P. Marrinan
Pratikshya Meher
Jason Rakos
Amanda M. Lines
Samuel A. Bryan
Stuart T. Arm

U.S. DEPARTMENT of ENERGY

Prepared for the U.S. Department of Energy
under Contract DE-AC05-76RL01830

DISCLAIMER

This report was prepared as an account of work sponsored by an agency of the United States Government. Neither the United States Government nor any agency thereof, nor Battelle Memorial Institute, nor any of their employees, makes **any warranty, express or implied, or assumes any legal liability or responsibility for the accuracy, completeness, or usefulness of any information, apparatus, product, or process disclosed, or represents that its use would not infringe privately owned rights**. Reference herein to any specific commercial product, process, or service by trade name, trademark, manufacturer, or otherwise does not necessarily constitute or imply its endorsement, recommendation, or favoring by the United States Government or any agency thereof, or Battelle Memorial Institute. The views and opinions of authors expressed herein do not necessarily state or reflect those of the United States Government or any agency thereof.

PACIFIC NORTHWEST NATIONAL LABORATORY
operated by
BATTELLE
for the
UNITED STATES DEPARTMENT OF ENERGY
under Contract DE-AC05-76RL01830

Printed in the United States of America

Available to DOE and DOE contractors from
the Office of Scientific and Technical Information,
P.O. Box 62, Oak Ridge, TN 37831-0062
www.osti.gov
ph: (865) 576-8401
fox: (865) 576-5728
email: reports@osti.gov

Available to the public from the National Technical Information Service
5301 Shawnee Rd., Alexandria, VA 22312
ph: (800) 553-NTIS (6847)
or (703) 605-6000
email: info@ntis.gov
Online ordering: http://www.ntis.gov

PNNL-39679

Power Fluidics & Online Spectroscopy for Reprocessing Plant: Development of Online Monitoring System (CRADA 605) Final Report

August 2026

Adan Schafer Medina
Heather M. Felmy
Tim P. Marrinan
Pratikshya Meher
Jason Rakos
Amanda M. Lines
Samuel A. Bryan
Stuart T. Arm

Prepared for
the U.S. Department of Energy
under Contract DE-AC05-76RL01830

Pacific Northwest National Laboratory
Richland, Washington 99354

CRADA Final Report Certification Memo

Memo Completion Date: 8/31/2026

CRADA Number: 605

CRADA Title: MODULAR POWER FLUIDICS AND ONLINE OPTICAL SPECTOSCOPY FOR REPROCESSING PLANT CONTROL AND ACCOUNTANCY

Responsible Technical Contact at DOE Lab (PNNL):

Stuart T. Arm

Provide a list of publications, conference papers, or other public releases of results, developed under this CRADA:

None

Provide a detailed list of all subject inventions, to include patent applications, copyrights, and trademarks:

No subject inventions were generated under this CRADA.

Summary

Integration of online monitoring (OLM) can have substantial benefits for process control, material accountancy, and upset avoidance in the reprocessing of used nuclear fuel. Results reported here highlight the development and integration of OLM into NuVision Engineering's Power Fluidics test rig to perform real-time mass balance. The set goal was to determine if mass balance uncertainty could be achieved within ±1% of the actual value. While required assumptions ultimately impact results, it was found that this uncertainty could be achieved under a variety of system conditions.

A variety of OLM tools could be leveraged for reprocessing needs. Work here focused on optical sensors capable of providing chemical composition analysis partnered with 2 different approaches to measure transferred mass of total solution, where the combination of data streams allowed for calculation of mass balance for a given dissolved species. Specifically visible absorbance spectroscopy was utilized to monitor the fingerprint of neodymium (Nd) as a surrogate for transuranics (e.g. Pu), and Raman spectroscopy was used to monitor nitrate as a surrogate for nitric acid. Both sensors could be utilized to monitor other species within a fuel reprocessing flowsheet. In both cases data science tools (chemometric models) were used to quantify concentration of dissolved species to feed into mass balance and uncertainty calculations. Total mass transferred was measured by either floor scales under receipt tanks or a flowmeter installed inline. Comparisons of resulting mass balance uncertainties when using either data stream are included in the discussion.

Notably, this project delivered the following advances:

- Developed and demonstrated novel designs for pilot scale optical sensors for monitoring the flowing process stream and for immersion into feed/receipt tanks. A novel flow cell design was developed to allow for cell switching in the case of needed referencing, maintenance, or replacement of components.

- Developed and demonstrated real-time data analysis tools for chemical concentration analysis ties to optical output at the pilot scale, with successful creation of data handling approaches that accounted for the flow behavior of the NuVision Power Fluidics system.

- Developed in-depth data fusion and handling tools that enabled mass balance calculation using multiple data feed streams. Most importantly, an advanced understanding of required assumptions regarding process parameters and progression was developed. This finding is perhaps the most valuable to industry moving forward, where better understanding these key parameters will enable innovation and acceleration of novel process control and material accountancy approaches.

In accordance with Requirements set forth in the terms of the CRADA (MODULAR POWER FLUIDICS AND ONLINE OPTICAL SPECTROSCOPY FOR REPROCESSING PLANT CONTROL AND ACCOUNTANCY, #605), this document is the CRADA Final Report, to be provided to PNNL Information Release who will forward to the DOE Office of Scientific and Technical Information as part of the commitment to the public to demonstrate results of federally

funded research. PNNL acknowledges that the CRADA parties (NuVision Engineering, Inc.) have been involved in the preparation of the report or reviewed the report.

Work here demonstrated the viability of partnering NuVision's Power Fluidics tools with PNNL's OLM capabilities. Further, toolkits were developed to accelerate deployment of OLM in the nuclear fuel reprocessing industry. Finally, the work highlighted key opportunities to advance knowledge in sensor integration. Examples of these opportunities include 1) advancing automated calibration tools and data science approaches to simplify deployment, 2) addressing calculation assumptions through pilot scale demonstration to accelerate pathways for industry utilization of automated mass balances, 3) further hardening of sensors and Power Fluidics approaches to improve applicability across variable operational conditions.

Acknowledgments

Research was supported by U.S. Department of Energy, Advanced Research Projects Agency–Energy (ARPA-E) and was performed at the Pacific Northwest National Laboratory (PNNL) operated by Battelle for the U.S. Department of Energy under Contract DE-AC05-76RL01830 as well as the NuVision test facility in Mooresville, North Carolina.

Acronyms and Abbreviations

ADVANCED Act	Accelerating Deployment of Versatile, Advanced Nuclear for Clean Energy Act
ALARA	As Low As Reasonably Achievable
AP-105	Hanford Tank AP-105
ARPA-E	Advanced Research Projects Agency–Energy
CCD	Charge-Coupled Device
CoDCon	Co-Decontamination (nuclear fuel reprocessing process)
CRS	Congressional Research Service
CSL	Continuous Sludge Leaching
CV	Cross validation
DOE	Department of Energy
GUM	The Guide to the Expression of Uncertainty in Measurement
HASQARD	Hanford Analytical Services Quality Assurance Requirements Documents
HEU	Highly enriched uranium
IC	Ion Chromatography
ICP	Inductively Coupled Plasma
LOD	Limit of detection
LWR	Locally Weighted Regression
MCS	Monte Carlo simulation
NIR	Near-Infrared
NTU	Nephelometric Turbidity Units
OLM	On-Line Monitoring
OOS	Online optical spectroscopy
PEP-WTP	Pretreatment Engineering Platform - Waste Treatment Plant
PF	Power fluidic
PFOOS	Power Fluidics and optical online spectroscopy
PLS	Partial Least Squares
PNNL	Pacific Northwest National Laboratory
PVC	Polyvinyl Chloride
QA/QC	Quality Assurance / Quality Control
RMSEC	Root-Mean-Square Error of Calibration
RMSECV	Root-Mean-Square Error of Cross-Validation
RMSEP	Root-Mean-Square Error of Prediction
SBIR	Small business innovative research
SNF	Spent Nuclear Fuel
SOW	Statement of Work

SPE	Standard prediction error
SSI	Spectra Solutions Inc.
SST	Single Shell Tank
TBP	Tributyl Phosphate
TIC/TOC	Total inorganic/organic carbon
TRL	Technology Readiness Level
UQ	Uncertainty quantification
UV-vis	Ultraviolet-Visible Spectroscopy
WTP	Waste Treatment Plant

Contents

Summary iii
Acknowledgments vi
Acronyms and Abbreviations vii
1.0 Introduction 8
1.1 Background: Previous PNNL Advancement of Sensor Hardware 9
1.1.1 Data Science for Automated Quantification: Chemometric methodology 9
1.1.2 PNNL past demonstrations in comparable process scales: Hanford waste applications 10
1.1.3 Taking Sensors into a High-Radiation Environment: notes on previous studies on radiation effects 11
1.1.4 Previous advancements of probe design for turbid solutions 13
1.1.5 Demonstration of enabling real-time, manual process control in nuclear fuel reprocessing 13
2.0 Hardware and Equipment 15
2.1 Spectrometers 15
2.2 Probes and Sensor Systems 15
2.2.1 The parallel cell: innovating mitigation strategies for realistic operations 16
2.2.2 Immersion probes 17
3.0 Design of Experiments 19
3.1 Success criteria 19
3.2 Surrogate test material 19
3.3 Test configuration 20
4.0 Automating Data Analysis and Chemometric Analysis 22
4.1 Data acquisition and model parameters 22
4.2 Small-scale chemometric modeling 23
4.3 Deployment of sensors 27
5.0 Materials Accountancy and Uncertainty 43
5.1 Problem definition 43
5.1.1 Analyte-specific mass balance 44
5.1.2 Mass balance error 45
5.2 Uncertainty quantification background 45
5.2.1 GUM 46
5.2.2 Floor scale uncertainty model 48

5.2.3 Monte Carlo simulation 49
5.2.4 Combining uncertainties 54
5.3 Measurement consistency 55
5.3.1 The Birge ratio 56
5.3.2 Combining independent measurements 57
5.4 Chemometric modeling 58
5.4.1 Partial least squares regression 58
5.5 Strategies for invalid measurements 61
5.5.1 Masking strategies 63
5.5.2 Imputation strategies 63
5.5.3 Resampling strategy 64
5.6 Uncertain quantities 64
6.0 Materials Accountancy and Uncertainty Analysis Results 68
6.1 Overview of the mass transfer uncertainty analysis for Nd^{3+} 68
6.2 Overview of the mass transfer uncertainty analysis for NO_3^- 72
6.3 Overview of the total mass transfer uncertainty analysis 73
6.4 Mass measurement comparison 75
6.5 Example UQ Output 76
6.6 Analysis of Monte Carlo Simulations 81
7.0 Conclusions and Next Steps 85
8.0 References 87
Appendix A – Supplementary Optical Data A.1
Appendix B – Additional Uncertainty Analysis B.33

Figures

Figure 1. Raman spectra of real AP-105 tank waste at multiple flow rates and resulting chemometric results from flow test. 10
Figure 2. A) Photo of the S-109 on-line monitoring system during acceptance testing. B) Computer display showing real-time composition during S-109 retrieval testing. 11
Figure 3. A) Quartz cuvettes irradiated within PNNL's gamma facility showing the relative darkening of the optical components as a function of dose. The total accumulated dose showing a range of dose from 0 rad (far left) to 1.7×10^8 rad (far right). B) Measured nitrate concentration as a function of applied dose to probe optics, for various simulated wastes. 12

Figure 4. The percent composition of U and Pu in the aqueous product stream during CoDCon run....14
Figure 5. Schematic diagram of the power fluidic system and integrated Raman and UV-vis sensors....16
Figure 6. Photo of deployed parallel cells at NuVision Engineering....17
Figure 7. Calibration set spectra collected on cell 1 for A) Raman B) UV-vis. The primary NO_3^- Raman peak is shown in the inset....23
Figure 8. Preprocessed spectra collected on cell 1 for A) Raman and B) UV-vis for the calibration and test datasets along with the corresponding parity plots of known vs. PLS model measured concentration of C) NO_3^- from Raman and D) Nd^{3+} from UV-vis....24
Figure 9. Parity plots showing the model results comparing the calibration dataset collected on cell 1 to validation data collected on cells 2-4 and the immersion probes for A) NO_3^- from Raman and B) Nd^{3+} from UV-vis before applying a slope and intercept correction to the models, and the model results for C) NO_3^- from Raman and D) Nd^{3+} from UV-vis after applying a slope and intercept correction to the models for cells 2-4 and the immersion probe....25
Figure 10. Flowing solution test showing the normalized and baseline corrected Raman spectra for A) cell 1, B) cell 3, and C) cell 4 along with the corresponding target vs. model measured nitrate concentrations for D) cell 1, E) cell 3, and F) cell 4....26
Figure 11. Flowing solution test showing the baseline corrected UV-vis spectra for A) cell 1, B) cell 3, and C) cell 4 along with the corresponding target vs. model measured neodymium concentrations for D) cell 1, E) cell 3, and F) cell 4....27
Figure 12. UV-vis spectra of the standard addition solutions with a first derivative applied for the A) calibration, C) surrogate, E) first dilution, and G) second dilution solutions. The univariate calibration curves of absorbance at 795 nm vs. added Nd^{3+} concentration used for the determination of the initial Nd^{3+} concentration for B) calibration, D) surrogate, F) first dilution, and H) second dilution solutions....29
Figure 13. Raman spectra of the standard addition solutions with a first derivative applied for the A) calibration, C) surrogate, E) first dilution, and G) second dilution solutions. The univariate calibration curves of absorbance at 1022 cm^{-1} vs. added NO_3^- concentration used for the determination of the initial NO_3^- concentration for B) calibration, D) surrogate, F) first dilution, and H) second dilution solutions....30
Figure 14. A) Raman spectra collected on cell 1 measuring the blank solution and calibration solution. B) Top-down view of the Raman spectra. C) Reduced Q residuals of the model....31
Figure 15. A) Raman spectra collected on cell 1 measuring the blank solution and calibration solution after the removal of spectra with reduced Q residuals

>50. B) Top-down view of the Raman spectra. C) Model results showing the measured nitrate concentration. 32

Figure 16. UV-vis model results for Nd^{3+} concentration measured across the blank and calibration solutions at the start of the first week of tank transfers and used for the slope and intercept correction. The model measured Nd^{3+} concentration is shown before and after the correction was applied to the models. 33

Figure 17. UV-vis model results for Nd^{3+} concentration measured across a partial tank transfer of the undiluted surrogate before and after the slope and intercept correction was applied to the models. 34

Figure 18. Raman model results for calibration solution NO_3^- concentration measured across the blank and calibration solutions at the start of the first week of tank transfers and used for the slope and intercept correction. The model measured NO_3^- concentration is shown before and after the correction was applied to the models. 35

Figure 19. Raman model results for surrogate solution NO_3^- concentration measured across a partial tank transfer of the undiluted surrogate before and after the slope and intercept correction was applied to the models. 36

Figure 20. UV-vis model results for Nd^{3+} concentration measured across the blank and calibration solutions at the start of the second week of tank transfers and used for the slope and intercept correction. The model measured Nd^{3+} concentration is shown before and after the correction was applied to the models. 37

Figure 21. UV-vis model results for Nd^{3+} concentration measured across a partial tank transfer of the first dilution of the surrogate before and after the slope and intercept correction was applied to the models. 37

Figure 22. UV-vis model results for Nd^{3+} concentration measured across a partial tank transfer of the second dilution of the surrogate before and after the slope and intercept correction was applied to the models. 38

Figure 23. Raman model results for calibration solution NO_3^- concentration measured across the blank and calibration solutions at the start of the second week of tank transfers and used for the slope and intercept correction. The model measured NO_3^- concentration is shown before and after the correction was applied to the models. 39

Figure 24. Raman model results for surrogate solution NO_3^- concentration measured across a partial tank transfer of the first dilution of the surrogate before and after the slope and intercept correction was applied to the models. 40

Figure 25. Raman model results for surrogate solution NO_3^- concentration measured across a partial tank transfer of the second dilution of the surrogate before and after the slope and intercept correction was applied to the models. 41

Figure 26. Floor scales under the supply and receipt tanks were calibrated by standardizing readings to those of a third scale measuring a fixed, known volume of water. The blue curve represents the raw combined mass

measured by both floor scales during one full-tank transfer and the orange curve represents the combined readings after calibration-correction. 49
Figure 27. Monte Carlo simulation perturbation bounds of Raman data for Track 01 (upper left), Track 03 (lower left), Track 04 (upper right), and Track 05 (lower right). 51
Figure 28. Monte Carlo simulation perturbation bounds of UV-vis data for Track 01 (upper left), Track 03 (lower left), Track 04 (upper right), and Track 05 (lower right). 52
Figure 29. Model predictions of NO_3^- concentration for measured spectra (blue) and mean model predicted NO_3^- concentration for 100 perturbations (yellow). 53
Figure 30. Model predictions of Nd^{3+} concentration for measured spectra (blue) and mean model predicted Nd^{3+} concentration for 100 perturbations (yellow). 54
Figure 31. Trial 1 – Repetition 1 Nd^{3+} cumulative mass transferred (top) and relative standard uncertainty (bottom). 70
Figure 32. Trial 4 – Repetition 2 Nd^{3+} cumulative mass transferred (top) and relative standard uncertainty (bottom). 71
Figure 33. Mass measurement options for $\mathrm{Nd3}+$using no mask (left) and associated relative uncertainty (right). 75
Figure 34. Mass measurement options for $\mathrm{NO3}-$ using no mask (left) and associated relative uncertainty (right). 76
Figure 35. Q-residual analysis for $\mathrm{NO3}-$. 81
Figure 36. Q-residual analysis for $\mathrm{Nd3}+$. 82
Figure 37. Hotelling $T2$ statistic analysis for $\mathrm{NO3}-$. 83
Figure 38. Hotelling $T2$statistic analysis for $\mathrm{Nd3}+$. 83
Figure 39. Drive phase mask analysis for $\mathrm{NO3}-$. 84
Figure 40. Drive phase mask analysis for $\mathrm{Nd3}+$. 84
Figure 41. UV-vis Trial 1: Full tank transfer, 2.3 Bar, 3 replicates A.1
Figure 42. Raman Trial 1: Full tank transfer, 2.3 Bar, 3 replicates A.2
Figure 43. UV-vis Trial 2: Full tank transfer, 1.0 Bar, 3 replicates A.3
Figure 44. Raman Trial 2: Full tank transfer, 1.0 Bar, 3 replicates A.4
Figure 45. UV-vis Trial 3: Full tank transfer, 2.3 Bar, 2.0 Bar, 1.0 Bar A.5
Figure 46. Raman Trial 3: Full tank transfer, 2.3 Bar, 2.0 Bar, 1.0 Bar A.6
Figure 47. UV-vis Trial 4: First third tank transfer, 2.3 Bar, 2.0 Bar, 1.0 Bar A.7
Figure 48. Raman Trial 4: First third tank transfer, 2.3 Bar, 2.0 Bar, 1.0 Bar A.8
Figure 49. UV-vis Trial 5: Second third tank transfer, 2.3 Bar, 2.0 Bar, 1.0 Bar A.9
Figure 50. Raman Trial 5: Second third tank transfer, 2.3 Bar, 2.0 Bar, 1.0 Bar A.10
Figure 51. UV-vis Trial 6: Recirc on/off 1.0 Bar A.11
Figure 52. Raman Trial 6: Recirc on/off 1.0 Bar A.12

Figure 53. UV-vis Trial 7: Dilution 1, Full tank transfer, 2.3 Bar, 3 replicates A.13
Figure 54. Raman Trial 7: Dilution 1, Full tank transfer, 2.3 Bar, 3 replicates A.14
Figure 55. UV-vis Trial 8: Dilution 1, Full tank transfer, 2.3 Bar, 2.0 Bar, 1.0 Bar.....A.15
Figure 56. Raman Trial 8: Dilution 1, Full tank transfer, 2.3 Bar, 2.0 Bar, 1.0 Bar A.16
Figure 57. UV-vis Trial 9: Dilution 1, First third tank transfer, 2.3 Bar 3 replicates A.17
Figure 58. Raman Trial 9: Dilution 1, First third tank transfer, 2.3 Bar 3 replicates.....A.18
Figure 59. UV-vis Trial 10: Dilution 1, Second third tank transfer, 2.3 Bar 3 replicates A.19
Figure 60. Raman Trial 10: Dilution 1, Second third tank transfer, 2.3 Bar 3 replicates A.20
Figure 61. UV-vis Trial 11: Dilution 2, Full tank transfer, 2.3 Bar, 3 replicates.....A.21
Figure 62. Raman Trial 11: Dilution 2, Full tank transfer, 2.3 Bar, 3 replicates A.22
Figure 63. UV-vis Trial 12: Dilution 2, Full tank transfer, 2.3 Bar, 2.0 Bar, 1.0 Bar.....A.23
Figure 64. Raman Trial 12: Dilution 2, Full tank transfer, 2.3 Bar, 2.0 Bar, 1.0 Bar A.24
Figure 65. UV-vis Trial 13: Dilution 2, First third tank transfer, 2.3 Bar, 3 replicates A.25
Figure 66. Raman Trial 13: Dilution 2, First third tank transfer, 2.3 Bar, 3 replicates.....A.26
Figure 67. UV-vis Trial 14: Dilution 2, Second third tank transfer, 2.3 Bar, 3 replicates A.27
Figure 68. Raman Trial 14: Dilution 2, Second third tank transfer, 2.3 Bar, 3 replicates A.28
Figure 69. UV-vis Trial 15: Dilution 2, First third tank transfer, 2.3 Bar, 2.0 Bar, 1.0 Bar.....A.29
Figure 70. Raman Trial 15: Dilution 2, First third tank transfer, 2.3 Bar, 2.0 Bar, 1.0 Bar.....A.30
Figure 71. UV-vis Trial 16: Dilution 2, Second third tank transfer, 2.3 Bar, 2.0 Bar, 1.0 Bar.....A.31
Figure 72. Raman Trial 16: Dilution 2, Second third tank transfer, 2.3 Bar, 2.0 Bar, 1.0 Bar.....A.32
Figure 73. Mass measurement options for $Nd3+$ using the concentration bound and spike mask (left) and associated relative uncertainty (right). B.33
Figure 74. Mass measurement options for $NO3-$ using the concentration bound spike mask (left) and associated relative uncertainty (right). B.33
Figure 75. Mass measurement options for $Nd3+$using the power fluidics phase mask (left) and associated relative uncertainty (right). B.34
Figure 76. Mass measurement options for $NO3-$ using the power fluidics phase mask (left) and associated relative uncertainty (right).....B.34
Figure 77. Mass measurement options for $Nd3+$ using the Monte Carlo std. mask (left) and associated relative uncertainty (right). B.34

Figure 78. Mass measurement options for NO3 − using the Monte Carlo std. mask (left) and associated relative uncertainty (right). B.35
Figure 79. Mass measurement options for Nd3 + using the Q-residual threshold mask (left) and associated relative uncertainty (right). B.35
Figure 80. Mass measurement options for NO3 − using the Q-residual threshold mask (left) and associated relative uncertainty (right). B.35
Figure 81. Mass measurement options for Nd3 + using the concentration bound, PLS stats, and Monte Carlo std. masks combined (left) and associated relative uncertainty (right). B.36
Figure 82. Mass measurement options for NO3 − using the concentration bound, PLS stats, and Monte Carlo std. masks combined (left) and associated relative uncertainty (right). B.36

Tables

Table 1. Summary of PNNL-SA-211652 Memorandum of Simulant formulation. 20
Table 2. Consolidated test matrix. 21
Table 3. Model statistics for Raman and UV-vis collected on cell 1 including the RMSE values, R^2 values, and LODs. 24
Table 4. Solution concentrations determined by standard addition. 31
Table 5. Details of UV-vis and Raman tank transfer plots included in Appendix A. 42
Table 6. Masking strategies 63
Table 7. Imputation strategies 64
Table 8. Resampling strategies 64
Table 9. Scale uncertainty sources. 64
Table 10. Flowmeter uncertainty sources. 65
Table 11. PLS spectroscopy uncertainty sources. 65
Table 12. Lab measurement uncertainty sources. 66
Table 13. Concentration drift uncertainty sources. 66
Table 14. Density uncertainty sources. 66
Table 15. Combination and reconciliation uncertainty sources. 66
Table 16. Uncertainty sources grouped by category. 67
Table 17. Nd3 +estimated transferred mass and relative uncertainty. 68
Table 18. Trial 1 – Repetition 1 uncertainty budget for Nd^{3+} mass transfer. 70
Table 19. Trial 4 – Repetition 2 uncertainty budget for Nd^{3+} mass transfer. 71
Table 20. NO3 − estimated transferred mass and relative uncertainty. 72
Table 21. Estimated total transferred mass and relative uncertainty. 74

1.0 Introduction

The United States currently has no permanent spent nuclear fuel (SNF) repositories leading to a backlog of 91,000 metric tons at powerplants as of December 2022. Additionally, there is a yearly increase of approximately 2,200 metric tons of SNF each year. Furthermore, there is an increasing interest in advanced reactors, such as those using highly enriched uranium (HEU), or fast reactors that can burn transuranics. Overall, this has led to a changing paradigm where recycling used nuclear fuel can offer much-needed solutions to both powering the reactors of the future and mitigating the heat loading of wastes that have challenged repositories for several decades.

While industry interest in recycling used nuclear fuel is rapidly growing, deployment of plants is still limited by economic concerns and questions about effectively addressing safeguards requirements. On-line monitoring (OLM) has been presented as a critical, cost-effective tool for probing SNF processing streams for the purposes of real-time process control and material accountancy. Various sensors and tools can provide a wide range of information, including flowrate, density, concentration, and redox state.(Tse et al. 2024) Depending on target application and process stream conditions (e.g. aqueous process vs molten salt) sensors are at different technology readiness levels (TRL) and market availability.

This report focuses on the advancement and scale up of one of the highest TRL options for online monitoring and completion of real-time mass balances within a surrogate processing environment. Specifically, this report details the integration of pilot scale optical spectroscopy sensors and corresponding flow/total mass measurements partnered with NuVision's Power Fluidics pilot plant. Optical spectroscopy is well suited to quantifying actinides and monitoring process conditions, and it can be flexibly applied across a range of process scales and types.(Hope E. Lackey et al. 2024; Heather M. Felmy et al. 2026; Samuel A. Bryan et al. 2013; Branch et al. 2023; Lines et al. 2018) Partnering these optical measurements with flow data for mass balance enables a safe and effective mechanism to simultaneously measure f-element concentrations across a process, from inlet to outlet feeds, through chemometric modeling and calibration transfers.(Tse et al. 2025) Furthermore, demonstrating optical online spectroscopy (OOS) alongside NuVision's Power Fluidics allows for testing and developing sensors that can work effectively in a representative flow environment. In this instance, application to aqueous process systems was completed, however translation of tool kits to alternative matrices is a viable focus of future work and would further advance and enable the fuel recycle industry.

Here optical sensors included visible absorbance and Raman spectroscopies. Vis spectroscopy has been used to follow U and various actinides under previous efforts.(Heather M. Felmy et al. 2023; Tse et al. 2024; Lines, Hall, et al. 2020b) Neodymium (Nd) was used as a non-rad surrogate for demonstration. Raman Spectroscopy was also used and has been leveraged to follow polyatomic actinides (e.g. uranyl), nitric acid, total nitrate, various ligands, and even pH in previous efforts.(Heather M. Felmy et al. 2023; H. E. Lackey et al. 2020; Serrano et al. 2025; Heather M. Felmy et al. 2026) Here, $NaNO_3$ was used as a surrogate for nitric acid. Total mass transferred between vessels was measured by scales, and flow was measured by flow meters. Mass balances were calculated using either and both data streams to compare resulting uncertainties.

The primary objective of this effort was to demonstrate that an uncertainty of ±1% could be obtained for a mass balance via online monitoring. While demonstrating this, the team also

advanced optical sensor design, data science approaches that were adaptive to the NuVision Power Fluidics flow profiles, and a comprehensive understanding of the operational assumptions that need to be addressed to enable industry to complete real-time mass balances with accurate uncertainty propagation.

Section 1 of the report discusses PNNL's previous work on sensor hardware and advanced automated tools. Section 2 discusses the hardware and equipment used to integrate the optical OLM tools for this work. Section 3 describes the design of experiment. Section 4 describes this work's advancement of the automated data analysis tools, including chemometric modeling, sensor deployment, and data collection. Section 5 discusses the uncertainty analysis for the mass balance. Section 6 covers the results of the mass balance uncertainty calculations. Section 7 provides concluding remarks and next step recommendations for this work. A companion report from Nuvision Engineering will discuss the set-up and operation of the Power Fluidics Online Optical Spectroscopy test rig.

1.1 Background: Previous PNNL Advancement of Sensor Hardware

To better provide context for the current TRL and the impact of advances under the ARPA-E efforts, the following sections provide a background on the current state of the art in optical monitoring.

1.1.1 Data Science for Automated Quantification: Chemometric methodology

The general methodology for quantitative prediction of nuclear fuel reprocessing and related waste components from optical spectroscopic measurements is based on the unique signatures associated with each analyte of interest.(Lines et al. 2019)

PNNL has demonstrated the development and application of chemometric models to the analysis of complex streams exhibiting spectral data challenges expected in reprocessing streams including confounding (overlapping) bands and matrix-dependent speciation.(S. A. Bryan et al. 2011; Lines et al. 2017; Lines et al. 2018; Nelson, Lines, et al. 2018; Lines et al. 2019) In general, chemometric modeling approaches are utilized where these well-documented and well understood mathematical approaches are commonly used in pharmaceutical and food processing industry where trust and verification of results is crucial. These algorithms also come with well documented methods to calculate metrics and uncertainties, making them ideal for the nuclear industry where regulatory review requires verification and trust.

These data science tools are capable of handling significant complexity. As an example, a previous application to inline and real-time monitoring of a real Hanford tank AP-105 supernate sample is provided. Here, solution was pumped in a closed, bench-scale loop through the monitoring flow cell. Raman spectra were collected while the pump flow rate was varied from 0 mL/min to 35.6 mL/min in various stages. Spectral signatures did not vary over these flow regimes and are shown in Figure 1A. Chemometric models were applied on the spectra collected in real-time and is displayed in Figure 1B.(Lines et al. 2019)

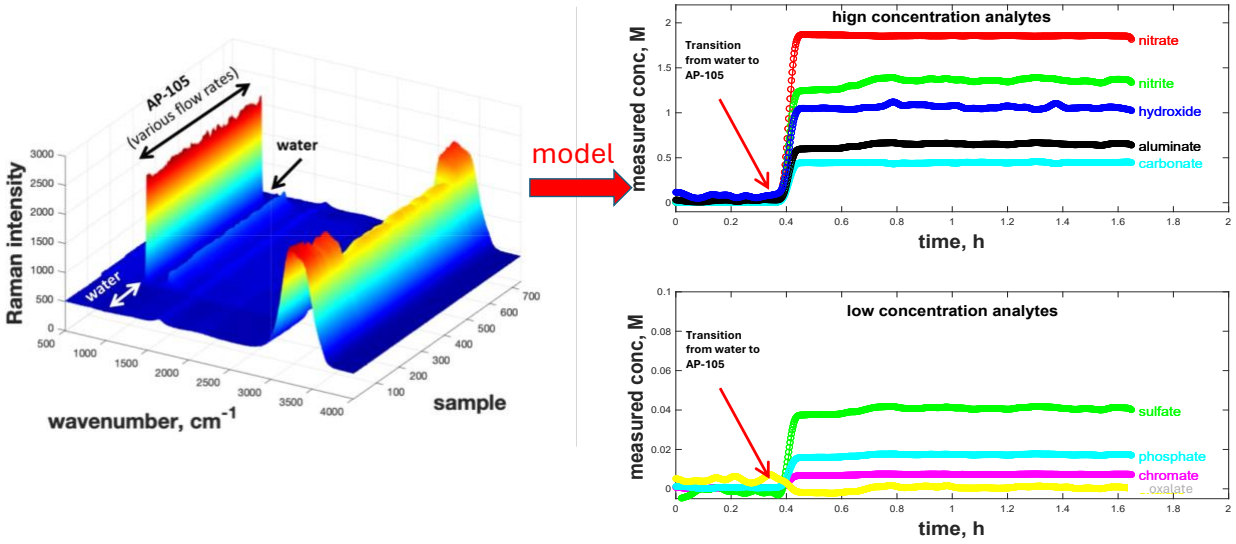


Figure 1. Raman spectra of real AP-105 tank waste at multiple flow rates and resulting chemometric results from flow test.

1.1.2 PNNL past demonstrations in comparable process scales: Hanford waste applications

Chemometric analysis coupled with Raman spectroscopy and real-time or near-real-time display of the resulting data has been demonstrated in a few, limited examples. These include Hanford Tank Salt Cake Retrieval Project (2002-2005)(S. A. Bryan et al. 2006; S. A. Bryan, Levitskaia, and Schlahta 2008); Pretreatment Engineering Platform (PEP-WTP) Project (2008-2009);(Kurath 2009) and Near-Tank Treatment System, Pilot Scale CSL Testing (2011).(Edwards M.K. et al. 2011).

Within the Hanford Tank Salt Cake Retrieval Project, PNNL developed process monitoring instrumentation capable of measuring concentrations and total inventory of the components of solutions obtained from saltcake retrieval activities in Hanford Tank S-109. The process monitoring system, which was composed of a Raman spectrometer, conductivity probe, and Coriolis flow meter was assembled in a field-deployable test-skid configuration. Acceptance tests were performed before the test-skid was deployed for use in S-109 retrieval activities, which verified the acceptability of chemical composition analysis and software functionality. Figure 2 is a photo of the S-109 on-line monitoring system during acceptance testing. The concentrations predicted by the chemometric model were highly reproducible with the accuracy and precision of each analyte determined. Close agreement between the actual concentrations and average predicted values was found for all analytes with relative errors for most analytes being within the acceptance criterion of ± 20 %. The absolute error for all analytes was less than the ± 0.5 wt % acceptance criterion. Figure 2B shows the real-time computer display during S-109 retrieval testing.

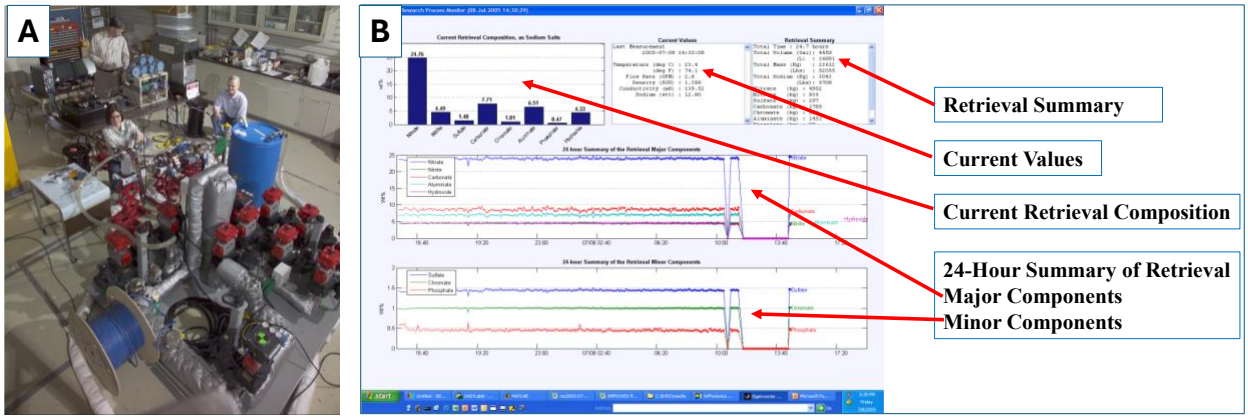


Figure 2. A) Photo of the S-109 on-line monitoring system during acceptance testing. B) Computer display showing real-time composition during S-109 retrieval testing.

Within the Pretreatment Engineering Platform (PEP-WTP) Project, the Raman method was employed as an alternative method that was implemented for the PEP tests to improve the turnaround time for analysis and reduce project costs. Due to the availability of the dedicated instrument and near-real-time analysis method, the Raman method provided results in less than 1 day from receipt of sample, compared with greater than 3-day turn-around from the standard methods such as ion chromatography (IC) and inductively coupled plasma (ICP) methods using offsite analysis. Work was completed under a full QA/QC HASQARD compliant procedure.(S.A. Bryan 2008) Quality control (QC) samples were generated at the analytical workstation and included a sample replicate determination, preparation blank, blank spike, and a matrix spike.

Within the Near-Tank Treatment System, Pilot Scale Continuous Sludge Leaching (CSL) Testing Platform, developed in 2011, an in-situ Raman probe was instrumented into the platform to provide real-time monitoring during continuous sludge leaching over a 24/7 2.5-month production run. The dissolution of boehmite and gibbsite aluminum mineral phases were monitored by following the aluminate and hydroxide concentrations in solution using the Raman in-line monitoring system developed for this program.(Edwards M.K. et al. 2011)

Past deployments of OLM have laid the foundation necessary for work completed under ARPA-E to expand sensing modalities and further reduce uncertainties of quantification through rigorous calculations.

1.1.3 Taking Sensors into a High-Radiation Environment: notes on previous studies on radiation effects

While not a focus of current ARPA-E efforts, it is recognized that downstream applications will be in high-radiation environments. Optical sensor materials and operation can be optimized for these applications, as demonstrated by previous efforts. Exposure to radiation dose will limit the lifetime of any material, where some systems exhibit higher tolerance and robustness than others. The Raman approach is a high tolerance example because only robust materials (Raman probe and fibers composed of glass and metal materials) are exposed to the dose while the sensitive

equipment and operators can be located 100's of meters away, connected to the probes by fiber optic cables.

Studies of Raman probe lifetime as a function of radiation dose received have been performed at PNNL. Initial experiments involved exposing probe and optical window material to gamma doses up to 1.7×10^8 rad. Typical lifetime doses anticipated in Hanford tank processing equipment are estimated to be less than 1×10^8 rad.(S. A. Bryan, Levitskaia, and Sinkov 2004; Lines et al. 2019) Materials were dosed in incremental steps to observe how spectral response was affected after different dosing timeframes. The probe and window materials did not fail within the cumulative maximum dose studied, and funding limited options to irradiate materials until failure.

Several quartz cuvettes constructed with the same material as the probe face widows were irradiated with PNNL's gamma facility to receive total acquired dose simulating the lifetime dose accumulation. Figure 3A shows the optical windows of the cuvettes which show some darkening as a function of dose. Between dosing steps, the irradiated probe and window material were used to measure an AP-105 simulant.(Lines et al. 2019) The NO_3^- model was applied to this data, and despite spectral variation, the concentration of NO_3^- was accurately measured, as presented in Figure 3B. This indicates data preprocessing accurately accounts for spectral intensity and baseline fluctuations.

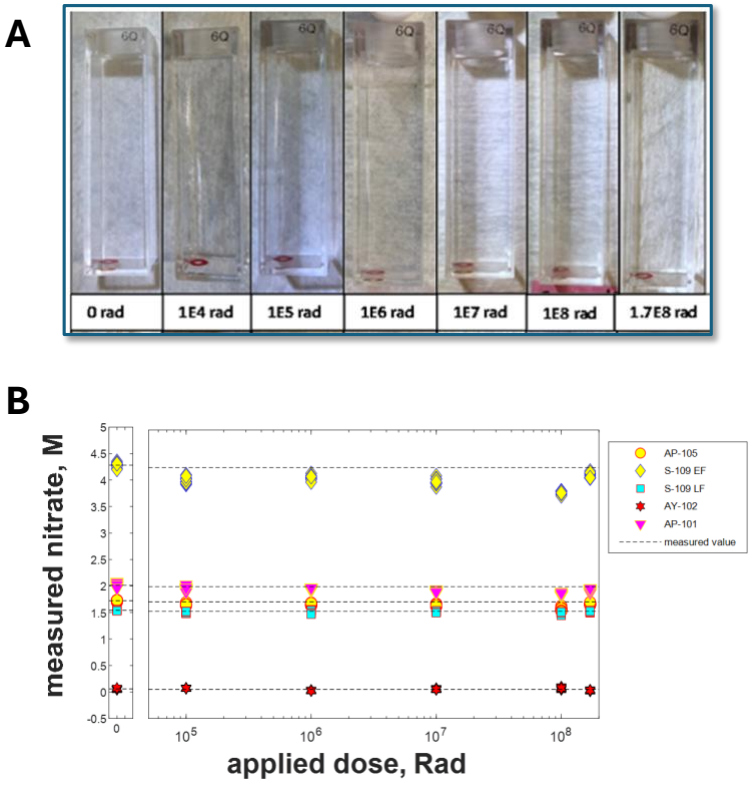


Figure 3. A) Quartz cuvettes irradiated within PNNL's gamma facility showing the relative darkening of the optical components as a function of dose. The total accumulated dose showing a range of dose from 0 rad (far left) to 1.7×10^8 rad (far right). B) Measured nitrate concentration as a function of applied dose to probe optics, for various simulated wastes.

1.1.4 Previous advancements of probe design for turbid solutions

Recent advances in data analysis have enabled application of optical spectroscopy-based monitoring approaches under conditions that have been traditionally prohibitive. This includes applications where matrix effects,(Clifford et al. 2021; H. E. Lackey et al. 2020; Lines et al. 2017; Lines, Hall, Sinkov, et al. 2020) band overlap,(Lines et al. 2018; Nelson, Asmussen, et al. 2018; Schroll et al. 2016) or baseline variation interferences(Nelson et al. 2021; Nelson et al. 2019a) are present. This expansion of applications is largely due to the utilization of multivariate analysis approaches such as chemometric analysis. However, advances in optical probe materials have also allowed for deployments in radioactive environments,(Lines et al. 2019) highly corrosive processes,(Schroll et al. 2016; H. M. Felmy et al. 2021) or high temperature systems such as molten salts.(Schroll et al. 2013; Schroll et al. 2016) Furthermore, incorporation of sensor fusion into probe design has also expanded the applicability of optical spectroscopy.(S. A. Bryan et al. 2011; Lines, Hall, et al. 2020a; Nee et al. 2018) We have also demonstrated how chemometric analysis and sensor fusion can be combined to expand optical-based monitoring approaches into process conditions that traditionally limit monitoring success, including variable turbidity streams.(Lines et al. 2022a; Heather M. Felmy et al. 2026) Specifically, the development and demonstration of a combined Raman-turbidity measurement probe has been developed.(Lines et al. 2022b) The combined Raman-turbidity probe allows for a unique opportunity to relate changes in Raman response to changes in turbidity of the sample or process stream through simultaneous data collection. Chemometric models that incorporate both data streams (Raman and turbidity measurements) are then uniquely capable of accounting for solution scattering effects and quantifying target chemical species. Two points of advancement and novelty were covered by this work: 1) the compact probe design allows for flexible *in situ* monitoring directly on a process stream or batch and 2) the analytical approach can avoid assumptions of stable chemistry that may hinder accurate applications to dynamic process streams. More recent work demonstrated how commercially available Raman probe designs could be integrated with advanced data science analysis to enable accurate quantification within a dynamic turbid environment without *a priori* knowledge of turbidity or solids mass fraction.(Heather M. Felmy et al. 2026)

1.1.5 Demonstration of enabling real-time, manual process control in nuclear fuel reprocessing

While efforts under ARPA-E were focused on pilot scale demonstration against relatively simple simulants, it is important to note optical sensors and mass balance approaches have been demonstrated on far more complex and radioactive simulant streams at the bench scale. In these demonstrations, online monitoring enables real-time, manual process control to hit ±1% target U/Pu ratio within product streams.

The optical techniques of visible absorbance, near infrared absorbance, and Raman spectroscopy were combined to quantify plutonium (III, IV, VI), uranium (IV, VI), neptunium (IV, V, VI), and nitric acid within various CoDCon and PUREX demonstrations on bench scale centrifugal contactors. Quantifying all these species is essential to process control, however no single form of optical spectroscopy can capture all the needed signals. Therefore, sensor fusion was essential to the success of CoDCon process control. The on-line monitoring tools simultaneously utilized ultraviolet-visible (UV-vis) absorbance, near infrared (NIR) absorbance, and Raman spectroscopy to characterize multiple target analytes within a continuous process separation scheme.

Chemometric modeling was used to quantify analytes in process streams in real-time and results were successfully used to enable immediate process control and generation of a product stream at a set composition ratio.(Lines et al. 2017; Lines et al. 2018; S. A. Bryan et al. 2011; Lines, Hall, et al. 2020a; Nee et al. 2018) During the CoDCon process, a comingled product stream containing uranium and plutonium was produced. The goal of the CoDCon process was to achieve the U/Pu product in a 70%/30% ratio, and since this is a dynamic process the U/Pu product ratio could be changed and fine-tuned by the operator during the experiment. Based on on-line monitoring results, operators adjusted (time of adjustment indicated by vertical dashed lines in Figure 4) the flow rate of the fresh TBP process stream to alter the composition ratio of the product stream. As can be seen in this figure, the 70/30 ratio of U/Pu was established early in the process (~100 min) and maintained within 1% for the remainder of the experimental run, confirmed by online measurements (solid lines) and, much later, offline measurements (markers).

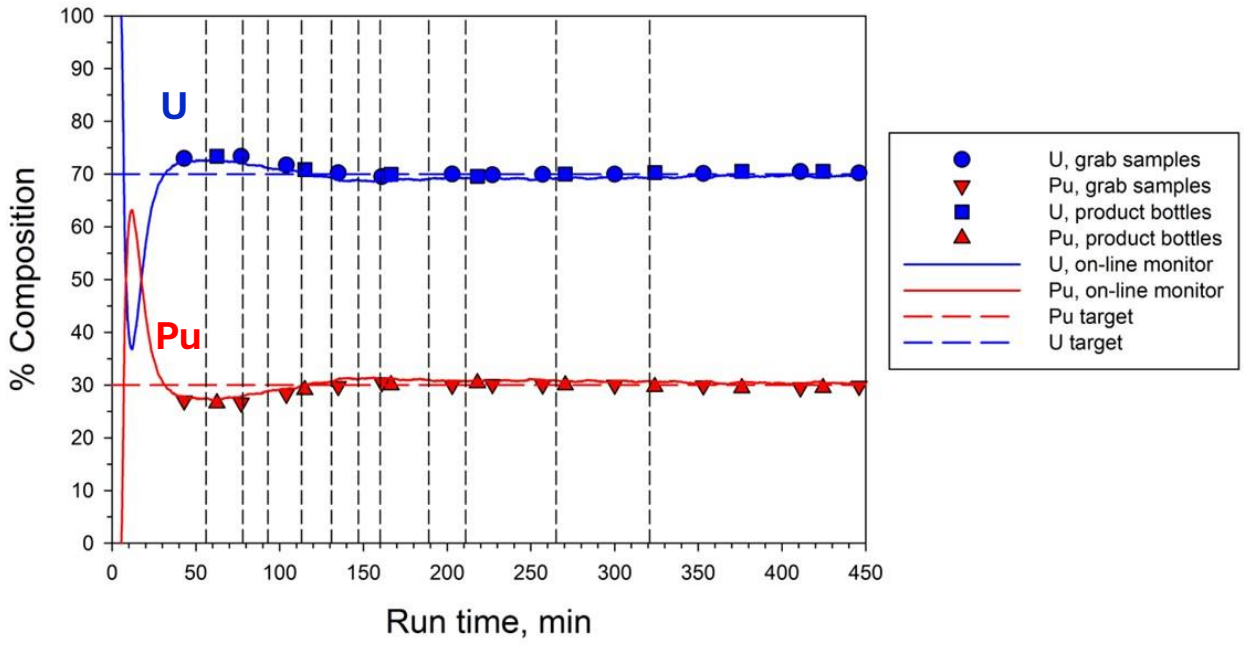


Figure 4. The percent composition of U and Pu in the aqueous product stream during CoDCon run.

2.0 Hardware and Equipment

A key aspect of project work was designing a sensor system that could provide a more robust and flexible approach to industrial scale online monitoring. Industrial scale monitoring of spent nuclear fuel processing poses many challenges, including but not limited to radiation and chemistry impacts to sensors and difficulty to access sensors for maintenance or calibration. Mitigating for these various impacts can be accomplished through combined optimization of sensor hardware as well as data processing. Covered in this section is the hardware design and optimization of instrumentation and sensors to enable more reliable and robust deployment of optical online monitoring sensors. This will include an overview of instrument specifications, which were optimized to enable remote and simultaneous monitoring of multiple process locations. Discussion also includes the design and testing of both in-pipe and in-vessel probes. Examples of collected data will be provided, and subsequent sections will cover the development and validation of automated data analysis algorithms.

2.1 Spectrometers

A Spectra Solutions Raman instrument was purchased for this work and included a multitrack system. This system consisted of 200 mW 671 nm (red) lasers and a back illuminated charge-coupled device (CCD) detector that covered the range of ~140 cm^{-1} to ~5600 cm^{-1}. This instrument's multitrack design consisted of 6 individual excitation and collection ports. This allows for 6 different measurement locations with each track having its own excitation laser, making the system robust to potential degradation or breakage of one laser. This laser light was transmitted via 105 µm FC/PC fiber optic fibers to a Raman probe. This Raman probe then collected the response via a backscattering geometry (180º) with a laser light filter, allowing light to pass through a 200 µm FC/PC fiber back into the collection port where the light was separated via a diffraction grating onto the CCD detector. The fiber optics utilized can be manufactured for long lengths (100s of meters) allowing an increased distance for personnel and instrumentation from eventual radiological deployment, which aligns with as low as reasonably achievable (ALARA) principles.

Additionally, a Spectra Solutions UV-vis instrument was purchased in a multitrack system configuration with a functional wavelength range of ~400 – 1000 nm. This instrument consists of an excitation port which couples to a chosen excitation source. The light from the excitation port is then split evenly between all the tracks, resulting in the ability to measure UV-vis in multiple locations. In this work, a ThorLabs xenon arc lamp SKS205 was used due to its 75 W bulb resulting in 3.5 mW fiber coupled output and broad wavelength range of 240 to 1200 nm. The ThorLabs lamp was connected to the Spectra Solutions instrument via a 100 µm SMA to FC fiber, paired with a 105 µm FC/PC fiber. After the light was dispersed across the 6 tracks, it was transmitted via 105 µm FC/PC fibers to the excitation locations. The collection locations were in linear geometry (180°) with 200 µm FC/PC fibers and transmitted back the spectrometer where it was dispersed across the CCD using the diffraction grating.

2.2 Probes and Sensor Systems

The Power Fluidics and Optical Online Spectroscopy (PFOOS) test rig is designed to pump solution from the supply tank (Tank 1) to the receipt tank (Tank 2) using power fluidic (PF) devices

housed within the supply tank. The solution is pumped through a straight section of pipe with valves used to direct the solution through three parallel flow cells, or to bypass them altogether. The valves can be configured to flow through any combination of the flow cells. Additionally, a set of in-tank deployed probes are located in Tank 1. Figure 5 shows a schematic of the power fluidic system with integrated Raman and UV-vis sensors.

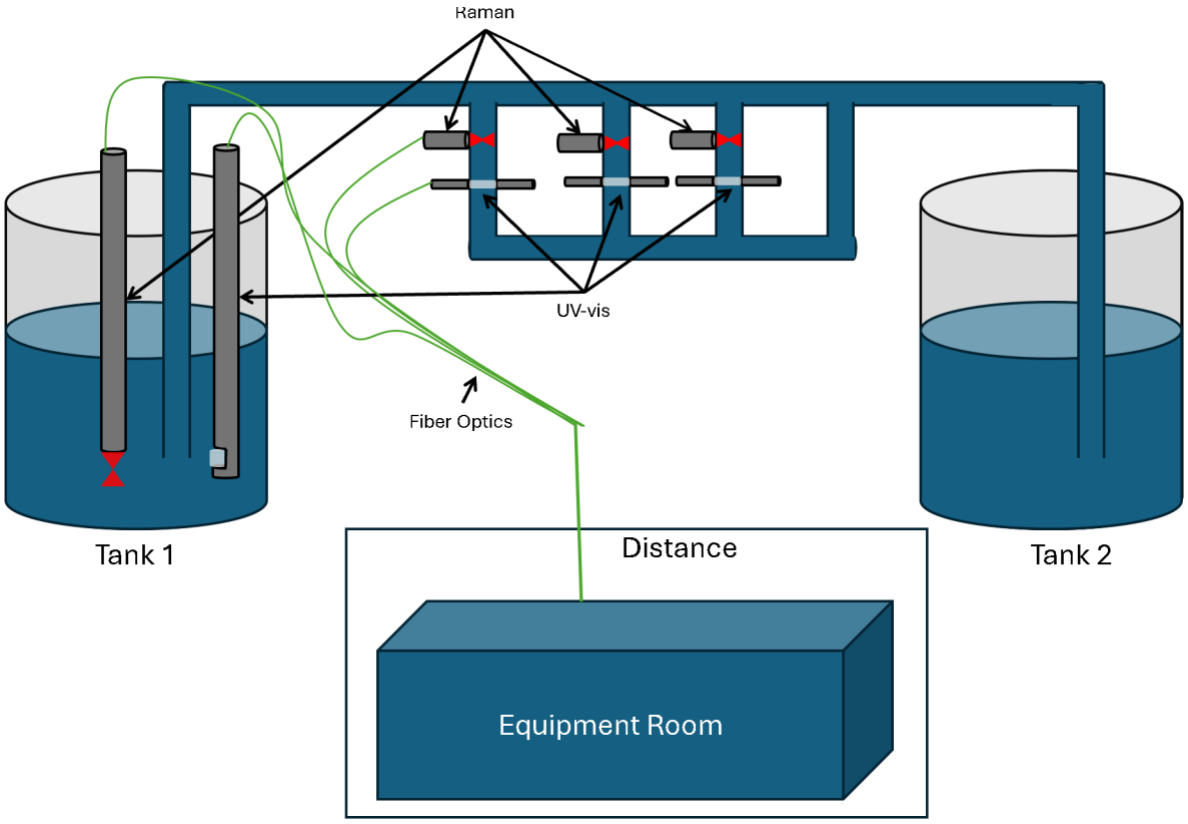


Figure 5. Schematic diagram of the power fluidic system and integrated Raman and UV-vis sensors.

2.2.1 The parallel cell: innovating mitigation strategies for realistic operations

A parallel flow cell manifold was designed with three valved parallel flow cells and a bypass line to enable the collection of data from multiple optical sensors simultaneously or individually depending on maintenance, response check, or referencing needs. Figure 6, shows the relative orientation of the UV-vis and Raman optics on each flow cell, as well as their vertical orientation, chosen to minimize the effect of entrained bubbles. Sight glasses, shut-off valves, and flanged connections enabled the removal/replacement of individual flow cells as needed for maintenance/calibration activities. The sight glasses allowed for visualization of the process fluid during operation.

Chemometric model training set spectra were collected on one parallel cell, and a calibration transfer was done to the other cells. The results of this are detailed in later sections. Ultimately, each parallel cell resulted in slightly different variations in response due to machining constrictions resulting in imperfections in optical pathlength. Despite these imperfections, light transmission

was more than adequate for accurate data collection and chemometric modeling. The implementation of multiple parallel cells compared to a single cell demonstrates the ability to measure various points in an industrial stream. Additionally, this deployment allowed for individual cells to be closed and disconnected if desired.



Figure 6. Photo of deployed parallel cells at NuVision Engineering.

2.2.2 Immersion probes

The parallel inline flow cells were paired with a set of optical immersion probes that were deployed in the supply tank. The tank-deployed probes were designed to be immersed in the tanks where they would provide additional data to compare to the inline probes. This enabled monitoring of the surrogate in the supply tank even when transfers were not taking place, and it provided insight into interval timing between transfers to avoid entraining air into the flow from mixing operations. The immersion probes consisted of one UV-vis and one Raman probe with similar geometry and optical properties as the inline flow cells. This allowed for the model trained on the inline flow cell to be adapted via calibration transfer to the immersion probes. Advances were made in the sealing and integration approaches for probes meant for large vessels (i.e. probes meant to immerse >1 m into solution).

Advancement of this design was completed iteratively. The probes were constructed from stainless steel and were first mounted at the bottom of schedule 80 PVC risers. For implementation into NuVision Engineering's power fluidics system, the probes were connected to a PVC schedule 80 pipe and fastened with a compression fitting. However, due to the duration of experimental collection and pressure in the tank, the seal failed, resulting in water seeping into the optical probes, significantly reducing optical signal. Ultimately, a combination of welding and a marine adhesive

on a <2 mm spacing with PVC tubing was utilized for the visible immersion probe, while the immersion Raman probe was sealed using a bulkhead fitting. These seals were then tested at the PNNL testing rig for 1 day before being dismantled and transported to NuVision Engineering for deployment. It is recognized that welding and alternative sealing approaches will be required for different flow sheet types and process conditions. The base design developed and demonstrated here serves as a strong learning foundation for those future engineering optimizations.

3.0 Design of Experiments

The purpose of this project was to provide a focused demonstration of the ability of OOS combined with PF to achieve material accountancy at a ±1% uncertainty. This was accomplished through careful selection of surrogate material, development of an automated data analysis system (chemometric analysis partnered with custom mass balance algorithms), and a full-scale demonstration on the PFOOS test rig. Selection of the surrogate material (neodymium (III) nitrate) and development of the initial test plan were completed in 5308-PROJ-037, *Test Plan Concept*, and PNNL-SA-211652, *Memorandum of Simulant Formulation*. The automated data analysis is described in later sections.

3.1 Success criteria

The experimental campaign consisted of transferring a surrogate solution through the PFOOS test rig and across the parallel flow cells described in Section 2.0. Live data from the parallel flow cells and the in-tank probes were processed by chemometric models to determine the concentrations of neodymium (III) and nitrate ions in solution. These concentrations were then used in the mass balance calculations by combining with either flow meter or mass scale (scales located under tanks) data. Subsequent uncertainty analysis was based on propagating combined uncertainties from optical and flow/mass sensors. Neodymium (III) and nitrate served as non-radioactive surrogates for the actinide targets, and $NaNO_3$ served as the lower-hazard surrogate for nitric acid.

Uncertainty analysis requires combining the OOS data with data from other system sensors including tank scales, flow meters, density meters, and level sensors. To further quantify system uncertainty, two surrogate dilutions and a blank solution experiment were added to the campaign. A successful campaign therefore required the simultaneous collection of OOS data and PFOOS test rig data across three concentrations of surrogate material and a blank. Consistent with the project objective, success was evaluated against a target of ±1% uncertainty in the resulting material accountancy, with a supporting goal of repeatable measurement to within less than 1% deviation from the mean.

3.2 Surrogate test material

For the purposes of this work, a balance was needed between minimizing surrogate chemical hazards and including well-benchmarked species to demonstrate representative performance on mass balance calculations. Nd(III) has been studied previously due to the strong UV-vis signal. Real-time analysis methods have been developed for this target across scales from the micro scale with microfluidic devices (Hope E. Lackey et al. 2024; Nelson et al. 2021; Nelson et al. 2019b) to lab scale in solvent extraction systems (Tse et al. 2025), and in complex chemical systems with analytes with interfering optical signals (Tse et al. 2022). Furthermore, Nd is a commonly used simulant for the optical properties of species such as Pu. Nitrate is already a common target in fuel reprocessing flowsheets and has a well-understood Raman fingerprint. Previous work has demonstrated the ability to quantify nitrate from different sources (e.g., $An(NO_3)_3$, $Ln(NO_3)_3$, $NaNO_3$, and HNO_3) and under different process conditions and scales (Heather M. Felmy et al. 2023; Heather M. Felmy et al. 2022; Nelson, Lines, et al. 2018; Lines et al. 2018). This prior knowledge lays the foundation to scale these systems up to larger process scales in this work.

PNNL-SA-211652, *Memorandum of Simulant Formulation*, recommended a pH 5.0 neodymium (III) nitrate formulation prepared to limit solubility concerns while the surrogate material was in transit. The recommendations are summarized in Table 1.

Table 1. Summary of PNNL-SA-211652 Memorandum of Simulant formulation.

Target	Operating range	Possible sources	Notes on purity
Sodium nitrate	0-3 M	Sigma-Aldrich or other common commercial vendors	Recommend 99% or higher
Neodymium nitrate $Nd(NO_3)_3$	0-10 mM (0-0.01 M)	Sigma-Aldrich or other common commercial vendors	Recommend 99% or higher
pH	5.0 ± 0.2		

The surrogate was ordered from NOAH Chemicals and measured as 3.025 M sodium nitrate and 12.1 mM neodymium nitrate. The higher-than-expected concentrations were deemed to be within the bounds of the training set data collection, and therefore within the bounds of the established models.

Further testing and confirmation of simulant concentrations, chemical stability, and purity were completed utilizing a variety of techniques and measurements completed over the course of demonstrations.

3.3 Test configuration

Document 5308-PROJ-037, *Test Plan Concept*, was modified to increase the number of replicates available for uncertainty analysis within the available funding. This was accomplished by performing a matrix of full and partial tank transfers, with solution directed through two of the three parallel flow cells: cell 1 and either cell 3 or cell 4. Cell 2 was a back-up cell that was not used for these tests. The test matrix is summarized in Table 2. Blank solutions were also collected under these same conditions to evaluate instrument performance.

Table 2. Consolidated test matrix.

Experiment	Cells	Solution	Details
Trial 1	1,3	Surrogate	Full tank transfer at 2.3 Bar, 3 replicates
Trial 2	1,3	Surrogate	Full tank transfer at 1.0 Bar, 3 replicates
Trial 3	1,3	Surrogate	Full tank transfer at 2.3, 2.0, 1.0 Bar
Trial 4	1,3	Surrogate	First third tank transfer at 2.3, 2.0, 1.0 Bar
Trial 5	1,4	Surrogate	Second third tank transfer at 2.3, 2.0, 1.0 Bar
Trial 6	1,3	Surrogate	Recirculation on and off
Trial 7	1,3	First dilution	Full tank transfer at 2.3 Bar, 3 replicates
Trial 8	1,3	First dilution	Full tank transfer at 2.3, 2.0, 1.0 Bar
Trial 9	1,3	First dilution	First third tank transfer at 2.3 Bar, 3 replicates
Trial 10	1,4	First dilution	Second third tank transfer at 2.3 Bar, 3 replicates
Trial 11	1,3	Second dilution	Full tank transfer at 2.3 Bar, 3 replicates
Trial 12	1,3	Second dilution	Full tank transfer at 2.3, 2.0, 1.0 Bar
Trial 13	1,3	Second dilution	First third tank transfer at 2.3 Bar, 3 replicates
Trial 14	1,4	Second dilution	Second third tank transfer at 2.3 Bar, 3 replicates
Trial 15	1,3	Second dilution	First third tank transfer at 2.3, 2.0, 1.0 Bar
Trial 16	1,4	Second dilution	Second third tank transfer at 2.3, 2.0, 1.0 Bar

4.0 Automating Data Analysis and Chemometric Analysis

This section documents the process involved in developing the chemometric models used in the automated quantification of Nd^{3+} and NO_3^- concentrations based on optical signatures. This represents two of the data streams fed into mass balances and uncertainty calculations as discussed in later sections. Chemometric models were developed through a stepwise process. First, a training set was prepared consisting of a matrix of neodymium nitrate and sodium nitrate concentrations. The training set was then measured using parallel flow cell 1, and the resulting data was used to build chemometric models that regressed neodymium and nitrate. The models were then applied via calibration transfer to cells 2, 3, and 4, as well as the in-tank probes. These models were used during the experimental campaign on the PFOOS test rig (Table 2). The performance of the models during the campaign was tracked against data from a calibration solution on-site. The methods used to track and adjust for changes over the course of the campaign are discussed.

While these approaches have been well demonstrated in bench scale applications previously, efforts here saw advancement in transitioning applications to pilot scale and adapting applications to the flow profiles of the Power Fluidics system.

Note, the demonstration of extending models built on one cell to additional cells also lays the foundation for the development of widely deployable models and model maintenance toolkits. While further advancement is needed, this type of plug and play nature will be needed in deployment by industry.

4.1 Data acquisition and model parameters

The training/calibration set data was collected at 1 sec integration for Raman and 0.3 sec integration for UV-vis. 100 spectra were collected for each sample. These spectra were averaged by 25 leaving 4 replicate spectra of each sample. Spectral data was collected using SpectraSoft software. This data was then extracted and analyzed in MATLAB (R2022b) using the Eigenvector Research PLS-Toolbox (version 9.2). Raman spectral preprocessing involved a 1^{st} order polynomial baseline correction around the water band (~3000 – 4000 cm^{-1}) followed by a normalization to the area under the water band to account for laser power fluctuations. A first derivative (2^{nd} order polynomial with a 15-point filter width) was then applied to remove baseline effects and then a mean centering was applied to equally weigh the high and low concentration spectra. Only the spectral region from 500 – 2000 cm^{-1} was used for modelling nitrate concentration. The UV-vis spectra were preprocessed using a first derivative (2^{nd} order polynomial with a 15-point filter width) to remove baseline shifts. The region from 450 – 900 nm was used for modeling Nd^{3+} concentration, with the following non-analyte regions excluded: 620 – 680 nm where the 671 nm Raman laser caused interference and 830 – 840 nm which included a light source interference peak.

PLS regression models were built for NO_3^- using Raman spectra and Nd^{3+} using UV-vis spectra. Cross validation used a venetian blinds method (5 data splits, blind thickness of 4) allowing for the sequential removal of ~20% of the calibration spectra. The remaining spectra were then used to predict the removed spectra during cross validation. Model statistics included the root-mean-square error of calibration (RMSEC) which is a measure of uncertainty in the calibration dataset, the root-mean-square error of cross validation (RMSECV) which is a measure of the uncertainty

in predicting samples sequentially removed from the calibration dataset during cross validation, and the root-mean-square error of prediction (RMSEP) which is a measure of the uncertainty in predicting samples unknown to the model.

Online measurements were performed by loading the PLS models into the SpectraSoft software which uses Solo Predictor for real-time model output. Using this software, the analyte concentrations are displayed in real-time as spectra are collected, and model output is also saved to a file allowing for further analysis offline. With the spectral integration time and model processing time, the analyte concentrations can be measured on the timescale of a few seconds.

4.2 Small-scale chemometric modeling

The model calibration dataset consisted of a series of $NaNO_3$ and $Nd(NO_3)_3$ solutions prepared as single component and mixed analyte solutions of 0 – 3 M NO_3^- and 0 – 30 mM Nd^{3+}. A separate test sample set was prepared within the same concentration range but different sample concentrations as a test of model performance. These two datasets were collected on cell 1 on Track 1 of the Raman and UV-vis instruments to be used as the primary models. The calibration spectra are shown in Figure 7 where the primary NO_3^- Raman peak at 1047 cm^{-1} is highlighted in the inset and the Nd^{3+} UV-vis bands are shown with variable concentration.

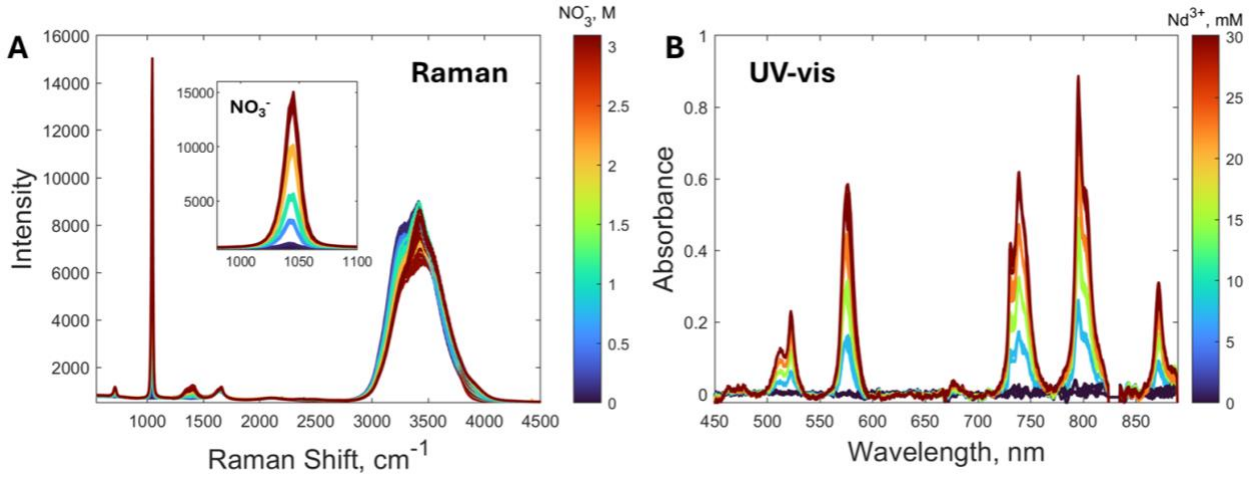


Figure 7. Calibration set spectra collected on cell 1 for A) Raman B) UV-vis. The primary NO_3^- Raman peak is shown in the inset.

These spectra were preprocessed and wavelength selected using the method described above and the resulting calibration and test set spectra are shown in Figure 8 A and B. PLS models were built on the calibration data and applied to the test sample spectra. The resulting parity plots showing known vs. model measured concentrations are shown in Figure 8 C and D. A one-to-one correlation between known and model measured concentration (red line) indicates a perfectly accurate model, and the line of best fit to the predicted data very closely aligns with the one-to-one correlation.

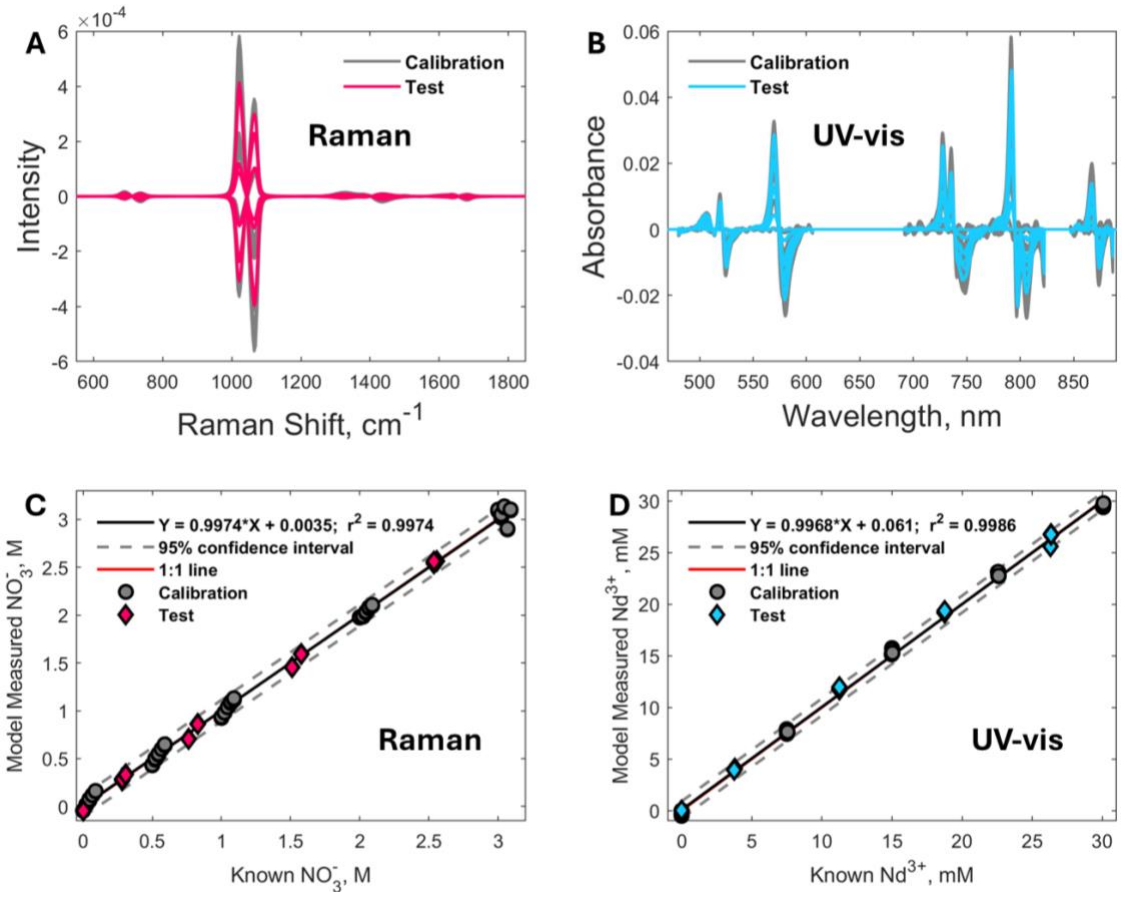


Figure 8. Preprocessed spectra collected on cell 1 for A) Raman and B) UV-vis for the calibration and test datasets along with the corresponding parity plots of known vs. PLS model measured concentration of C) NO_3^- from Raman and D) Nd^{3+} from UV-vis.

The model statistics are shown in Table 3 for the data collected on the calibration and test set measured on cell 1. The RMSEC, RMSECV, and RMSEP were all similar, indicating consistent model performance on new samples. The highest values of 0.069 M NO_3^- and 0.48 mM Nd^{3+} can be considered the uncertainties in the models. The limits of detection (LOD) were also calculated from the parity plots using methods described elsewhere.(Allegrini and Olivieri 2014; Parastar and Kirsanov 2020) The LODs were 0.18 M NO_3^- and 1.4 mM Nd^{3+}.

Table 3. Model statistics for Raman and UV-vis collected on cell 1 including the RMSE values, R^2 values, and LODs.

Technique	RMSEC	RMSECV	RMSEP	R^2, Cal	R^2, CV	R^2, Pred	LOD
Raman	0.0548 M	0.0688 M	0.03425 M	0.9974	0.9959	0.9987	0.184 M
UV-vis	0.405 mM	0.447 mM	0.4778 mM	0.9986	0.9982	0.9982	1.36 mM

The data collected as the calibration set on cell 1 was then compared to the performance on the other three parallel flow cells as well as the immersion probes. A smaller subset of the calibration set was collected on each of the other sensors. This was used as a validation set in the models to

compare differences in sensor signals. The results with no corrections applied are shown in Figure 9 A and B. There is some deviation in both the Raman and UV-vis model responses. This indicates differences in signal between the different flow cells and probes. Differences are expected as optics and detector track variation will lead to differences in the signal produced for each flow cell and the immersion probes. The smaller subset data was used for calibration transfer via a slope and intercept correction to build models designed to accurately quantify signal for each flow cell and probe. The model performance after the slope and intercept correction are shown in Figure 9 C and D. These results show better agreement with the calibration set models for all flow cells and for the immersion probes.

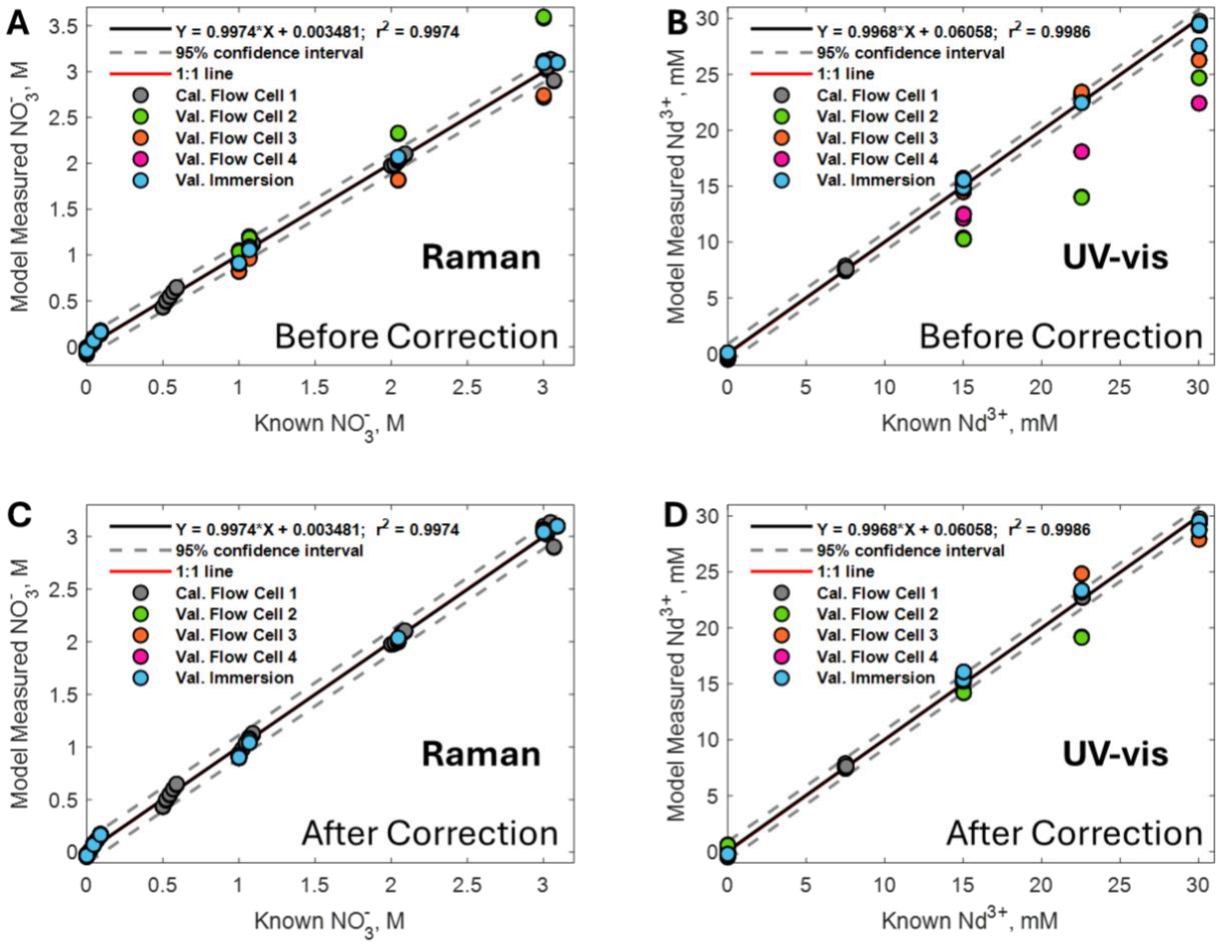


Figure 9. Parity plots showing the model results comparing the calibration dataset collected on cell 1 to validation data collected on cells 2-4 and the immersion probes for A) NO_3^- from Raman and B) Nd^{3+} from UV-vis before applying a slope and intercept correction to the models, and the model results for C) NO_3^- from Raman and D) Nd^{3+} from UV-vis after applying a slope and intercept correction to the models for cells 2-4 and the immersion probe.

A validation flow experiment was then performed using the parallel flow cells 1, 3, and 4. In this experiment, water was flowed through the parallel cells and then sequential additions of $NaNO_3$ and $Nd(NO_3)_3$ were made to the solution tank and allowed to dissolve. Preliminary NO_3^- Raman

and Nd^{3+} UV-vis models were running in real time. These models were further optimized based on the results of this flow experiment. Figure 10 shows the Raman spectra and model output during this continuous measurement and Figure 11 shows the results for the UV-vis.

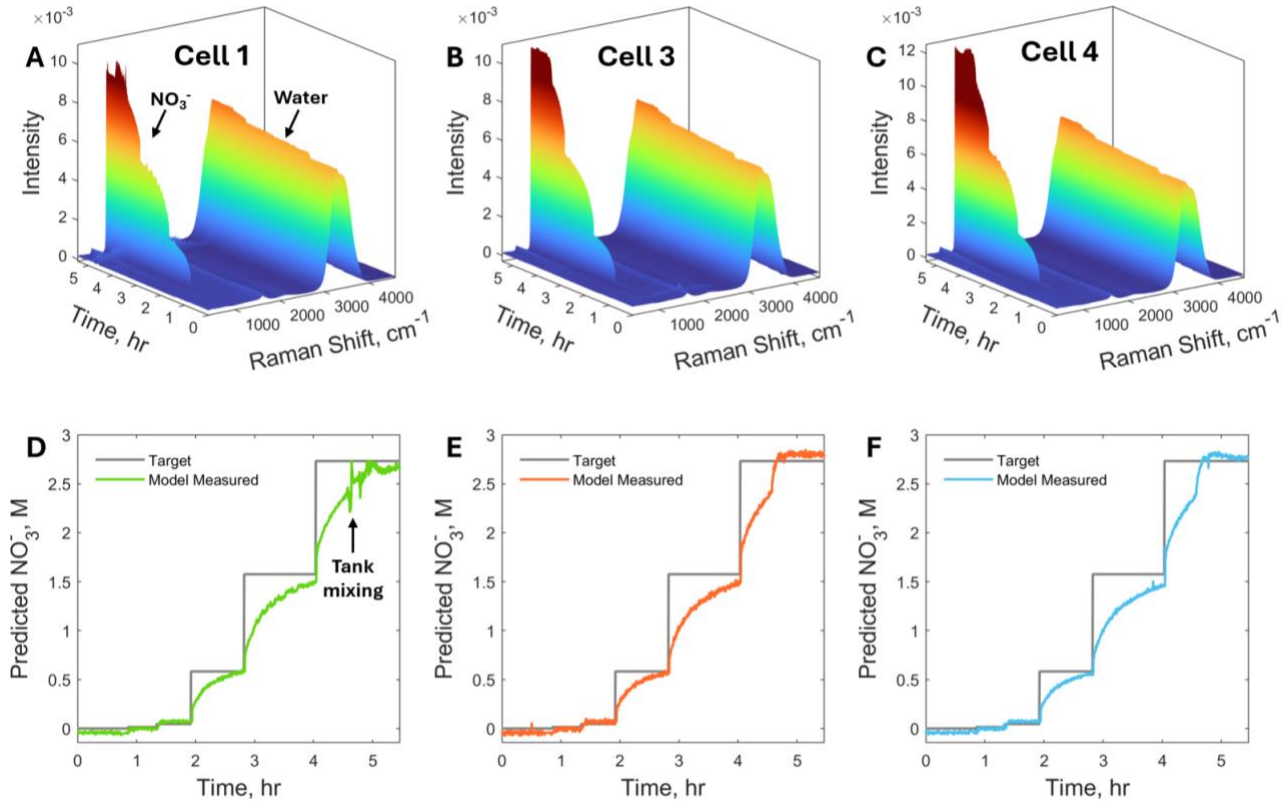


Figure 10. Flowing solution test showing the normalized and baseline corrected Raman spectra for A) cell 1, B) cell 3, and C) cell 4 along with the corresponding target vs. model measured nitrate concentrations for D) cell 1, E) cell 3, and F) cell 4.

The Raman spectra shown in Figure 10 A – C were baseline corrected and normalized to the area under the water band around 3000 cm^{-1} to visualize the changes in the spectrum with added NO_3^-. The primary nitrate band around 1050 cm^{-1} increases as $NaNO_3$ was added to the tank. This is also reflected in the target vs. model measured concentrations in Figure 11 D – F. It is important to note that the model measured concentrations slowly increase after each addition of nitrate because the solid dissolved slowly, only reaching that addition's target concentration after a long period of dissolution and mixing. During the experiment, the model output was monitored, and the solution was allowed to equilibrate until the model output appeared to stabilize.

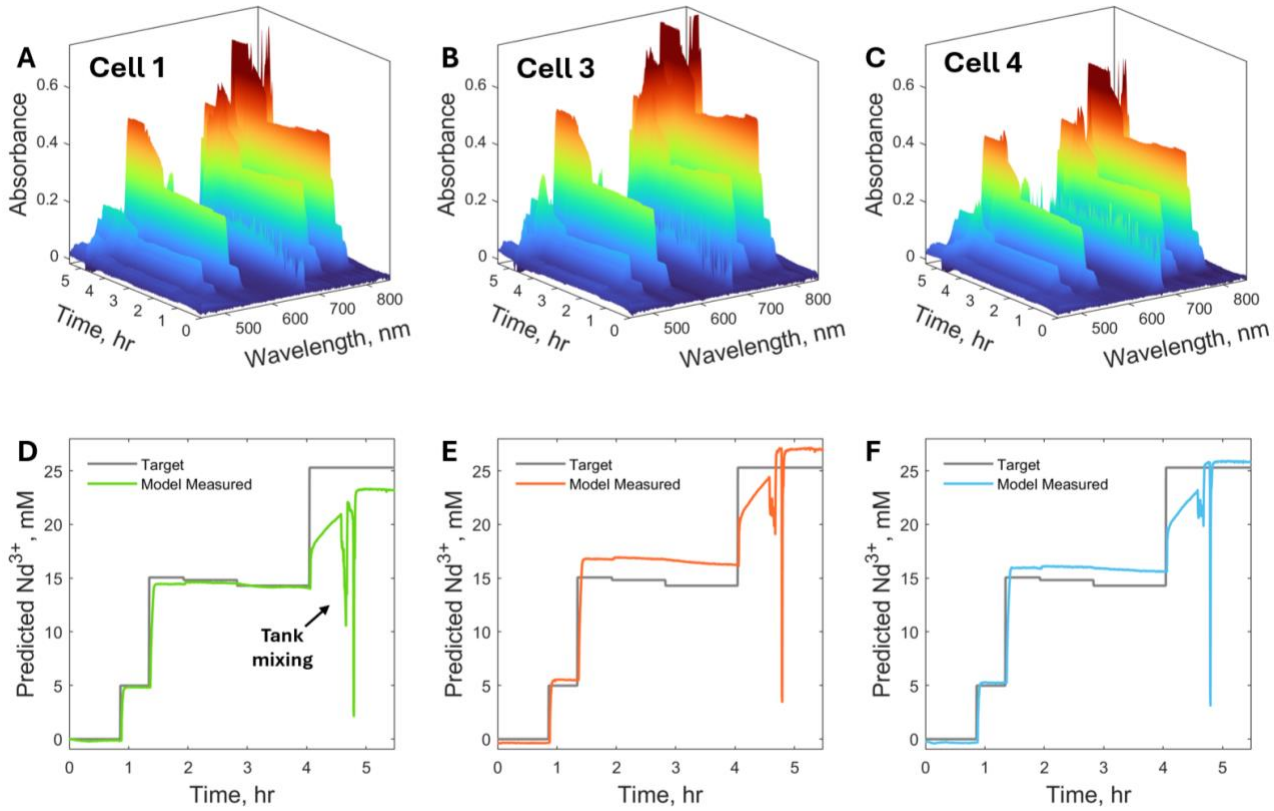


Figure 11. Flowing solution test showing the baseline corrected UV-vis spectra for A) cell 1, B) cell 3, and C) cell 4 along with the corresponding target vs. model measured neodymium concentrations for D) cell 1, E) cell 3, and F) cell 4.

The UV-vis Nd^{3+} model was also running in real time, and it was observed that the Nd^{3+} concentration equilibrated more quickly than the $NaNO_3$ concentration, indicating that the solid $Nd(NO_3)_3$ dissolved much more quickly. There was more variation in the target vs. model measured Nd^{3+} concentration than the NO_3^- concentration, but the signals produced from Raman vs. UV-vis are not directly comparable and the concentration ranges were very different (M for NO_3^- and mM for Nd^{3+}). The concentration trends, however, were in agreement with the model output.

Additional causes of the model response deviating from the targeted concentrations in the flow validation data include the method of solution preparation being less precise than the calibration set samples, which introduced increased uncertainty in the "known" values to which model output is being compared. Instrument response can also fluctuate over time, and additional calibrations can improve uncertainty. It was therefore decided that onsite demonstrations of the Raman and UV-vis models would involve measuring a calibration check solution. Models can be updated based on the response of this check solution to provide more accurate real-time results.

4.3 Deployment of sensors

Several solutions were utilized during the onsite deployment of the sensors. These included a blank solution, a calibration solution, and a surrogate solution. The blank solution was used as a reference

for the UV-vis measurements. The calibration solution was intended as a test of the model response and was measured periodically throughout the deployment. The calibration solution was prepared at PNNL and the blank and surrogate solutions were prepared by NOAH chemicals. The concentration of Nd^{3+} and NO_3^- in the calibration and surrogate solutions were determined by standard addition. Here, solutions were prepared by adding a known volume of calibration or surrogate solution to volumetric flasks, each containing increasing concentrations of $Nd(NO_3)_3$ and $NaNO_3$ solutions of known concentration. With this method, the initial Nd^{3+} and NO_3^- concentrations in the calibration and surrogate solutions could be determined. The UV-vis and Raman spectra of these solutions were plotted with a first derivative applied to remove baseline shifts. Figure 12 shows the results of the UV-vis standard addition measurement. The absorbance at 572 nm was plotted against the added Nd^{3+} concentration. The 795 nm peak was chosen for the standard addition calculation because it has the highest signal to noise ratio of the observed peaks. This peak is also not as sensitive to changing nitrate concentration as the peak at 572 nm, which increases more significantly with increasing nitrate concentration.(Nelson et al. 2019b) The analyte concentrations were calculating from where the standard addition curve crosses the y-axis. The initial undiluted solution concentrations were then calculated from these results and are included in Table 4.

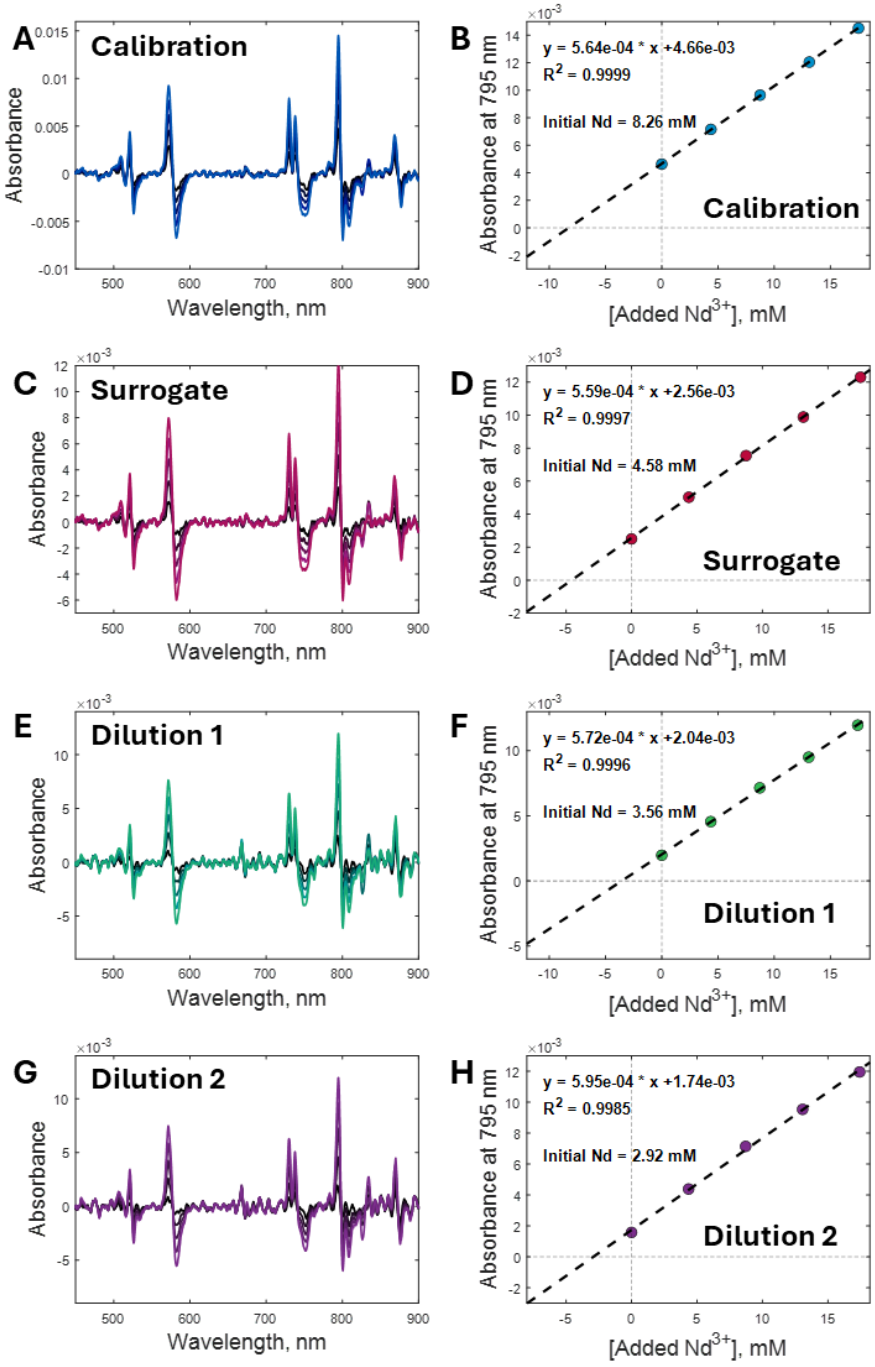


Figure 12. UV-vis spectra of the standard addition solutions with a first derivative applied for the A) calibration, C) surrogate, E) first dilution, and G) second dilution solutions. The univariate calibration curves of absorbance at 795 nm vs. added Nd^{3+} concentration used for the determination of the initial Nd^{3+} concentration for B) calibration, D) surrogate, F) first dilution, and H) second dilution solutions.

Figure 13 shows the Raman standard addition results. Here, the nitrate peak at 1022 cm^{-1} was used for the calculation of the initial NO_3^- concentration in each solution. The resulting NO_3^- concentration of each solution is included in Table 4.

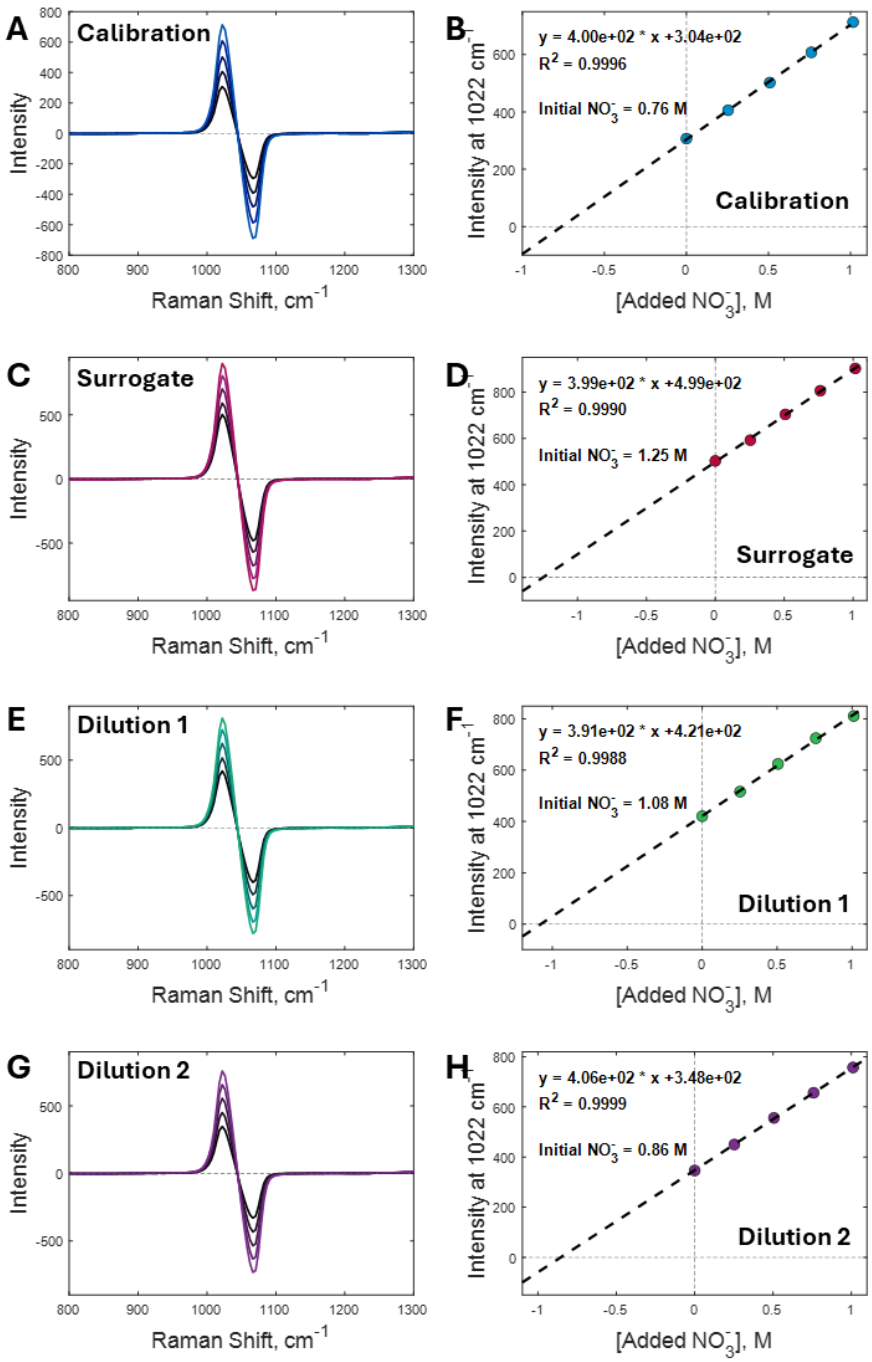


Figure 13. Raman spectra of the standard addition solutions with a first derivative applied for the A) calibration, C) surrogate, E) first dilution, and G) second dilution solutions. The univariate calibration curves of absorbance at 1022 cm^{-1} vs. added NO_3^- concentration used for the determination of the initial NO_3^- concentration for B) calibration, D) surrogate, F) first dilution, and H) second dilution solutions.

Table 4. Solution concentrations determined by standard addition.

Solution	Nd^{3+}, mM	NO_3^-, M
Calibration	20.7	1.90
Surrogate	11.5	3.13
Dilution 1	8.97	2.71
Dilution 2	7.36	2.15

During the deployment of the UV-vis and Raman sensors, 3 parallel flow cells and 1 immersion probe were utilized for each technique. Because this was a dynamic system with heterogenous flow, at times the sensors encountered drained lines or bubble formation. An example of the impact of this to one of the inline Raman sensors is shown in Figure 14. In this instance, the flow cell was filled with the blank solution, then the calibration solution, then the blank solution again. The line was periodically empty due to pulsing of the pump. When measuring these solutions, the water peak around 3500 cm^{-1} should be relatively constant, but due to the periodic draining of the flow cell, the peak disappears when the cell is empty. The empty flow cell data will cause anomalous chemometric model results due to a lack of analyte information for the model to use. The Raman model results were especially impacted by the emptying of the cell due to the normalization step in the preprocessing.

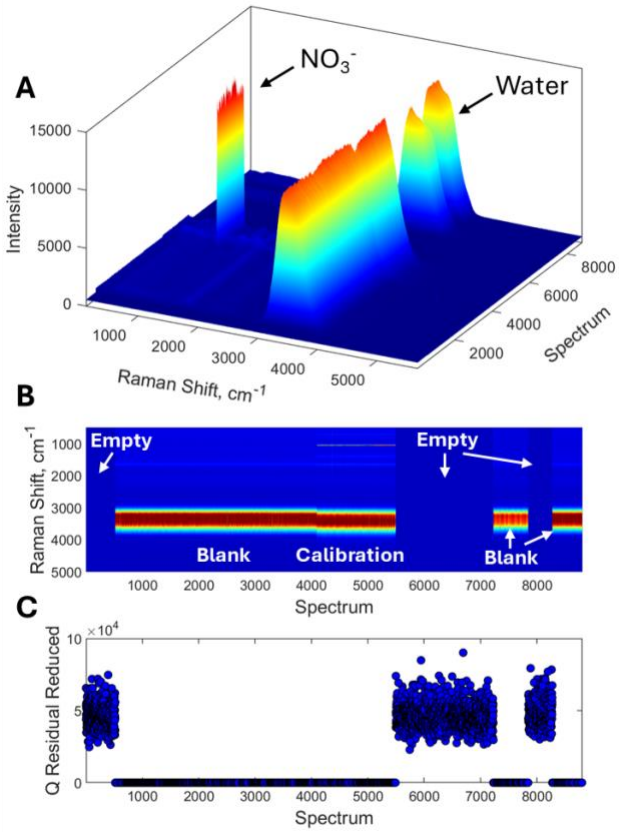


Figure 14. A) Raman spectra collected on cell 1 measuring the blank solution and calibration solution. B) Top-down view of the Raman spectra. C) Reduced Q residuals of the model.

The model statistics include Q residuals. Q residuals indicate how similar the data is to the training set. A high Q residual indicates data that is not consistent with the training set spectra. In this case, the empty flow cell yielded high residuals, and these residuals can be used to mark data as irrelevant to the measurement. Figure 14C shows high Q residuals for the data when the cell was empty. This data was removed from the dataset and the resulting spectra and model results are shown in Figure 15. This figure shows the model accurately predicting 0 M nitrate in the blank solution and 1.9 M nitrate in the calibration solution. A Q residual cutoff was applied to all other Raman spectra shown in this section.

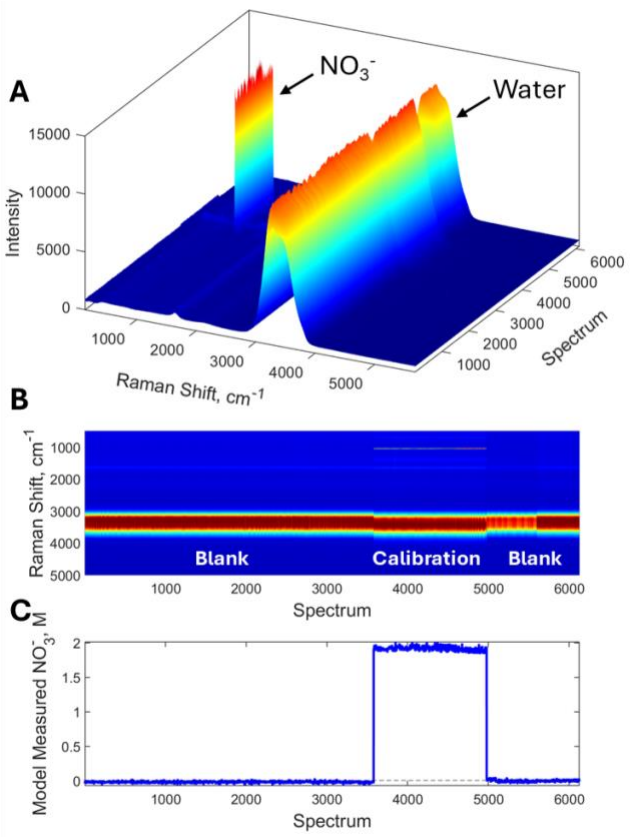


Figure 15. A) Raman spectra collected on cell 1 measuring the blank solution and calibration solution after the removal of spectra with reduced Q residuals >50. B) Top-down view of the Raman spectra. C) Model results showing the measured nitrate concentration.

The calibration solution was measured at the start and end of each week of measurements to verify model performance and provide data for ongoing calibration maintenance. The blank and calibration data measured at the start of the first and second week of tank transfers was used to update the models using a slope and intercept correction. Figure 16 shows the UV-vis Nd^{3+} model measured concentrations for the blank (0 mM Nd^{3+}) and the calibration solution (20.7 mM Nd^{3+}) before and after the application of the slope and intercept correction. The results show better agreement with the known concentrations after the correction.

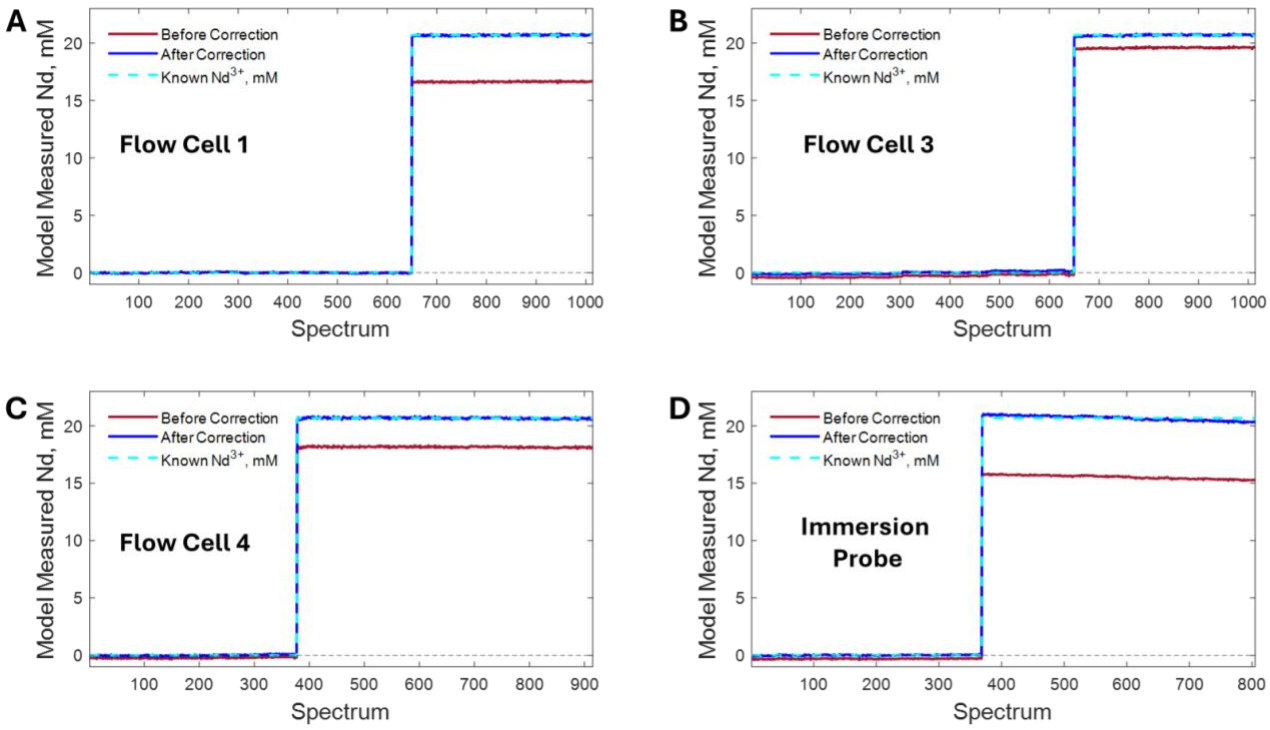


Figure 16. UV-vis model results for Nd^{3+} concentration measured across the blank and calibration solutions at the start of the first week of tank transfers and used for the slope and intercept correction. The model measured Nd^{3+} concentration is shown before and after the correction was applied to the models.

The tank transfer data was run through the updated models, and an example partial tank transfer is shown in Figure 17 The model results were generally in better agreement with the known surrogate concentration after the slope and intercept correction was applied. Note that the pump pulses the solution, resulting in segments where the measured concentration is zero. For the UV-vis measurements, spectra collected where the flow cell was empty were not removed because, unlike for Raman, the model accurately predicted a concentration of zero.

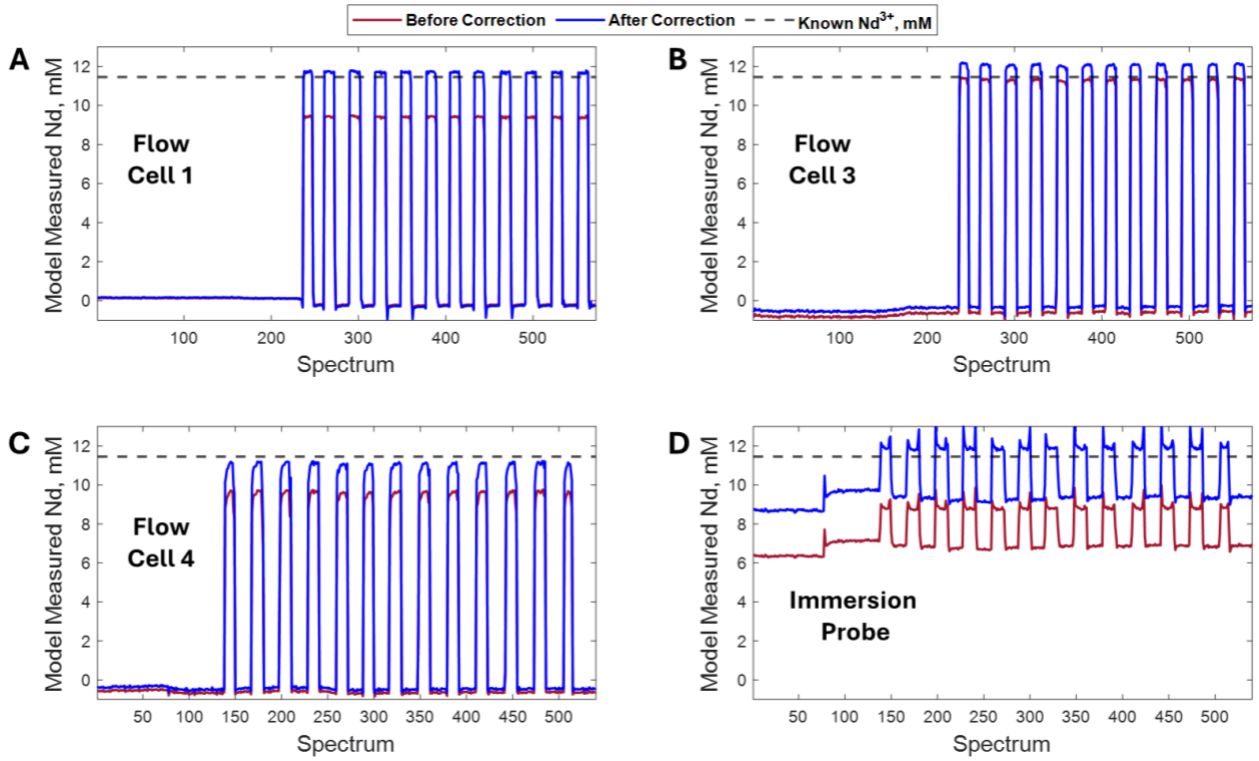


Figure 17. UV-vis model results for Nd^{3+} concentration measured across a partial tank transfer of the undiluted surrogate before and after the slope and intercept correction was applied to the models.

The same slope and intercept correction was applied to the Raman data and the results of the blank and calibration solutions are shown in Figure 18. The correction improved the prediction of the calibration solution but did not improve the prediction of an example partial tank transfer shown in Figure 19, though the deviation from expected values was relatively small.

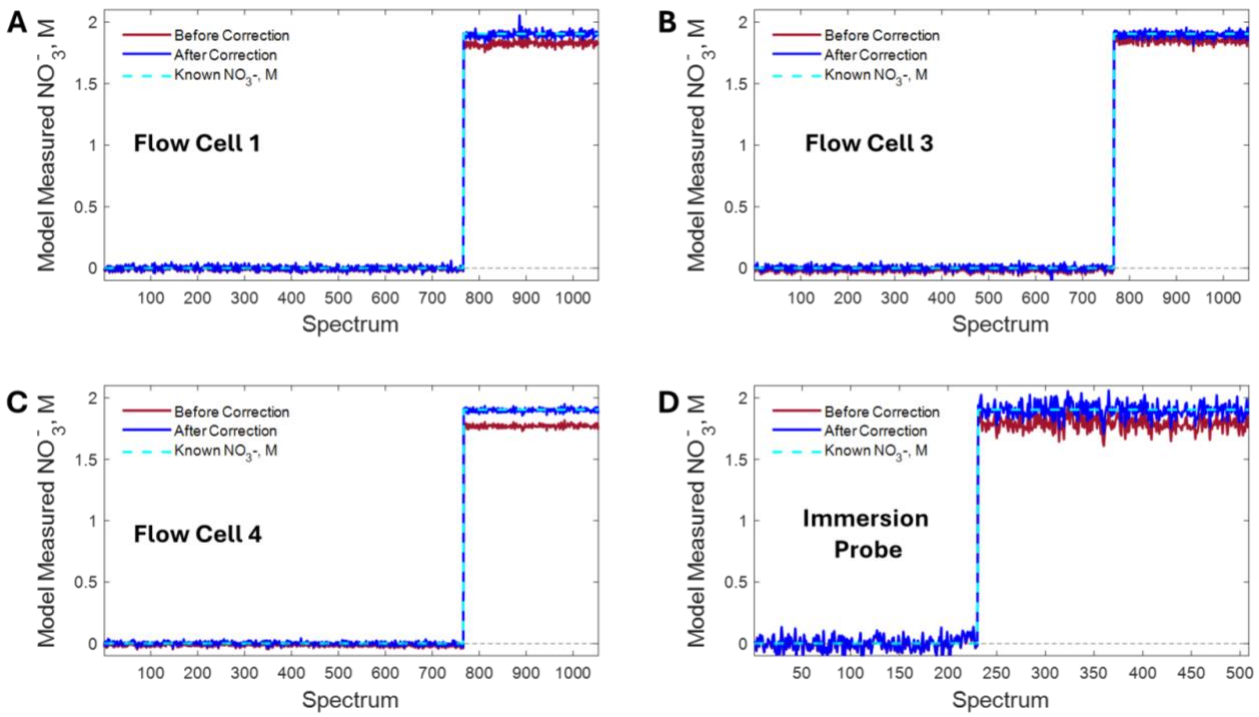


Figure 18. Raman model results for calibration solution NO_3^- concentration measured across the blank and calibration solutions at the start of the first week of tank transfers and used for the slope and intercept correction. The model measured NO_3^- concentration is shown before and after the correction was applied to the models.

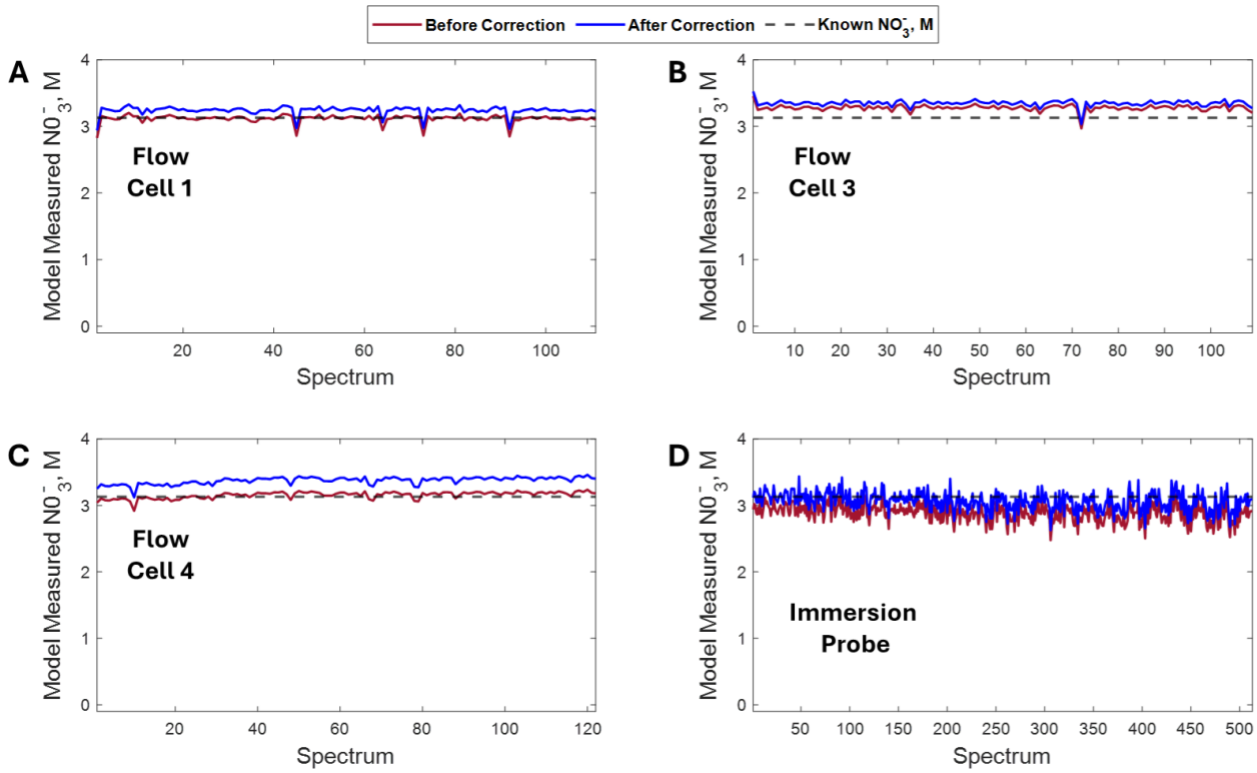


Figure 19. Raman model results for surrogate solution NO_3^- concentration measured across a partial tank transfer of the undiluted surrogate before and after the slope and intercept correction was applied to the models.

At the start of the second week of tank transfers of the diluted surrogate, the blank and calibration solutions were again measured and used for a slope and intercept correction. This analysis was done iteratively, meaning that the updated models from the previous week were corrected a second time. The results comparing the slope and intercept corrected model results from the first week to the second week are shown in Figure 20. There is less correction needed for this second iteration which means there was less change in the instrument performance or flow system characteristics between the first and second week of measurements. The results for a partial tank transfer are shown in Figure 21 and Figure 22. There wasn't a significant change in the models for the diluted surrogate solutions.

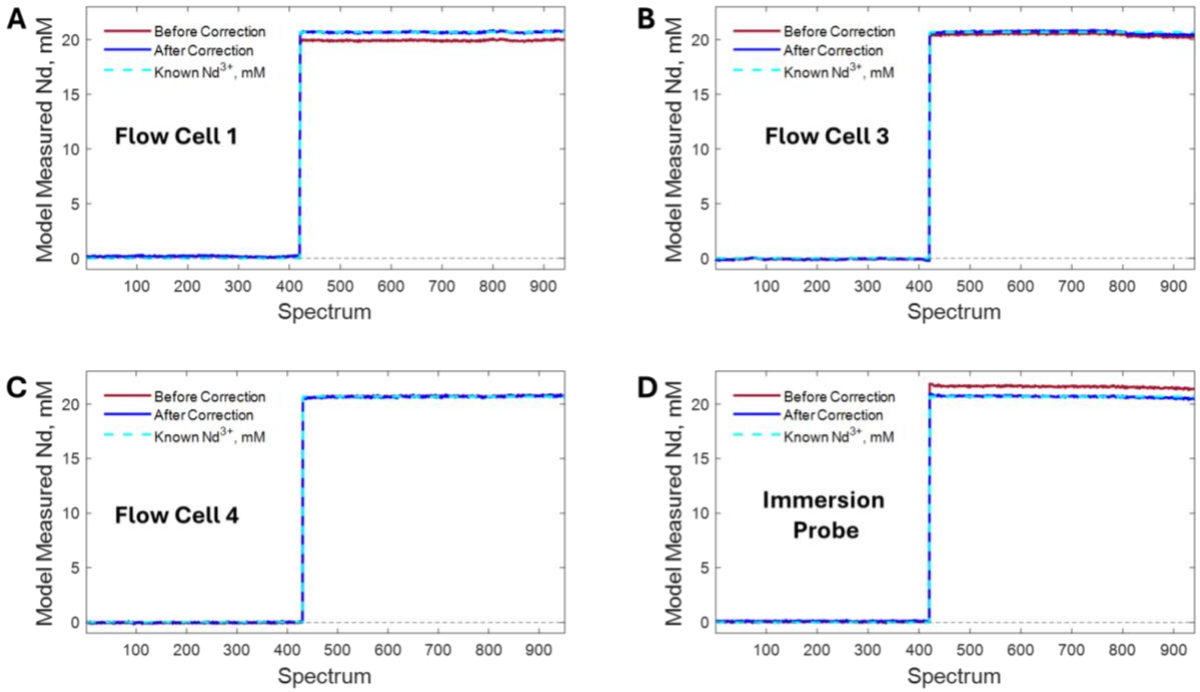


Figure 20. UV-vis model results for Nd^{3+} concentration measured across the blank and calibration solutions at the start of the second week of tank transfers and used for the slope and intercept correction. The model measured Nd^{3+} concentration is shown before and after the correction was applied to the models.

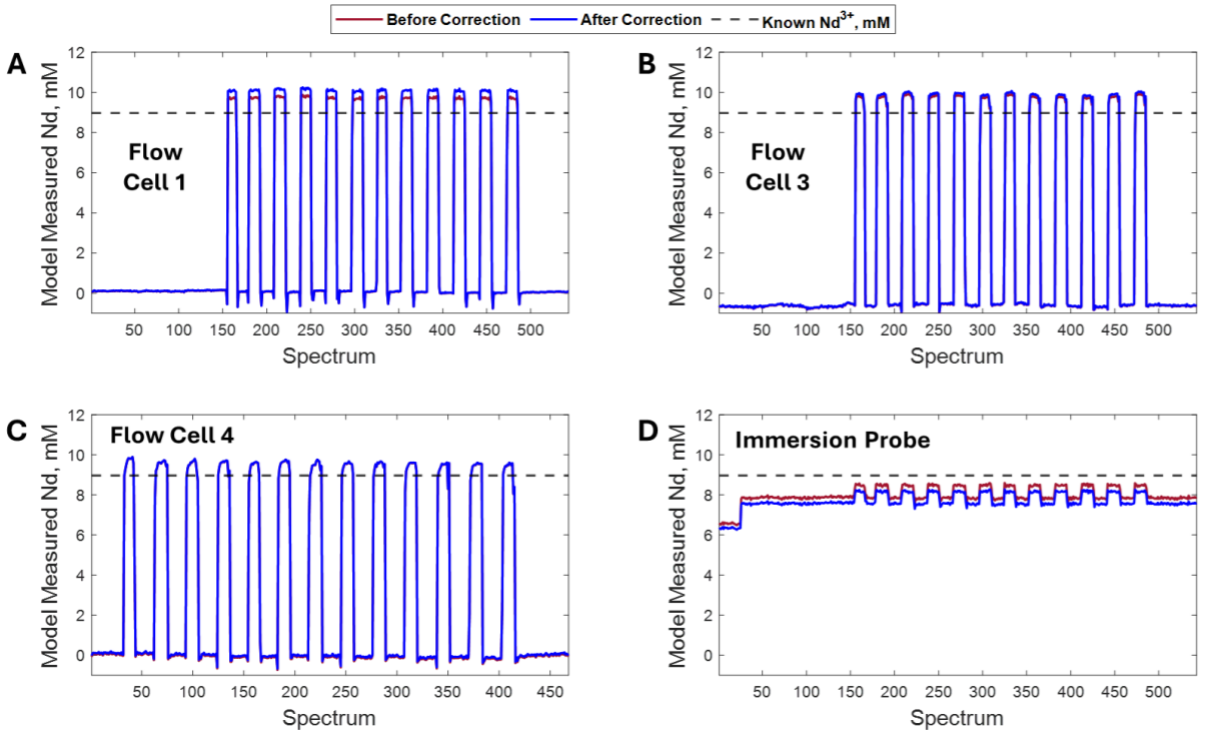


Figure 21. UV-vis model results for Nd^{3+} concentration measured across a partial tank transfer of the first dilution of the surrogate before and after the slope and intercept correction was applied to the models.

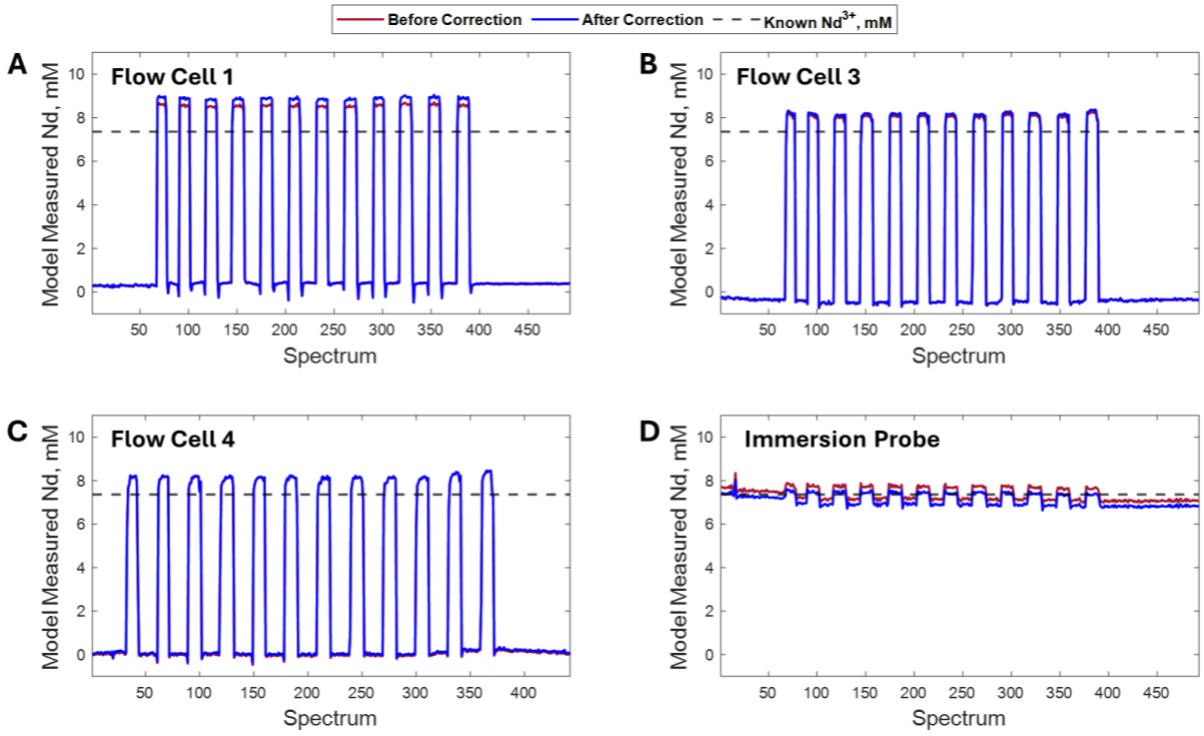


Figure 22. UV-vis model results for Nd^{3+} concentration measured across a partial tank transfer of the second dilution of the surrogate before and after the slope and intercept correction was applied to the models.

The same analysis was performed on the Raman data where only cell 3 showed significant change in the calibration model results before and after the second slope and intercept correction, as shown in Figure 23. The model under predicted the calibration solution. Partial tank transfers of the first and second dilution of the surrogate are shown in Figure 24 and Figure 25. Here the most significant change was the overprediction of cell 3 for both dilutions of the surrogate. The underprediction of the calibration solution caused the corrected model to overpredict the diluted surrogate solutions. This is an example where more frequent or more extensive calibration of the instruments during deployments would be beneficial rather than relying on a single measurement at the beginning of a set of measurements.

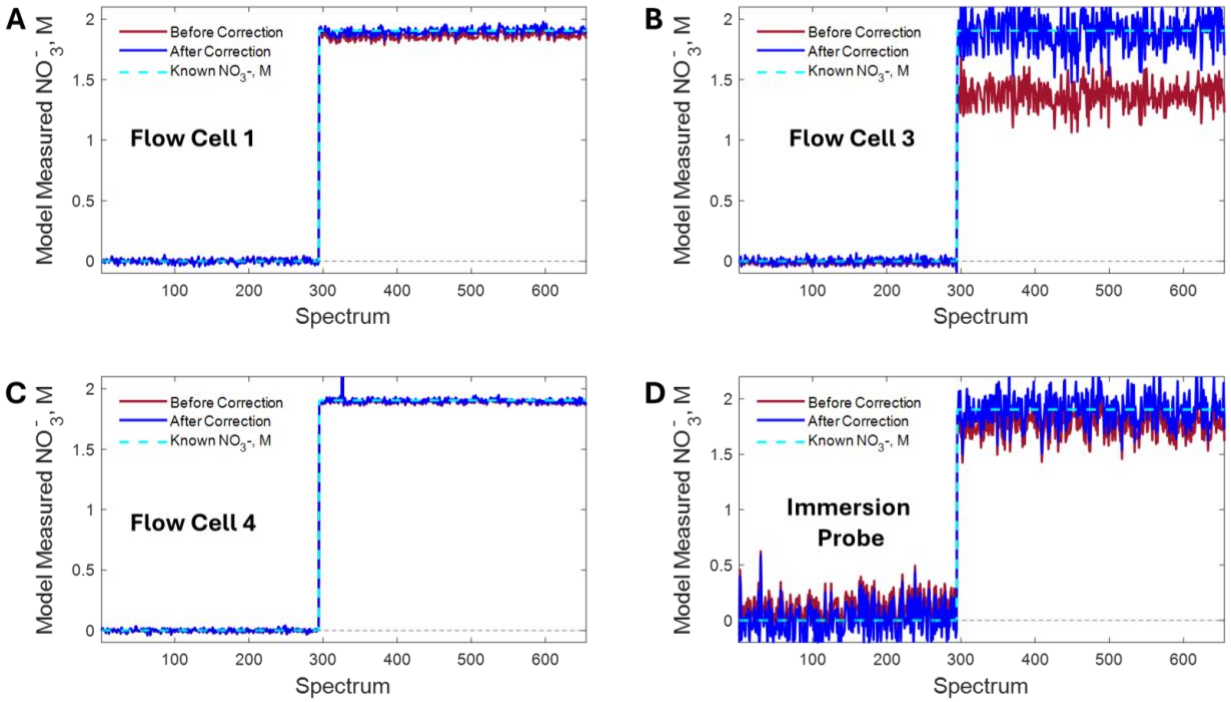


Figure 23. Raman model results for calibration solution NO_3^- concentration measured across the blank and calibration solutions at the start of the second week of tank transfers and used for the slope and intercept correction. The model measured NO_3^- concentration is shown before and after the correction was applied to the models.

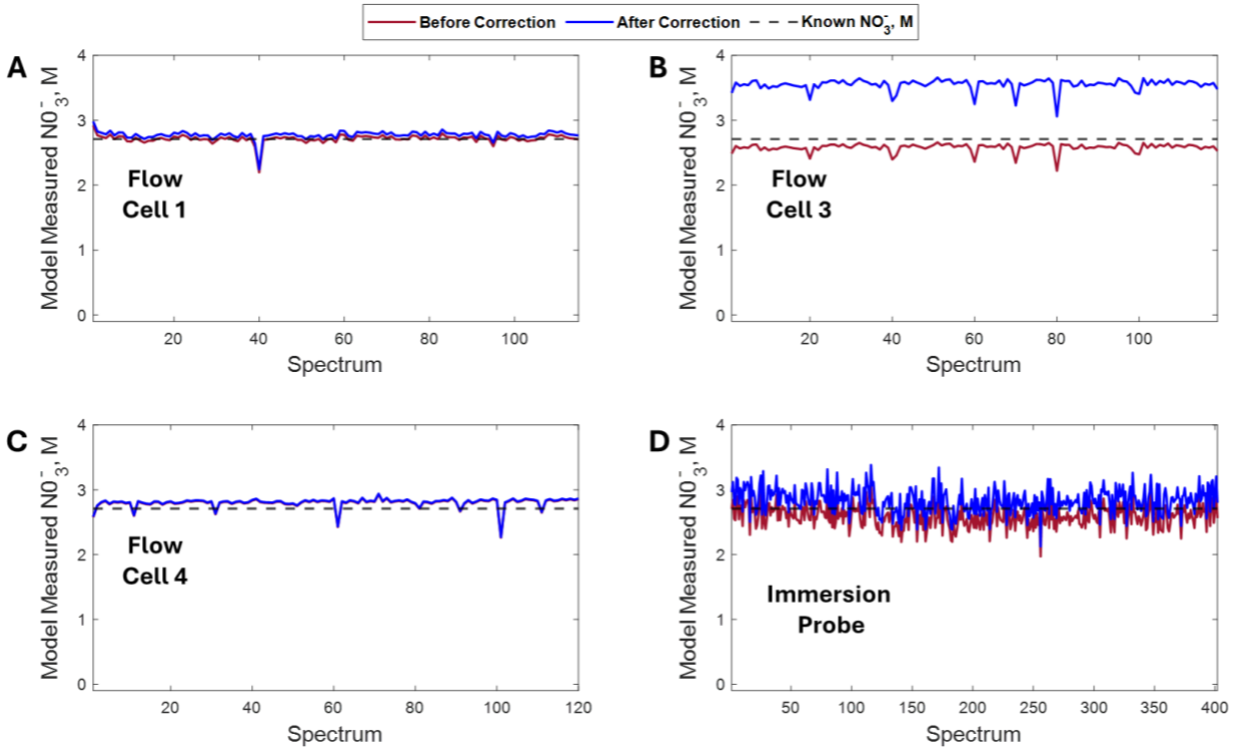


Figure 24. Raman model results for surrogate solution NO_3^- concentration measured across a partial tank transfer of the first dilution of the surrogate before and after the slope and intercept correction was applied to the models.

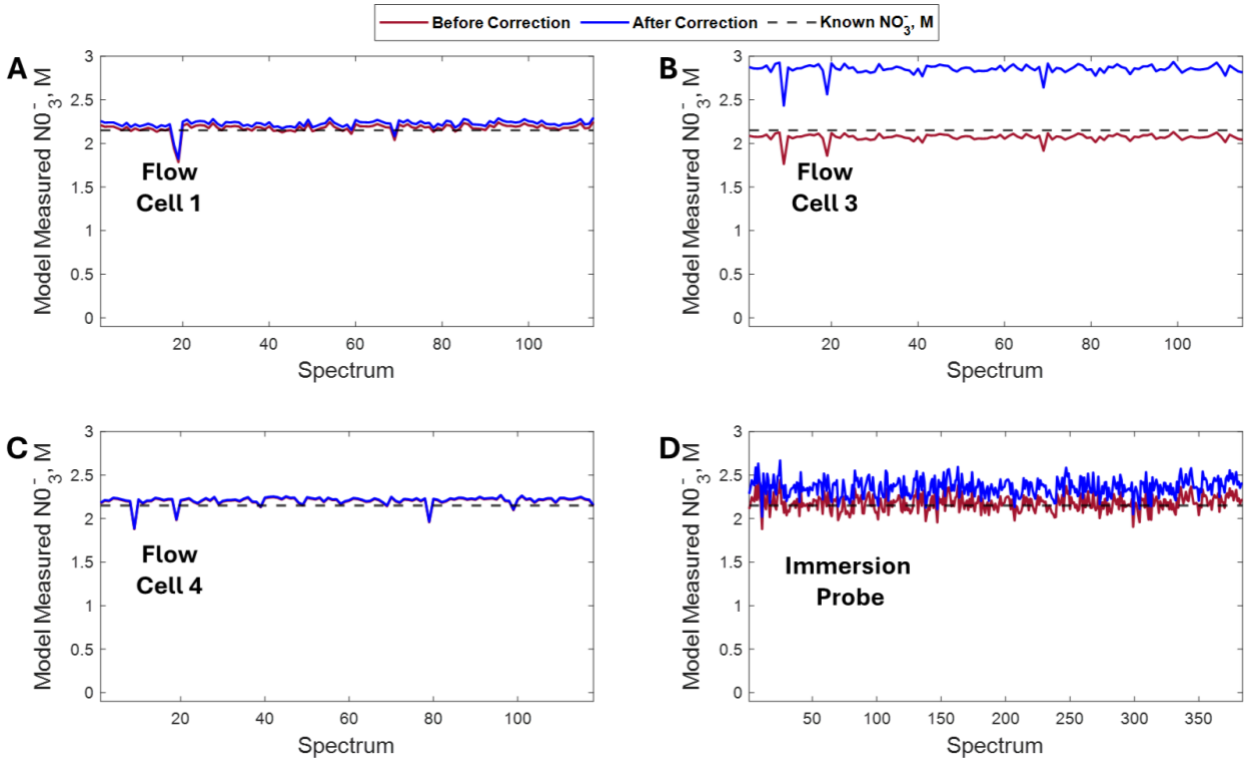


Figure 25. Raman model results for surrogate solution NO_3^- concentration measured across a partial tank transfer of the second dilution of the surrogate before and after the slope and intercept correction was applied to the models.

Table 5 details the plots included in Appendix A which include the UV-vis and Raman tank transfers performed using the undiluted surrogate and two dilutions of the surrogate. Full tank transfers with replicates were performed in addition to partial tank transfers where the first third of the tank was transferred and the second third of the tank was transferred. The flow rate was varied by changing from 2.3 to 2.0 to 1.0 Bar. A comparison was done with the recirculation on and off.

Table 5. Details of UV-vis and Raman tank transfer plots included in Appendix A.

UV-vis	Raman	Experiment	Solution	Details
Figure 41	Figure 42	Trial 1	Surrogate	Full tank transfer at 2.3 Bar, 3 replicates
Figure 43	Figure 44	Trial 2	Surrogate	Full tank transfer at 1.0 Bar, 3 replicates
Figure 45	Figure 46	Trial 3	Surrogate	Full tank transfer at 2.3, 2.0, 1.0 Bar
Figure 47	Figure 48	Trial 4	Surrogate	First third tank transfer at 2.3, 2.0, 1.0 Bar
Figure 49	Figure 50	Trial 5	Surrogate	Second third tank transfer at 2.3, 2.0, 1.0 Bar
Figure 51	Figure 52	Trial 6	Surrogate	Recirculation on and off
Figure 53	Figure 54	Trial 7	First dilution	Full tank transfer at 2.3 Bar, 3 replicates
Figure 55	Figure 56	Trial 8	First dilution	Full tank transfer at 2.3, 2.0, 1.0 Bar
Figure 57	Figure 58	Trial 9	First dilution	First third tank transfer at 2.3 Bar, 3 replicates
Figure 59	Figure 60	Trial 10	First dilution	Second third tank transfer at 2.3 Bar, 3 replicates
Figure 61	Figure 62	Trial 11	Second dilution	Full tank transfer at 2.3 Bar, 3 replicates
Figure 63	Figure 64	Trial 12	Second dilution	Full tank transfer at 2.3, 2.0, 1.0 Bar
Figure 65	Figure 66	Trial 13	Second dilution	First third tank transfer at 2.3 Bar, 3 replicates
Figure 67	Figure 68	Trial 14	Second dilution	Second third tank transfer at 2.3 Bar, 3 replicates
Figure 69	Figure 70	Trial 15	Second dilution	First third tank transfer at 2.3, 2.0, 1.0 Bar
Figure 71	Figure 72	Trial 16	Second dilution	Second third tank transfer at 2.3, 2.0, 1.0 Bar

5.0 Materials Accountancy and Uncertainty

The project's objective is to demonstrate an advanced real-time nuclear materials accountancy system for reprocessing spent nuclear fuel that achieves less than $\pm 1\%$ uncertainty level of accuracy for individual constituents (Arm, Enderlin, and Lines 2023). To this end, it is necessary to define the equations and uncertainty framework used to quantify the contributions of each relevant quantity in the uncertainty of the final mass balance for each constituent material. This challenge is more complex than initially apparent due to the assumptions required in uncertainty contributions from individual sensors, operational realities such as hold up, and even environmental impacts such as facility temperature. While the uncertainty goal was achieved here under a set of assumptions, perhaps the more valuable finding was advancing the understanding of what assumptions are required and where further R&D is necessary to verify assumptions and further reduce uncertainties.

In holistic terms, the experimental apparatus described in Section 2.0 consists of two tanks connected by a transfer pipe that is suspended from scaffolding. The supply tank, Tank 1, is instrumented with a floor scale, referred to as WIT-200, one UV-vis immersion probe, and one Raman immersion probe, both referenced as track T05. The receipt tank, Tank 2, is instrumented with a floor scale, WIT-300. Between the two tanks, a Coriolis flowmeter, AIT-250, is installed in the transfer pipe and provides simultaneous mass flow rate (kg/min), volumetric flow rate (L/min), and fluid density (kg/L) at 10 Hz. Three UV-vis sensors and three Raman sensors (tracks T01, T03, and T04) are mounted in the parallel flow cells along the transfer pipe and used along with chemometric modeling to estimate inline concentration of the relevant analytes. Liquid is transferred between Tank 1 and Tank 2 via a power fluidics pump operating in a repeating three-phase cycle: charge (suction valve V-101 open), drive (drive valve V-102 open), and drain (both valves closed). During the drain phase the flowmeter records negative mass flow, corresponding to backflow from the pipe into the supply tank. The power fluidics pump apparatus and charge vessel are suspended from scaffolding and hang inside the supply tank, below or above the liquid level depending on the amount of liquid in Tank 1. A sump pump is located in Tank 2, which can pump liquid from the receipt tank back to the supply tank via a pipe located at the bottom of the tanks.

Readings from each sensor are made discretely, with a fixed, sensor-specific, temporal resolution. To compute the cumulative transferred mass, incremental measurements are summed from the start of the trial at time t_0 to the current time, t_i. Each of the measured quantities included in the mass transfer calculations have different systematic biases and uncertainty magnitudes. This means that the true mass transferred may not be equal to the measured value. By quantifying the uncertainties of each measured quantity, accounting for potential correlations between these measurements, and combining the individual uncertainties, uncertainty quantification allows us to determine a range around the measured mass transfer that theoretically contain the true value. In the subsections that follow, we will introduce the mass transfer equations and describe the tools used in the real-time uncertainty analysis.

5.1 Problem definition

For each trial and replicate, the initial mass of the solution is measured using WIT-200 at time t_0,

$$m_{\text{total}}(t_0) = m_{\text{WIT}-200}(t_0).$$

At time t_i, the total incremental mass transferred, $\Delta m_{\text{total}}(t_i)$, also referred to as the mass delta, can be estimated from three independent sources. For the first two sources, the mass transferred can be measured by the change in WIT-200 readings between time t_i and time t_{i-1},

$$\Delta_{\text{WIT}-200} m_{\text{total}}(t_i) = m_{\text{WIT}-200}(t_{\text{i}-1}) - m_{\text{WIT}-200}(t_{\text{i}}),$$

referred to as the supply scale delta, or by the change in the WIT-300 readings between time t_i and time t_{i-1},

$$\Delta_{\text{WIT}-300} m_{\text{total}}(t_i) = m_{\text{WIT}-300}(t_{\text{i}}) - m_{\text{WIT}-300}(t_{\text{i}-1}),$$

referred to as the receipt scale delta. Note that the order of the terms in the difference is reversed between these two equations because the mass measured by WIT-300 is increasing with time while the mass measured by WIT-200 is decreasing with time. For the third source, the incremental mass transferred can be computed as the instantaneous mass flow measured by the flowmeter, AIT-250, at time t_i, multiplied by the change in time between measurements,

$$\Delta_{\text{AIT}-250} m_{\text{total}}(t_i) = \dot{m}_{\text{AIT}-250}(t_i)(t_i - t_{i-1}).$$

This estimate of the total incremental mass transferred is referred to as the flowmeter delta.

The total mass transferred at time t_i is computed as the sum of the incremental masses from time t_0 to time t_i,

$$m_{\text{total}}(t_i) = \sum_{j=0}^{i} \Delta m_{\text{total}}(t_j),$$

using any of the previously described mass deltas.

5.1.1 Analyte-specific mass balance

For each solution described in Table 2, the initial analyte concentrations of sodium nitrate and neodymium nitrate are computed via a lab standard addition as reported in Table 12. We refer to these reference values as, $c^{\text{LSA}}_{\text{NO}_3^-}(t_0)$, and $c^{\text{LSA}}_{\text{Nd}^{3+}}(t_0)$, respectively. Using these values, the initial mass of each analyte is computed as the product

$$m_{\text{NO}_3^-}(t_0) = c^{\text{LSA}}_{\text{NO}_3^-}(t_0) m_{\text{WIT}-200}(t_0), \text{ and}$$

$$m_{\text{Nd}^{3+}}(t_0) = c^{\text{LSA}}_{\text{Nd}^{3+}}(t_0) m_{\text{WIT}-200}(t_0),$$

respectively.

Beyond the initial concentrations of each analyte in each solution, analyte concentrations during the trials are estimated by applying trained partial least squares regression (PLS) models to the spectra measured by the UV-vis and Raman immersion probes and in-line sensors. More details

about the chemometric modeling can be found in Section 4.0. Each sensor provides an independent estimate of the analyte concentration at time t_i. To keep track of the different estimates, the concentration at time t_i is written with the track/flow cell number (T01, T03, T04, or T05) as the superscript and the analyte listed in the subscript. For example, the concentration of sodium nitrate at time t_i estimated via the sensor in track/flow cell T01 is denoted by $c^{\mathrm{T01}}_{\mathrm{NO_3^-}}(t_i)$.

For each analyte, the associated incremental mass transferred can then be computed by multiplying the analyte concentration by the appropriate mass delta. For example, the sodium nitrate supply scale delta with concentration estimated by inline sensor T01 can be computed as

$$\Delta_{\mathrm{WIT-200}} m^{\mathrm{T01}}_{\mathrm{NO_3^-}}(t_i) = c^{\mathrm{T01}}_{\mathrm{NO_3^-}}(t_i)\Delta_{\mathrm{WIT-200}} m_{\mathrm{total}}(t_i),$$

and the neodymium nitrate flowmeter delta with concentration estimated by the immersion probe T05 is

$$\Delta_{\mathrm{AIT-250}} m^{\mathrm{T05}}_{\mathrm{Nd^{3+}}}(t_i) = c^{\mathrm{T05}}_{\mathrm{Nd^{3+}}}(t_i)\Delta_{\mathrm{AIT-250}} m_{\mathrm{total}}(t_i).$$

The other combinations are computed in an analogous fashion.

The analyte mass transferred at time t_i and the error in the analyte mass balance at time t_i are computed analogously to those for the total mass, with total mass deltas replaced by the appropriate analyte mass deltas. For example, if we generically write the sodium nitrate mass delta as $\Delta m_{\mathrm{NO_3^-}}(t_j)$, then the cumulative mass of sodium nitrate transferred at time at time t_i is

$$m_{\mathrm{NO_3^-}}(t_i) = \sum_{j=0}^{i} \Delta\, m_{\mathrm{NO_3^-}}(t_j).$$

5.1.2 Mass balance error

The error in the total mass balance at time t_i is computed as the difference between the initial total mass and total mass transferred, plus the mass remaining in the supply tank,

$$\mathrm{err}_{\mathrm{total}}(t_i) = m_{\mathrm{total}}(t_0) - \left(m_{\mathrm{total}}(t_i) + m_{\mathrm{WIT-200}}(t_i)\right).$$

Similarly, the error of the constituent material-specific mass balance at time t_i (using sodium nitrate as an example) is

$$\mathrm{err}_{\mathrm{NO_3^-}}(t_i) = m_{\mathrm{NO_3^-}}(t_i) - \left(m_{\mathrm{NO_3^-}}(t_i) + c^{\mathrm{T05}}_{\mathrm{NO_3^-}}(t_i) m_{\mathrm{WIT-200}}(t_i)\right),$$

where the mass of sodium nitrate that remains in Tank 1 at time t_i is computed as the mass measured by WIT-200 times the concentration estimated using the immersion probe T05.

5.2 Uncertainty quantification background

As the equations described here will apply to many of the quantities included in the mass balance equations, they will be written generically. Suppose that the quantity of interest is a function of

multiple variables, $y = f(x_1, x_2, \ldots, x_N)$. The traditional calculus-based approach to uncertainty estimation expands the function in a first-order Taylor series, deletes the higher-order terms, and calculates the variance of the estimated quantity assuming the errors in the measured quantities are uncorrelated. That is,

$$u_c^2(y) = \sum_{i=1}^{N} \left(\frac{\partial f}{\partial x_i}\right)^2 u^2(x_i)$$

where $\partial f / \partial x_i$ are the sensitivity coefficients and $u^2(x_i)$ is the uncertainty for variable x_i for $i = 1, \ldots, N$. However, the uncorrelated assumption is not always well founded, and when the correlations are unknown, it can also be useful to estimate the interactions between variables using Monte Carlo simulations (Gardenier, Gui, and Demas 2011). In this scenario, a distribution is defined for each variable, and statistics are estimated by drawing all variables jointly from the collection of distributions.

Uncertainty quantification (UQ) is the process of characterizing the range of values within which a measurand is expected to lie, given imperfect knowledge of the measurement process. In the context of mass balance for liquid transfer experiments, UQ requires tracking how uncertainty propagates from raw sensor readings, e.g., floor scales, a Coriolis flowmeter, and optical spectroscopy sensors, through calibration corrections, chemometric models, and numerical integration to a final reported analyte mass. This section summarizes the mathematical background necessary for the techniques used in this work.

5.2.1 GUM

The *Guide to the Expression of Uncertainty in Measurement* (GUM) ("Evaluation of measurement data—Guide to the expression of uncertainty in measurement" 2008) is an international standard for quantifying uncertainty in measurements as they are propagated through equations. Uncertainty as the result of a measurement may be grouped into two categories according to the way in which their numerical value is estimated:

Type A evaluation is based on statistical analysis of a series of repeated observations. The standard uncertainty is estimated as the sample standard deviation of the mean:

$$u_A(\bar{x}) = \frac{s}{\sqrt{n}} = \sqrt{\frac{1}{n(n-1)} \sum_{i=1}^{n} (x_i - \bar{x})^2}$$

where s is the sample standard deviation and n is the number of observations. Type A uncertainties are reduced by averaging: taking more readings decreases u_A at a rate of $1/\sqrt{n}$.

Type B evaluation uses information other than repeated observations, like manufacturer specifications, calibration certificates, physical reasoning, or prior experience. The standard uncertainty is inferred from the stated limits or bounds on the quantity.

The Type A and Type B categories both apply to *uncertainty* and are not substitutes for the words "random" and "systematic".

The standard uncertainty of the result of a measurement, when that result is obtained from the values of a number of other quantities, is termed *combined standard uncertainty* and denoted by u_c. It is the estimated standard deviation associated with the result and is equal to the positive square root of the combined variance obtained from all variance and covariance components, however evaluated, using the *law of propagation of uncertainty("Evaluation of measurement data—Guide to the expression of uncertainty in measurement" 2008)*. For a measurement model $y = f(x_1, x_2, \ldots, x_N)$ in which the input quantities x_i are independent, the GUM law of propagation of uncertainty gives the combined standard uncertainty as:

$$u_c^2(y) = \sum_{i=1}^{N} \left(\frac{\partial f}{\partial x_i}\right)^2 u^2(x_i)$$

where $\partial f / \partial x_i$ are the sensitivity coefficients. This first-order Taylor expansion is the basis for all analytic uncertainty propagation in this work. As part of this work, software was developed in which arithmetic operations automatically propagate variances according to this formula and maintain a labeled contributions dictionary that maps each source to its variance contribution for budget reporting.

Typically, for a quantity, y, that varies randomly, we will estimate its expected value, y, as the arithmetic mean of n observations obtained under the same conditions. For example, in order to quantify the uncertainty of the total mass of the system, we can take multiple measurements of the total mass as input and use the average of those measurements as the estimated value for the total mass. This allows us to estimate the variance of these readings, and in turn quantify the uncertainty. The number of observations needs to be chosen large enough to reliably estimate the expected value and variance. If the distribution of independent observations of the quantity of interest follows a normal distribution, then we can further quantify the relative uncertainty of our estimate of the standard deviation, $\bar{y}/u(y)$, as function of the number of observations, $1/\sqrt{2(n-1)}$, which can provide confidence intervals for our estimated uncertainties.

For measurements that are a function of time, or cannot be taken multiple times independently, we may obtain the estimated value of an input quantity from a curve that has been fitted to experimental data by the method of least squares. In this case, there are standard techniques for estimating variance from the predicted values that are standard in the literature (Fuller 1987).

In line with our success criteria of $\pm 1\%$ uncertainty, we will typically report the relative uncertainty,

$$u_r(y) = 100 * \frac{u_c(y)}{|y|},$$

which is a percentage, because the units of $u_c(y)$ and y cancel out.

5.2.2 Floor scale uncertainty model

The mass of the pump apparatus, charge vessel, transfer pipe, inline sensors, and the mass of the liquid in the transfer pipe are not being measured by either floor scale during operation because they are suspended from external scaffolding. However, the hardware located inside Tank 1 and Tank 2 still affects mass measurements by vertically displacing liquid in each tank as a function of the liquid volume in the respective tank at time t, increasing the downward force on the floor scales.

To reconcile these differences, the WIT-200 and WIT-300 floor scales were cross-calibrated against a reference scale, WS-10, by incrementally transferring 100 kg of water (as measured by WS-10) into each tank. The calibration range covered 677–5019 kg for WIT-200 and 487–4318 kg for WIT-300. Both scales were found to read systematically high relative to WS-10: WIT-200 by 0.5–1.1% (increasing with load) and WIT-300 by 0.2–0.8%.

Because WS-10 was not independently calibrated, the corrections establish the relative relationship between the two floor scales rather than their absolute accuracy. Monotone cubic spline corrections (PCHIP) (Fritsch and Butland 1984) were fitted to the calibration data and applied to all scale readings used in the mass balance computation, with calibration fit uncertainty estimated by leave-one-out cross-validation (LOO-RMSE = 0.463 kg for WIT-200, 0.418 kg for WIT-300).

As a result, the floor scales WIT-200 and WIT-300 exhibit three distinct uncertainty components that behave differently when readings are averaged:

Systematic (proportional) component: Represents calibration bias that scales with the measured load. Calibration of WIT-200 against the reference scale WS-10 over 42 dollop measurements revealed a systematic positive bias ranging from 0.498 at low load to 1.130 at high load. WIT-300 showed a smaller and more stable bias of 0.154 to 0.803 over 35 measurements. This bias is the same for every reading at a given load and is **not** reduced by averaging:

$$u_{\text{sys}}(m) = s \cdot m$$

where s is the fractional slope coefficient (e.g. $s = 0.001$ for a 0.1 systematic uncertainty). Figure 26 shows the effect of this calibration applied to the combined mass measured by both floor scales during a full-tank transfer. Assuming no loss of liquid, we would expect the initial mass and final mass to be the same. The raw data shows a difference between the initial mass and final mass that is significantly reduced by calibration.

Random (floor) component: Represents independent noise on each reading, e.g., electrical noise, vibration, resolution limits, etc. Unlike the systematic component, this is reduced by averaging over n readings:

$$u_{\text{rand}}(m) = \frac{c}{\sqrt{n}}$$

where c is the constant floor uncertainty in kg.

The combined scale uncertainty for a mean of n readings at load m is:

$$u(m,n) = \sqrt{u_{\text{sys}}^2(m) + u_{\text{rand}}^2(m,n)} = \sqrt{(s \cdot m)^2 + \left(\frac{c}{\sqrt{n}}\right)^2}$$

At the operating loads in these experiments, the systematic component dominates. For example, for $s = 0.001$ and $m = 5980$ kg, we have $u_{\text{sys}} \approx 5.98$ kg, which greatly exceeds the random floor $c/\sqrt{n}$ for any practical averaging window.

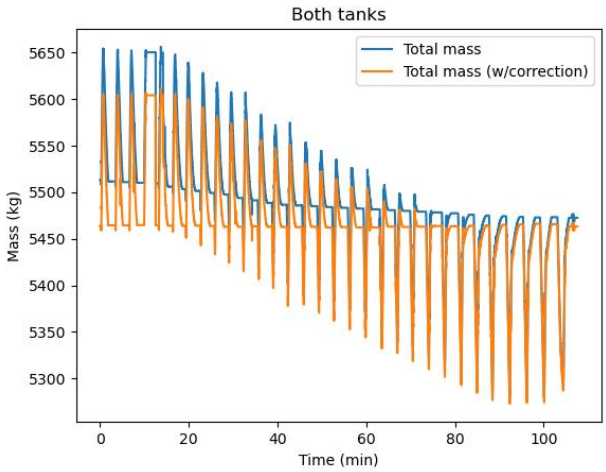


Figure 26. Floor scales under the supply and receipt tanks were calibrated by standardizing readings to those of a third scale measuring a fixed, known volume of water. The blue curve represents the raw combined mass measured by both floor scales during one full-tank transfer and the orange curve represents the combined readings after calibration-correction.

Floor scale cross-calibration component: The third floor-scale uncertainty source arises from the non-linear cross-calibration correction. This term is applied to each scale reading and added in quadrature with the intrinsic scale uncertainty:

$$u_{\text{total}}(m,n) = \sqrt{u_{\text{sys}}^2(m) + u_{\text{rand}}^2(m,n) + u_{\text{cal}}^2}.$$

5.2.3 Monte Carlo simulation

When the measurement model is highly non-linear, when there are partial correlations between variables, when input distributions are non-Gaussian, or when the first-order Taylor expansion of the GUM is inadequate, Monte Carlo simulation (MCS) provides a more general alternative. This is done by defining a distribution for each variable in such a way that models the observations and then performing joint random draws from the defined distributions. Of course, it is infeasible to perform such an analysis by hand, so many software packages have been developed specifically for this purpose(Albert 2020), (Gardenier, Gui, and Demas 2011), (Tennøe, Halnes, and Einevoll

2018). The approach, formalized in JCGM 101:2008("Evaluation of measurement data—Guide to the expression of uncertainty in measurement" 2008), propagates uncertainty by:

1. Draw N random samples from the probability distributions assigned to each input quantity
2. Evaluate the measurement model for each sample
3. Characterize the output distribution from the resulting N model evaluations

In this work, Monte Carlo methods are used for the uncertainty of PLS-predicted concentrations. For each spectrum, $\mathrm{x} \in \mathbb{R}^M$, with M observed wavelength bands, N perturbed spectra are generated by adding random noise drawn from the estimated per-wavelength noise distribution:

$$\mathrm{x}_m = \mathrm{x}_m + \varepsilon_m, \quad \varepsilon_m \sim U(-b_m, b_m)$$

for $m = 1, \ldots, M$, where $b_m \in \mathbb{R}$ is the maximum absolute deviation from the mean at each wavelength. Each perturbed spectrum is then passed through the PLS model to obtain a predicted concentration $\widehat{c_k}$. The standard deviation of $\{\hat{c}_k\}_{k=1}^N$ characterizes the uncertainty due to spectral noise alone.

The bounds, $b_m \in \mathbb{R}$, were derived for the Raman ($M = 1650$) and UV-vis ($M = 2000$) chemometric models independently, with unique bounds computed for each of Track 01, 03, 04, and 05 from track-specific calibration data. The calibration dataset consists of 28 spectra representing replicate measurements of the analyte (NO_3^- and Nd^{3+}) concentrations, split into 7 groups of 4 per modality. Given a group, g,with 4 calibration spectra, the mean at wavelength m, $\mu_m^{(g)}$, is computed as

$$\mu_m^{(g)} = \frac{1}{4}\sum_{j=1}^{4} x_{m,j}^{(g)}$$

where $x_{m,j}^{(g)}$ is the mth wavelength of the jth spectra in group g. Using these values, we compute the mean-centered minimum and maximum within each group,

$$b_m^{(g)-} = \mu_m^{(g)} - \min_j x_{m,j}^{(g)}, \text{ and } \quad b_m^{(g)+} = \max_j x_{m,j}^{(g)} - \mu_m^{(g)},$$

keeping the larger of the two as the group-specific maximum deviation,

$$b_m^{(g)} = \max\left\{b_m^{(g)-}, b_m^{(g)+}\right\}$$

and save the largest magnitude deviation at wavelength m as the symmetric bound for the uniform distribution,

$$b_m = \max_g \; b_m^{(g)}.$$

This conservative approach was adopted to capture the worst-case deviation curve over the wavelength by capturing the largest deviation found in any group. The goal of this approach is to represent the worst-case uncertainty.

5.2.3.1 Derived perturbation bounds

Using this approach, perturbation bounds were computed for each of the four tracks for Raman and UV-vis, respectively. Figure 27 visualizes the spectral perturbation bounds computed for Raman spectra from Track 01, 03, 04, and 05 as a function of wavelength, and Figure 28 shows the analogous plots for UV-vis spectra.

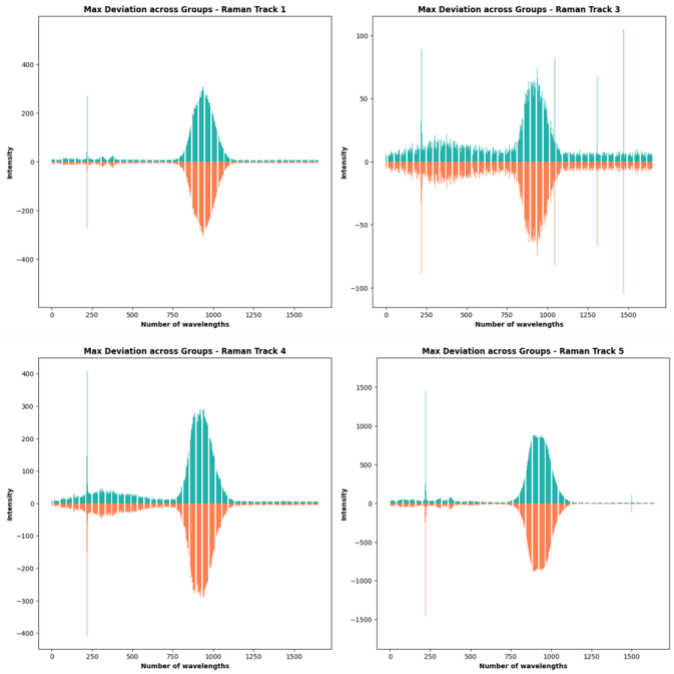


Figure 27. Monte Carlo simulation perturbation bounds of Raman data for Track 01 (upper left), Track 03 (lower left), Track 04 (upper right), and Track 05 (lower right).

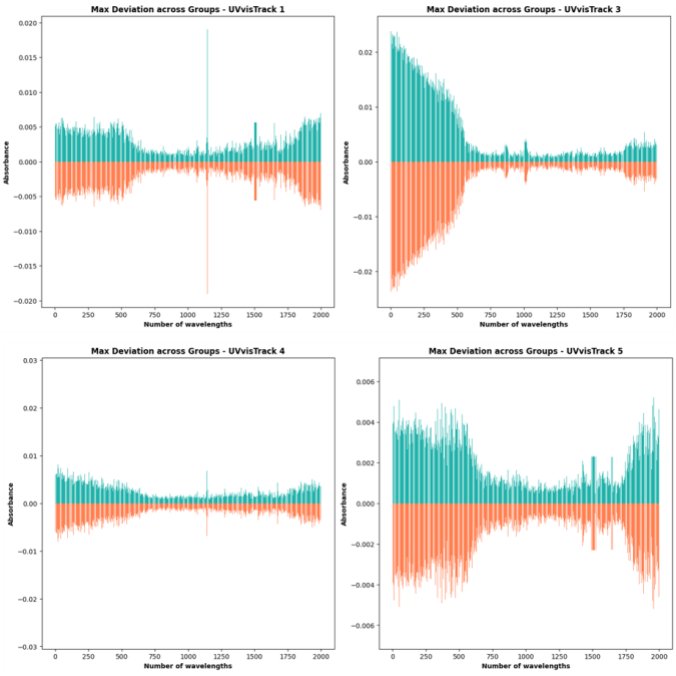


Figure 28. Monte Carlo simulation perturbation bounds of UV-vis data for Track 01 (upper left), Track 03 (lower left), Track 04 (upper right), and Track 05 (lower right).

These bounds were used to generate 100 perturbations for each observed spectrum. PLS chemometric model software is used to generate concentration of original spectrum and the concentration of all 100 perturbations. Mean, standard deviation and std. error are computed.

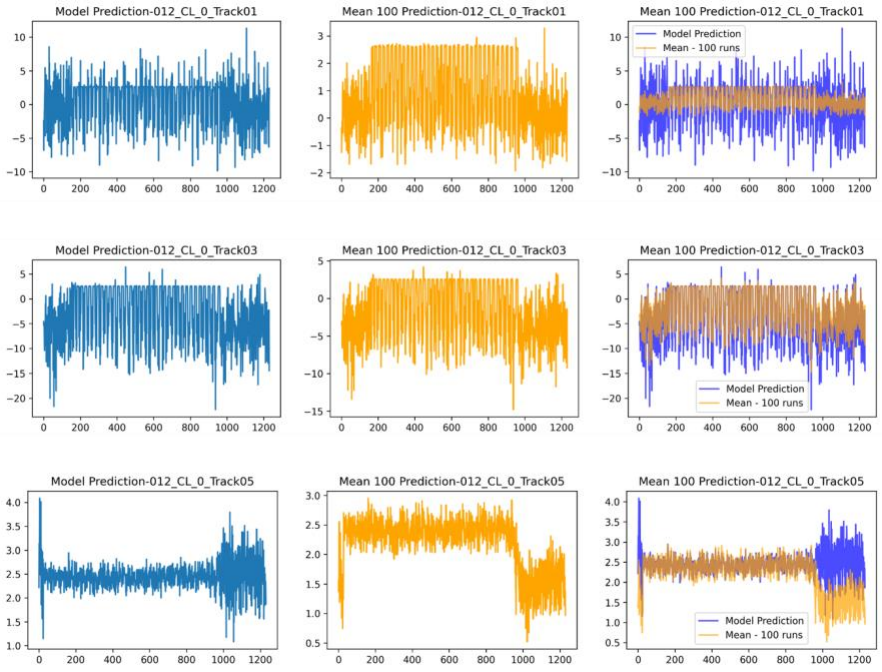


Figure 29. Model predictions of NO_3^- concentration for measured spectra (blue) and mean model predicted NO_3^- concentration for 100 perturbations (yellow).

Figure 29 and Figure 30 provide illustrative examples of the model predictions and mean for 100 perturbations generated using the bounds on NO_3^- and Nd^{3+} concentration, respectively, for all relevant tracks from Trial 10, Replication 1.

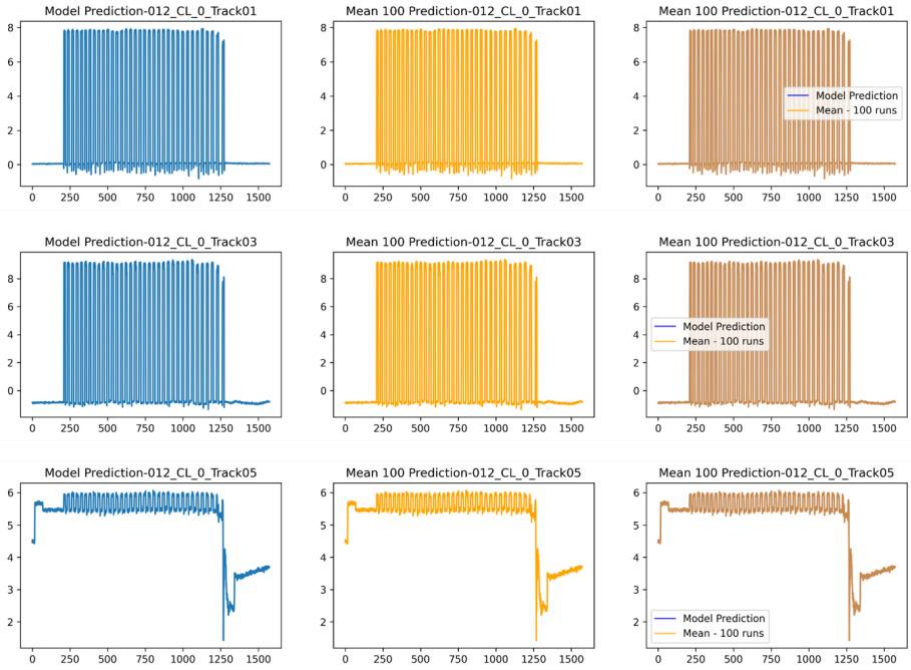


Figure 30. Model predictions of Nd^{3+} concentration for measured spectra (blue) and mean model predicted Nd^{3+} concentration for 100 perturbations (yellow).

5.2.4 Combining uncertainties

As previously discussed, when a result y depends on *independent* uncertain inputs $x_1, \ldots, x_N$, their variance contributions add in quadrature("Evaluation of measurement data—Guide to the expression of uncertainty in measurement" 2008):

$$u_c^2(y) = \sum_{i=1}^{N} \left(\frac{\partial f}{\partial x_i}\right)^2 u^2(x_i).$$

This is the primary combination rule used throughout this work. For example, the uncertainty of the analyte mass transferred is the quadrature sum of contributions from the scale uncertainty, flowmeter uncertainty, PLS model uncertainty, and concentration drift uncertainty.

5.2.4.1 Systematic vs. random components

A critical distinction in this work is between uncertainty components that are correlated across time (systematic) and those that are independent across time (random):

Systematic uncertainty, such as the flowmeter calibration bias, produces errors that are the same sign and magnitude for every reading. When the flowmeter integral is computed as $m = \sum_i \dot{m}_i \, \Delta t_i$ the systematic component does not average down: $u_{\text{sys}}(\Delta m) = r \cdot |\Delta m|$, where r is the relative uncertainty of the flowmeter.

Random uncertainty, such as electronic noise on individual readings, produces independent errors that partially cancel when summed: $u^2_{\text{rand}}(\Delta m) = \sum_i (r \cdot |\dot{m}_i| \Delta t_i)^2$.

For the flowmeter in these experiments, the systematic component dominates for transfer durations longer than a few minutes, making the relative uncertainty of the integral approximately equal to the relative uncertainty of a single reading.

5.2.4.2 Concentration drift uncertainty

A novel uncertainty source arises in this work when the most recent valid concentration measurement is carried forward (forward-filled) across time gaps during which the inline spectroscopy sensors produce invalid readings (e.g., during the pump charge and drain phases). The concentration is assumed constant at $\hat{c}_{\text{last}}$ with uncertainty u_{last}, but the true concentration may drift from this value during the gap of duration Δt. This is modeled as a random-walk inflation:

$$u(\hat{c}, t) = \sqrt{u^2_{\text{last}} + (\sigma_{\text{drift}} \cdot \Delta t)^2}$$

where σ_{drift} is the concentration drift rate in native units per second. The value of the drift rate used in this work was estimated empirically from the 95th percentile of $\Delta c / \Delta t$ between consecutive T05 tank probe spectra during active transfer, giving $\sigma_{\text{drift}} = 0.247$ mM/L/s for Nd^{3+} and $\sigma_{\text{drift}} = 0.271$ M/L/s for NO_3^- in these experiments.

5.2.4.3 Quantifying contributions to overall uncertainty

In the UQ software package developed for this work, all uncertainty contributions are tracked through every arithmetic operation by maintaining a labeled contributions dictionary. Each key identifies a source (e.g. `supply_scale_start_systematic`, `uv_vis_T01_rmsep`, `nd3_concentration_drift`) and the corresponding value is the variance contribution from that source. 28 unique sources of uncertainty were tracked per sensor type (Raman/UV-Vis). A complete list of uncertainty sources can be seen in Section 5.6, along with a summary that collects the sources into 7 broad categories. The contributions are propagated according to the GUM sensitivity coefficients and are normalized to produce a percentage-of-total-variance breakdown. This decomposition is referred to as the *Uncertainty Budget* and allows for direct identification of the dominant uncertainty source for any given measurement configuration.

5.3 Measurement consistency

A key feature of the mass balance system described in this work is the availability of multiple independent estimates of the same physical quantity. The supply scale, WIT-200, receipt scale, WIT-300, and Coriolis flowmeter, AIT-250 each provide an independent estimate of the total liquid mass transferred. Similarly, the inline pipe sensors (tracks T01, T03, and T04) and the supply tank immersion probe (track T05) each provide independent estimates of the analyte concentration. When multiple independent estimates of the same quantity are available, two questions arise: how should they be combined into a single best estimate, and are they mutually consistent with their stated uncertainties? This section addresses both questions.

5.3.1 The Birge ratio

The Birge ratio, introduced by Raymond Birge in the context of combining physical constants from disparate measurements (Birge 1932), provides a quantitative test of whether a set of independent estimates are mutually consistent with their stated uncertainties. It is widely used in metrology, notably in NIST measurement comparisons (Kacker, Kessel, and Sommer 2010) and in the CODATA least-squares adjustment of fundamental constants (Mohr, Taylor, and Newell 2008).

Given n independent estimates $x_1, x_2, \ldots, x_n$ of the same quantity, with standard uncertainty σ_i for the ith estimate, the inverse-variance weighted mean is:

$$\bar{x} = \frac{\sum_{i=1}^{n} w_i\, x_i}{\sum_{i=1}^{n} w_i}, \qquad w_i = \frac{1}{\sigma_i^2}.$$

The Birge chi-squared statistic measures the weighted sum of squared deviations from this mean:

$$\chi_B^2 = \sum_{i=1}^{n} w_i\, (x_i - \bar{x})^2.$$

If the estimates are mutually consistent, that is, if their spread is fully explained by their stated uncertainties, then χ_B^2 follows a chi-squared distribution with $\nu = n - 1$ degrees of freedom, with expected value $\mathbb{E}[\chi_B^2] = n - 1$. The Birge ratio is defined as:

$$R_B = \sqrt{\frac{\chi_B^2}{n-1}},$$

and has the following interpretation: (i) if $R_B \approx 1$, the estimates are mutually consistent and the spread is fully explained by the uncertainties, (ii) if $R_B \ll 1$, then the state uncertainties may be overestimated, and (iii) if $R_B \gg 1$, then the estimates are inconsistent and at least one uncertainty is under-estimated, or a systematic error is present.

In this work, a threshold of $R_B = 2.0$ is used to flag inconsistency. This is deliberately conservative — a threshold of $\sqrt{2}$ would correspond to twice the expected chi-squared, while $R_B = 2.0$ allows for moderate over-dispersion before triggering a warning.

5.3.1.1 Interpretation in the context of this work

A high Birge ratio between the supply scale, WIT-200, receipt scale, WIT-300, and flowmeter, AIT-250 is expected in some scenarios. The floor scales are cross-calibrated against the reference scale, WS-10, which itself is not independently traceable to a national standard. The flowmeter has no independent cross-calibration. When scale calibration corrections are applied, the corrected scale estimates may disagree with the flowmeter integral by more than the stated flowmeter uncertainty — not because the uncertainties are wrong, but because the flowmeter and the scales are measuring subtly different quantities (the flowmeter integrates instantaneous mass flow, which

includes the negative drain-phase backflow, while the scales measure the net change in tank contents). The Birge ratio serves as a diagnostic for this kind of systematic discrepancy.

5.3.2 Combining independent measurements

When n independent estimates $x_1, x_2, \ldots, x_n$ of the same quantity are available, the optimal linear unbiased estimator (under Gaussian assumptions) is the inverse-variance weighted mean:

$$\bar{x} = \frac{\sum_{i=1}^{n} w_i\, x_i}{\sum_{i=1}^{n} w_i}, \qquad w_i = \frac{1}{\sigma_i^2}.$$

The standard uncertainty of this combined estimate is:

$$\sigma_{\bar{x}} = \frac{1}{\sqrt{\sum_{i=1}^{n} w_i}}.$$

This is always smaller than the uncertainty of any individual estimate: $\sigma_{\bar{x}} < \min_i(\sigma_i)$. In the limit where one estimate is much more precise than the others ($\sigma_j \ll \sigma_i$ for $i \neq j$), the combined estimate approaches x_j and $\sigma_{\bar{x}} \to \sigma_j$.

The contribution of each estimate to the combination is proportional to its weight $w_i / \sum_j w_j$. In this work, the receipt scale WIT-300 typically has a smaller uncertainty than the supply scale WIT-200 at the operating loads of these experiments, because the proportional systematic uncertainty $u_{\text{sys}} = s \cdot m$ is smaller at lower loads. The flowmeter integral, with a relative uncertainty of 0.2 tends to dominate the combination when calibration corrections are applied to the scales.

5.3.2.1 Handling inconsistency

When $R_B > R_{\text{threshold}}$ for any set of measurements, it is a warning that we should pause and consider if this inconsistency is expected or if there is some uncertainty that is not being appropriately captured. In the software developed to support the uncertainty quantification, we provide two options of how to deal with measurements that yield high Birge ratios.

1. **Flag only**: Report the inconsistency and use the inverse-variance weighted combination as-is. The combined uncertainty $\sigma_{\bar{x}}$ may be under-estimated if the true spread of the estimates exceeds what the stated uncertainties predict. This option preserves the stated uncertainties and flags the inconsistency for investigation.

2. **Scale up (Birge ratio method (Bodnar and Clemens 2014))**: Inflate the combined uncertainty by the Birge ratio:

   $$\sigma_{\bar{x},\text{inflated}} = R_B \cdot \sigma_{\bar{x}},$$

   so that χ^2 of their weighted mean becomes equal to its expected value. This is equivalent to assuming that all stated uncertainties are underestimated by the same factor R_B and rescaling accordingly. It is a conservative approach that ensures the reported uncertainty is

consistent with the observed spread of the estimates, at the cost of potentially over-estimating the uncertainty when only one estimate is an outlier.

Both options are implemented in the pipeline and can be selected via a parameter. The choice between them depends on the scientific context: when the source of inconsistency is understood (e.g. known flowmeter offset), flagging only is appropriate; when the source is unknown, scaling up provides a more conservative and defensible reported uncertainty.

5.3.2.2 Uncertainty budget under combination

When estimates are combined using inverse-variance weighting, the contributions to the combined uncertainty from each input estimate's sources are scaled by $\left(w_i / \sum_j w_j\right)^2$. This means the dominant uncertainty source in the combination is determined by whichever estimate has the largest weight (smallest σ_i) multiplied by the fractional variance of its dominant source. The fully decomposed uncertainty budget is preserved through the combination, allowing identification of which physical source (scale calibration, flowmeter systematic, PLS model RMSEP, etc.) dominates the final uncertainty regardless of how many independent estimates are combined.

5.4 Chemometric modeling

5.4.1 Partial least squares regression

PLS regression is a latent variable method that simultaneously decomposes the predictor matrix X (here, absorbance or Raman intensity spectra) and the response matrix Y (here, analyte concentration) into a small number of latent components that maximize the covariance between X and Y.(de Jong 1993; Martens and Næs 1984) It is the standard chemometric tool for quantitative spectroscopic calibration when the number of predictors (wavelengths) greatly exceeds the number of calibration samples and when predictors are highly collinear; both of which are characteristic of UV-vis and Raman spectra.

5.4.1.1 Model structure

For a calibration set of n spectra $\boldsymbol{X} \in \mathbb{R}^{n \times p}$, where p is the number of wavelengths, and corresponding concentrations $\boldsymbol{y} \in \mathbb{R}^n$, PLS finds a decomposition:

$$\boldsymbol{X} = \boldsymbol{T}\boldsymbol{P}^\top + \boldsymbol{E}_X$$

$$\boldsymbol{y} = \boldsymbol{T}\boldsymbol{q}^\top + \boldsymbol{e}_y$$

where $\boldsymbol{T} \in \mathbb{R}^{n \times A}$ is the score matrix, $\boldsymbol{P} \in \mathbb{R}^{p \times A}$ are the X-loadings, $\boldsymbol{q} \in \mathbb{R}^A$ are the Y-loadings, and A is the number of retained latent components. The residual matrices $\boldsymbol{E}_X$ and $\boldsymbol{e}_y$ represent the variation in spectra and concentrations not explained by the A-component model. The number of components A is chosen by cross-validation to minimize prediction error without overfitting.

For a new spectrum $\boldsymbol{x}_{\text{new}}$ the predicted concentration is:

$$\hat{c} = \boldsymbol{x}_{\text{new}}\boldsymbol{b}_{\text{PLS}} + b_0$$

where $\boldsymbol{b}_{\mathrm{PLS}} \in \mathbb{R}^p$ is the vector of PLS regression coefficients and b_0 is the intercept. In this work, separate PLS models were calibrated for each analyte (Nd^{3+} via UV-Vis, NO_3^- via Raman) and for each physical sensor track (T01, T03, T04, T05), yielding eight models in total. All models share the same architecture but differ in their calibration data, regression coefficients, and performance statistics. More details of the model training and calibration can be found in Section 4.0.

5.4.1.2 Calibration and validation statistics

Three figures of merit characterize PLS model performance, all reported in native concentration units (mM for Nd^{3+}, M for NO_3^-):

1. **Root Mean Squared Error of Calibration (RMSEC)** measures the in-sample fit of the model to the calibration data:

$$\mathrm{RMSEC} = \sqrt{\frac{1}{n}\sum_{i=1}^{n}(c_i - \hat{c}_i)^2}$$

   A low RMSEC relative to RMSECV indicates that the model fits the calibration data well without overfitting. For the UV-vis models, RMSEC = 0.405 mM across all tracks, and for the Raman models, RMSEC = 0.0548 M.

2. **Root Mean Squared Error of Cross-Validation (RMSECV)** is estimated by leave-one-out or k-fold cross-validation and reflects the model's ability to predict samples excluded from calibration:

$$\mathrm{RMSECV} = \sqrt{\frac{1}{n}\sum_{i=1}^{n}\left(c_i - \hat{c}_{i,-i}\right)^2}$$

   where $\hat{c}_{i,-i}$ is the prediction for sample i from a model trained without it. For the UV-vis models, RMSECV = 0.447 mM and for Raman models RMSECV = 0.0688 M; the small difference from RMSEC indicates the models are not overfit.

3. **Root Mean Squared Error of Prediction (RMSEP)** is estimated from an independent validation set held out during calibration and represents the best available estimate of model performance on future samples:

$$\mathrm{RMSEP} = \sqrt{\frac{1}{m}\sum_{j=1}^{m}\left(c_j - \hat{c}_j\right)^2}$$

For the UV-vis models, RMSEP = 0.4778 mM; for the Raman models, RMSEP = 0.03425 M. RMSEP is the primary uncertainty term attributed to model prediction error in the uncertainty budget of this work, as it characterizes performance on independent samples most representative of the deployment condition.

The corresponding coefficients of determination R_C^2, R_{CV}^2, and R_P^2 are also available in the data and confirm high predictive power ($R_C^2 = 0.9986$, $R_{CV}^2 = 0.9982$, $R_P^2 = 0.9982$ for UV-Vis and $R_C^2 = 0.9974$, $R_{CV}^2 = 0.9959$, $R_P^2 = 0.9987$ for Raman). For more details on the PLS models and their training, please refer to Section 4.0.

5.4.1.3 Applicability domain indicators

Two complementary statistics characterize whether a new spectrum lies within the region of the calibration space where the model can be expected to perform reliably:

1. **Hotelling T^2** measures the distance of the new sample from the centroid of the calibration set in the latent variable (score) space:

$$T^2 = \sum_{a=1}^{A} \frac{t_a^2}{s_a^2}$$

where t_a is the score on component a and s_a^2 is the variance of calibration scores on that component. Under the assumption that calibration scores are normally distributed, T^2 follows an F-distribution with critical value:

$$T^2_{\text{crit}} = \frac{A(n^2-1)}{n(n-A)} F_{\alpha,A,n-A}$$

A sample with $T^2 > T^2_{\text{crit}}$ is at the edge of or outside the calibration space. The prediction of such a value involves extrapolation and should be treated with additional caution.

2. **Q-residual** (also called the squared prediction error, SPE) measures how well the retained A components reconstruct the observed spectrum:

$$Q = \|\boldsymbol{x} - \hat{\boldsymbol{x}}\| = \|\boldsymbol{x} - \boldsymbol{t}\boldsymbol{P}^{\top}\|^2$$

A large Q means the spectrum contains structure that the model cannot represent. It could mean that the sample is from outside the calibration distribution, the sensor may be malfunctioning, or in the context of inline pipe measurements, the pipe may not be fully filled with solution.

In this work, T^2 and Q-residual thresholds are used as optional components of the pipe-full validity mask. Spectra exceeding either threshold are flagged as potentially invalid and excluded from the concentration time series used in the mass balance integration. Separate thresholds are required for

UV-vis and Raman sensors because the two modalities operate at fundamentally different spectral resolutions and signal levels, yielding T^2 and Q-residual values on very different numerical scales. For example, in Trial 3, the mean T^2 for valid Raman T05 spectra was 545.8 compared to 1.4 for UV-vis T05 spectra.

5.4.1.4 Total spectroscopic uncertainty

The total uncertainty of a single PLS concentration prediction c combines two independent components:

1. **Model prediction error (RMSEP)**: Represents the irreducible error of the calibrated model, including calibration sample heterogeneity, model inadequacy, and reference measurement error. It is treated as a constant for a given model and track.

2. **Spectral noise propagated through the model ($\sigma_{\mathbf{MC}}$)**: Represents the contribution of instrument noise on the observed spectrum to the concentration prediction uncertainty. It is estimated by Monte Carlo perturbation: N perturbed spectra $\boldsymbol{x}_k = \boldsymbol{x} + \boldsymbol{\varepsilon}_k$ are generated by adding noise drawn from the estimated per-wavelength noise distribution, each is passed through the PLS model, and the standard deviation of the resulting predictions characterizes this contribution.

Since RMSEP and σ_{MC} are independent, they are combined in quadrature to give the total spectroscopic uncertainty for a single spectrum:

$$u_{\mathrm{PLS}}(\hat{c}) = \sqrt{\mathrm{RMSEP}^2 + \sigma_{\mathrm{MC}}^2}.$$

For example, in Trial 3, representative values from the experimental data of UV-Vis T05 track give $RMSEP = 0.478$ mM and $\sigma_{\mathrm{MC}} \approx 0.009 - 0.014$ mM, so that $u_{\mathrm{PLS}} \approx$ RMSEP. This means the model prediction error dominates by two orders of magnitude in variance. For the Raman T01 and T03 inline pipe sensors in the same experiment, σ_{MC} can be substantially larger when the pipe is not fully filled with solution, reaching values of 1.5 M or more compared to $RMSEP = 0.034$ M. This large σ_{MC} exceeds RMSEP by more than an order of magnitude and serves as a diagnostic criterion in the pipe-full validity mask described in Section 5.5.1.

5.5 Strategies for invalid measurements

The sensors used to measure system properties require certain physical conditions to be met for proper usage. For example, the accuracy of the Coriolis flowmeter is significantly degraded when the level of solution in the transfer pipe is low. Similarly, the inline spectroscopic sensors may produce invalid readings when the flow cells are not full of solution or when the solution in the flow cells is heavily aerated. As a result, the concentration predicted by the chemometric model may be highly inaccurate or even infeasible, such as producing a negative predicted concentration for an analyte.

In situations like these, the uncertainty of the individual measurements may dominate the uncertainty of the entire transfer if they are incorporated into the mass transfer equations. Many

measurements in the system are made redundantly, using independent observations. This makes it possible to reject some invalid measurements in favor of valid measurements made with other sensors, to combine measurements from multiple sensors, or to interpolate between measurements that have been determined to be valid. In each case these imputation strategies can reduce the combined uncertainty without compromising the integrity of the experiment.

For example, at different times during normal operation of the power fluidics system, solution may be flowing forward through the transfer pipe from Tank 1 to Tank 2, flowing backward into Tank 1, or not flowing at all. Since the inline Raman and UV-vis sensors are calibrated using full flow cells, they may provide inaccurate or invalid spectra when the transfer pipe and flow cells are not full. When invalid spectra are used as input to the chemometric models, the predicted concentration may also be inaccurate and have high uncertainty. One might hope that because very little mass is transferred during the times when the flow cells are not full, the high uncertainty associated with the invalid spectra might be mitigated by the relatively small amount of solution that is transferred. However, concentration uncertainty can grow exponentially for spectra that are not within the calibration range of the chemometric models and may dominate the final combined uncertainty.

One way to reduce the uncertainty of these concentration estimates is to forward fill the invalid measurements, replacing them with the last valid concentration estimate. This strategy assumes that concentrations change smoothly with time, so measurements taken at consecutive time steps will have similar concentrations, and that valid concentration estimates have lower uncertainty than invalid measurements. However, if a large number of consecutive measurements are invalid, the difference between the true concentration of the most recent valid measurement and the true concentration of the current invalid measurement may also be large. Thus, the first invalid measurement to be replaced has a lower uncertainty associated with imputation than the last invalid measurement to be replaced.

To account for this difference, we include a ‘concentration drift’ term in our uncertainty register that grows linearly with the number of consecutive measurements that have been imputed. Hypothetically, if all inline concentration estimates were determined to be invalid, this forward-filling strategy would be equivalent to using the lab standard as a constant estimated concentration, and the uncertainty associated with concentration drift may dominate the final combined uncertainty. In practice however, the number of measurements to be imputed is controlled by how we detect and mask invalid measurements.

It is not enough to reject, or mask, measurements simply because they are associated with a high uncertainty. Uncertainty is inherent in the system and ignoring valid measurements may underestimate the true uncertainty in the system and lead to false confidence in the results. Instead, we exploit indirect signals of the physical system or the underlying model assumptions to determine whether a measurement is valid or not.

One masking strategy is to use the phases of the power fluidics system to determine potentially invalid measurements. When the power fluidics pump is in the charge or drain phases, solution is not being pumped forward from Tank 1 to Tank 2. A small amount of solution may be backflowing into Tank 1 due to the angle of the transfer pipe, but in general the transfer pipe and the flow cells will not be full, and the spectra observed by the inline Raman and UV-vis sensors may not be valid.

When negative concentrations (computed from invalid spectra) are multiplied by negative mass transfer (from backflowing solution), the mass flow will be inaccurately measured as positive at a time when no solution is flowing into Tank 2. By masking the concentrations observed during the charge and drain phases, we can avoid these inaccuracies and their high uncertainties. Forward filling the last valid concentration to these timesteps leads to a negative measured mass transfer, that agrees with the physical state of the system where solution is flowing backwards into Tank 1. In contrast, during the drive phase of the power fluidics system, there may also be times when the transfer pipe and flow cells are not full, due to the nature of the flow profile, but even if a spectrum observed during the drive phase has high estimated uncertainty, it is unreasonable to reject it without additional information because it may simply be an uncertain measurement generated by a valid reading.

There are numerous signals that can be leveraged to identify invalid measurements and there are multiple ways of imputing the missing data. Additionally, when the measurements from different sensors are not jointly observed, observations can be resampled to a common grid. The details of these strategies are included in the following subsections.

5.5.1 Masking strategies

The inline flowmeter and spectroscopy sensors may produce invalid predictions when the transfer pipe is not fully filled.

Table 6 describes eight criteria that are available to mask concentration measurements. Each of these masks can be applied separately, or multiple masks can be used in combination.

Table 6. Masking strategies

Strategy	Description
No mask	no measurements are masked and all are included in the final calculations
Power fluidics phase mask	measurements during the charge and drain phases are masked and imputed
Q-residual threshold mask	measurements masked if the Q-residual exceeds a user-defined threshold
T^2 threshold mask	measurements masked if the T^2 statistic exceeds a user-defined threshold
Monte Carlo Std. mask	measurements are masked when the standard deviation of the Monte Carlo concentration predictions exceed a user-defined threshold
Concentration bound mask	measurements are masked when the estimated concentration is outside of a user-defined range (e.g., negative concentrations are masked or concentrations above 100% are masked)
Concentration spike mask	measurements are masked when the concentration changes by more than a user-defined amount between consecutive observations
Flow rate mask	measurements are masked when the flowrate drops below a user-defined threshold

5.5.2 Imputation strategies

When an invalid spectrum is masked, the corresponding time window has no concentration estimate. Three strategies are for replacing masked values are described in Table 7.

Table 7. Imputation strategies

Strategy	Description
No imputation	the time window contributes nothing to the integral, the mass transfer is estimated to be zero
Forward fill imputation	the most recent valid concentration is carried forward
Immersion probe imputation	concentrations for inline sensors are imputed from T05 immersion values when inline sensors are invalid

5.5.3 Resampling strategy

In an idealized system, sensors measurements would be made at the same time and would measure properties of the same sample of solution. However, this is not feasible in practice (or even theoretically possible for some measurements) because, e.g., the sensors cannot be collocated, and different sensor-types have different temporal resolutions. In particular, the floor scales and flowmeter operate at 10 Hz while the Raman and UV-vis sensors operate at ~0.5 Hz. To account for these temporal differences the observations are resampled to a common grid. The resampling strategies are described in Table 8.

Table 8. Resampling strategies

Strategy	Description
Spectroscopy-rate integration	Concentrations evaluated only at valid spectrum timestamps
Forward-fill integration	Concentrations carried forward to all 10 Hz timestamps
Linearly interpolated integration	Concentrations linearly interpolated to all 10 Hz timestamps

5.6 Uncertain quantities

This section provides a comprehensive list of the uncertainty sources included in the uncertainty budget. In Table 9 we see the sources associated with the floor scales. The main components are the systematic uncertainty, which is a linear function of the measured load, and the random uncertainty, which can be reduced by averaging scale measurements over small time windows.

Table 9. Scale uncertainty sources.

Uncertainty source	Description
supply_scale_start_systematic	Proportional bias in the WIT-200 scale reading at the start of the experiment. Scales with load: $u = s * m$. Not reduced by averaging.
supply_scale_start_random	Random noise on the WIT-200 supply scale at the start window. Reduced by averaging: $u = c/\sqrt{N}$.
supply_scale_end_systematic	Same as start systematic but at the end of the experiment
supply_scale_end_random	Same as start random but at the end of the experiment
receipt_scale_start_systematic	Proportional bias in the WIT-300 receipt scale at the start
receipt_scale_start_random	Random noise on WIT-300 at the start window
receipt_scale_end_systematic	Proportional bias in WIT-300 at the end
receipt_scale_end_random	Random noise on WIT-300 at the end window
supply_scale_calibration_fit	Uncertainty of the PCHIP spline correction for WIT-200, estimated by leave-one-out cross-validation (LOO-RMSE = 0.463 kg)
receipt_scale_calibration_fit	Uncertainty of the PCHIP spline correction for WIT-300 (LOO-RMSE = 0.418 kg)

In Table 10 we see the uncertainty sources associated with the flowmeter. These systematic and random components are applied to the total mass transferred and to each analyte individually.

Table 10. Flowmeter uncertainty sources.

Uncertainty source	Description
flowmeter_systematic	Calibration bias of the AIT-250 Coriolis flowmeter — a constant fractional error (0.2% of reading) that is fully correlated across all time steps and does not average down over the experiment
flowmeter_random	Independent reading-to-reading noise on the flowmeter. Partially averages out over many integration steps but is negligible compared to the systematic term for long experiments
{analyte}_flowmeter_systematic	Flowmeter systematic uncertainty propagated into the analyte mass estimate — scales with the total analyte mass transferred
{analyte}_flowmeter_random	Flowmeter random uncertainty propagated into the analyte mass

Table 11 describes the uncertainty sources that are connected to the chemometric PLS models. As we see in the summary in Table 16, the RMSEP of the PLS models is one of the dominant sources of uncertainty. The magnitude of this uncertainty can be reduced by masking concentration predictions with low confidence or infeasible values and interpolating from previous measurements, however this solution incurs other forms of uncertainty. Additionally, the uncertainty contributions for the Monte Carlo simulations perturbations can be significant when the transfer pipe is not full or when the observed sample has very low predicted concentration of for the relevant analyte.

Table 11. PLS spectroscopy uncertainty sources.

Uncertainty source	Description
uv_vis_T01_rmsep	Root mean squared error of prediction for the UV-vis PLS model on track T01 (inline pipe sensor). Represents irreducible model error (0.477845 mmol/L)
uv_vis_T03_rmsep	Same as T01 RMSEP but for the T03 inline pipe sensor
uv_vis_T05_rmsep	RMSEP for the UV-vis T05 supply tank immersion probe model
raman_T01_rmsep	RMSEP for the Raman PLS model on track T01 (0.034252 mol/L)
raman_T03_rmsep	RMSEP for the Raman T03 inline pipe sensor model
raman_T05_rmsep	RMSEP for the Raman T05 supply tank immersion probe model
uv_vis_T01_mc_std	Standard deviation of UV-vis T01 predictions from Monte Carlo spectral perturbation — represents instrument noise propagated through the PLS model
uv_vis_T03_mc_std	Same as T01 MC std but for T03
uv_vis_T05_mc_std	MC perturbation std for T05 UV-vis. Typically much smaller than RMSEP for valid tank probe spectra
raman_T01_mc_std	Raman T01 MC perturbation std. Can be large when the pipe is not full, serving as a pipe-full diagnostic
raman_T03_mc_std	Same as T01 Raman MC std but for T03
raman_T05_mc_std	Raman T05 MC std. Typically small for valid immersion probe spectra

In Table 12 we describe the uncertainty sources related to ‘ground truth’ values of the solutions. If the true concentration of each analyte does not match the measured value, uncertainty will propagate through the system. Concentrations were determined in using a lab standard addition prior to experimentation to correct for such biases. More details can be found in Section 5.2.

Table 12. Lab measurement uncertainty sources.

Uncertainty source	Description
lab_standard_addition	Uncertainty of the initial analyte concentration measured by standard addition in the laboratory. Applies directly to the lab-fallback concentration estimate
lab_anchor_lab_uncertainty	The lab standard addition uncertainty propagated into the lab anchor correction — represents how well we know the true initial concentration
lab_anchor_pls_variability	Variability of the PLS T05 predictions during the pre-transfer window used to compute the anchor correction — represents uncertainty in the PLS mean used as the bias reference

Table 13 contains the uncertainty source related to concentration drift. This source characterizes the uncertainty that grows with time when concentration measurements are not recorded due to a system error or invalid/infeasible measurements are masked. The drift rate is estimated from immersion probe readings prior to a tank transfer. This can become a dominant source of uncertainty if too many observations are masked.

Table 13. Concentration drift uncertainty sources.

Uncertainty source	Description
{analyte}_concentration_drift	Uncertainty introduced by forward-filling the last valid concentration across a gap of duration . Grows as $\sigma_{\text{drift}} \cdot \Delta t$ where σ_{drift} is the empirical drift rate (0.247 mmol/L/s for Nd^{3+}, and 0.271 mol/L/s for NO3-).

Table 14 includes the uncertainty sources related to density. They are recorded independently for the density sensors in the supply tank and in the transfer pipe, respectively.

Table 14. Density uncertainty sources.

Uncertainty source	Description
{label}_density	Uncertainty of the fluid density measurement from DIT-200 (supply tank) or DIT-250 (pipe). Default relative uncertainty 0.1%

Table 15 includes uncertainties that are related to combined measurements and the reconciliation of repeated observations. These terms come into play when two sensors measure different values for the same measurand. Uncertainty can be reduced by using a weighted some of the predicted values, as was described in Section 5.3.2.

Table 15. Combination and reconciliation uncertainty sources.

Uncertainty source	Description
{analyte}_flow_weighted_mean_conc	Uncertainty of the flow-weighted mean concentration used in the scale-weighted analyte mass estimate. Represents variability of PLS predictions across the experiment weighted by flow
{analyte}_pls_combined	Aggregated PLS uncertainty when multiple spectra are combined into a single mean estimate

The uncertainty register ends with a summary of the uncertainty sources in Table 16. This table groups the sources into 7 categories and describes the magnitude of their typical contributions in the final uncertainty budget. The dominance descriptions represent the typical behavior seen in the trials but are not prescriptive. Any category could become dominant, depending on the experimental parameters.

Table 16. Uncertainty sources grouped by category.

Category	Sources included	Typical dominance
Scale (systematic)	*_systematic	Dominant at high tank loads (>5000 kg)
Scale (random)	*_random	Small — reduced by averaging over 10s window
Scale calibration	*_calibration_fit	Small — LOO-RMSE ≈ 0.4–0.5 kg
Flowmeter	flowmeter_*	Dominant for flowmeter-only integration mode
PLS model (RMSEP)	*_rmsep	Dominant for spectroscopy-based estimates
PLS spectral noise	*_mc_std	Small for valid spectra; large for invalid pipe spectra
Concentration drift	*_concentration_drift	Grows with gap duration; can be significant for windows longer than 5–10s
Lab measurement	lab_standard_addition, lab_anchor_*	Small — typically < 1% relative
Density	*_density	Small — typically < 0.1% relative

6.0 Materials Accountancy and Uncertainty Analysis Results

The consolidated test matrix shown in Table 2 describes the parameters for each of the experimental trials and repetitions. The equations described in Section 4.0 provides the specific analysis framework under which each trial is evaluated. In this section, we provided a detailed analysis of the trials and evaluate their success against the target of ±1% uncertainty in the resulting material accountancy.

Several examples of successfully meeting or exceeding the ±1% uncertainty goal are presented, highlighting the differences between results using different data streams and processing assumptions/approaches.

6.1 Overview of the mass transfer uncertainty analysis for Nd^{3+}

Table 17 provides an overview of the combined standard uncertainty (kg) and the relative combined standard uncertainty (%) for the Nd^{3+} mass transfer trials. The mass transfer was measured using Coriolis flowmeter-integrated mass measurements. The concentration predictions were computed from the spectra measured by Tracks T01 and T03 and the predicted concentrations were combined using inverse-variance weighting. The resulting combined concentration predictions were resampled using the forward fill integration strategy. Invalid concentrations were masked using a combination of the power fluidics phase mask, the Q-residual threshold mask, the concentration bound mask, and the concentration spike mask.

Table 17. Nd^{3+} estimated transferred mass and relative uncertainty.

Trial	Rep.	Solution	Mass (kg)	$u_c(m)$ (kg)	$u_r(m)$ (%)	Success	Dominant category
1	1	Surrogate	6.7537	0.0390	0.58	TRUE	PLS model (RMSEP)
1	2	Surrogate	6.5325	0.0401	0.61	TRUE	PLS model (RMSEP)
1	3	Surrogate	6.3295	0.0327	0.52	TRUE	PLS model (RMSEP)
2	1	Surrogate	6.6673	0.0258	0.39	TRUE	PLS model (RMSEP)
3	1	Surrogate	6.4511	0.0342	0.53	TRUE	PLS model (RMSEP)
4	1	Surrogate	2.1257	0.0174	0.82	TRUE	PLS model (RMSEP)
4	2	Surrogate	2.0248	0.0276	1.36	FALSE	PLS model (RMSEP)
4	3	Surrogate	2.0104	0.0114	0.57	TRUE	PLS model (RMSEP)
5	1	Surrogate	2.1345	0.0209	0.98	TRUE	PLS model (RMSEP)
5	2	Surrogate	1.9750	0.0217	1.10	FALSE	PLS model (RMSEP)
5	3	Surrogate	1.9965	0.0191	0.96	TRUE	PLS model (RMSEP)
6	1	Surrogate	2.6537	0.0200	0.75	TRUE	PLS model (RMSEP)
7	1	Dilution 1	2.7379	0.0158	0.58	TRUE	PLS model (RMSEP)
7	2	Dilution 1	3.9415	0.0203	0.51	TRUE	PLS model (RMSEP)
7	3	Dilution 1	5.3577	0.0253	0.47	TRUE	PLS model (RMSEP)
8	1	Dilution 1	6.1160	0.0508	0.83	TRUE	PLS model (RMSEP)
8	2	Dilution 1	5.1603	0.0248	0.48	TRUE	PLS model (RMSEP)
9	1	Dilution 1	0.7509	0.0076	1.02	FALSE	PLS model (RMSEP)
9	2	Dilution 1	1.1495	0.2046	17.80	FALSE	Lab measurement
9	3	Dilution 2	1.7956	0.0102	0.57	TRUE	PLS model (RMSEP)

10	1	Dilution 1	0.6816	0.3324	48.77	FALSE	Lab measurement
10	2	Dilution 1	0.1712	0.0009	0.55	TRUE	PLS model (RMSEP)
10	3	Dilution 2	1.8471	0.0152	0.82	TRUE	PLS model (RMSEP)
10	4	Dilution 2	1.8674	0.0141	0.75	TRUE	PLS model (RMSEP)
11	1	Dilution 2	3.9992	0.0244	0.61	TRUE	PLS model (RMSEP)
11	2	Dilution 2	1.6739	0.0082	0.49	TRUE	PLS model (RMSEP)
11	3	Dilution 2	4.0056	0.0115	0.29	TRUE	PLS model (RMSEP)
12	1	Dilution 2	3.7459	0.0217	0.58	TRUE	PLS model (RMSEP)
12	2	Dilution 2	4.2127	0.0121	0.29	TRUE	PLS model (RMSEP)
13	1	Dilution 2	1.6328	0.0112	0.69	TRUE	PLS model (RMSEP)
13	2	Dilution 2	1.5637	0.0106	0.68	TRUE	PLS model (RMSEP)
13	3	Dilution 2	1.6160	0.0120	0.74	TRUE	PLS model (RMSEP)
14	1	Dilution 2	1.6191	0.0137	0.85	TRUE	PLS model (RMSEP)
14	2	Dilution 2	1.5695	0.0113	0.72	TRUE	PLS model (RMSEP)
14	3	Dilution 2	0.6717	0.0067	1.00	TRUE	PLS model (RMSEP)
15	1	Dilution 2	1.5700	0.0077	0.49	TRUE	PLS model (RMSEP)
15	2	Dilution 2	0.8655	0.0064	0.74	TRUE	PLS model (RMSEP)
16	1	Dilution 2	1.2798	0.0089	0.70	TRUE	PLS model (RMSEP)
16	2	Dilution 2	1.3503	0.0082	0.61	TRUE	PLS model (RMSEP)

The column labeled ‘Success’ indicates trials that pass the ≤ 1% relative uncertainty target. The success criterion was met for 34/39 (87.2%) of the trials/replications (labeled in green). The most common dominant source of uncertainty is the PLS model (RMSEP), which represents error in the chemometric model that cannot be reduced by repeated measurements.

Figure 31 shows the Nd^{3+} cumulative mass transferred (top) and relative standard uncertainty (bottom) for Trial 1 – Repetition 1 where the uncertainty target is met (0.58%). Table 18 show the complete uncertainty budget for the same Trial. We can see that 99.65% of the total uncertainty comes from irreducible RMSEP of the Track T01 concentration estimates.

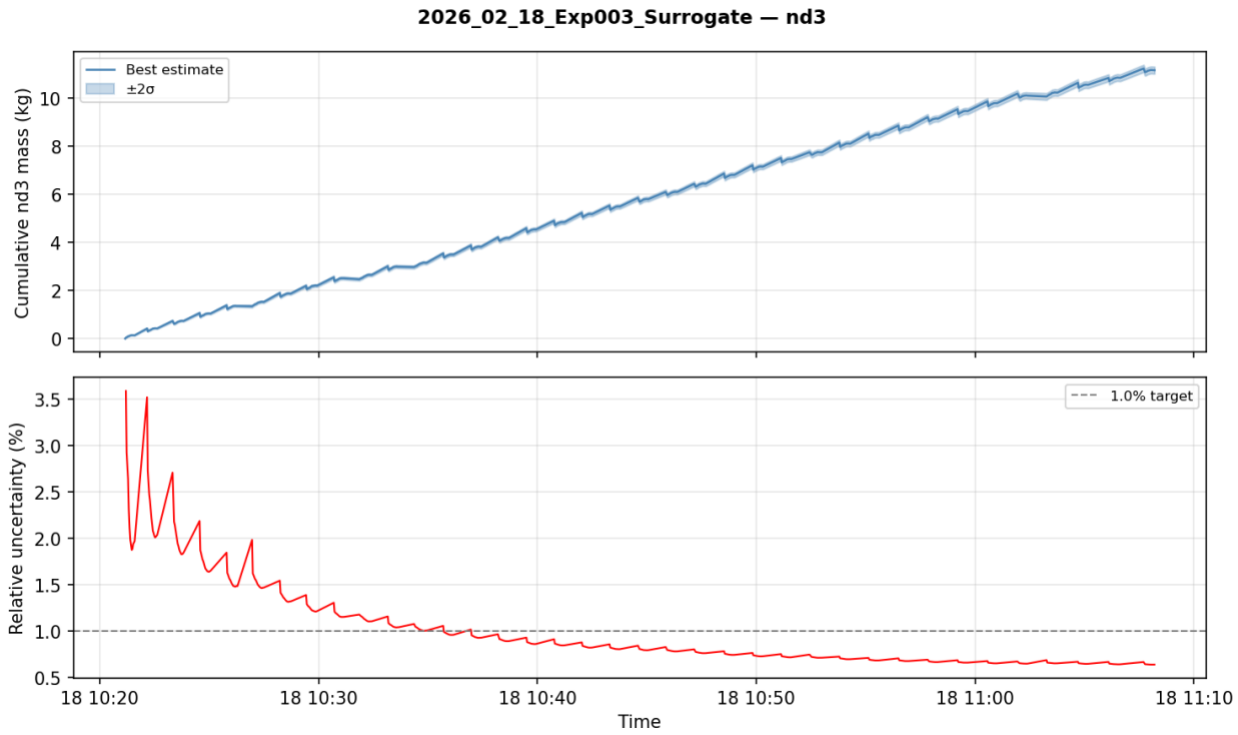


Figure 31. Trial 1 – Repetition 1 Nd^{3+} cumulative mass transferred (top) and relative standard uncertainty (bottom).

Table 18. Trial 1 – Repetition 1 uncertainty budget for Nd^{3+} mass transfer.

Source	Category	Variance	Std.	% of total
uv_vis_T01_rmsep	PLS model (RMSEP)	0.002	0.04	99.65
uv_vis_T03_rmsep	PLS model (RMSEP)	4.1e-06	0.002	0.27
uv_vis_T01_mc_std	PLS spectral noise	1.1e-06	0.001	0.076
uv_vis_T03_mc_std	PLS spectral noise	2.1e-09	4.5e-05	0.001
nd3_flowmeter_systematic	Flowmeter	4.1e-10	2.0e-05	2.7e-05
nd3_flowmeter_random	Flowmeter	4.6e-14	2.1e-07	3.0-09
nd3_concentration_drift	Concentration drift	8.8e-15	9.4e-08	5.8e-10

There are five trials/replications for which the success criterion is not met for the Nd^{3+} analyte. Of these five missed targets, three trials (labeled in blue) have a relative standard uncertainty is between 1% and 2%. Figure 32 shows the cumulative mass transferred (top) and relative standard uncertainty (bottom) for Trial 4 – Repetition 2 and Table 19 provides the uncertainty budget. Contrary to the pattern seen in Figure 31, in this trial there is an initial period of a few seconds here invalid measurements are being masked and imputed. This can be seen in the increasing mass and uncertainty in Figure 32 (top) on the left-hand side. After this initial rapid increase, the uncertainty decreases consistently throughout the transfer.

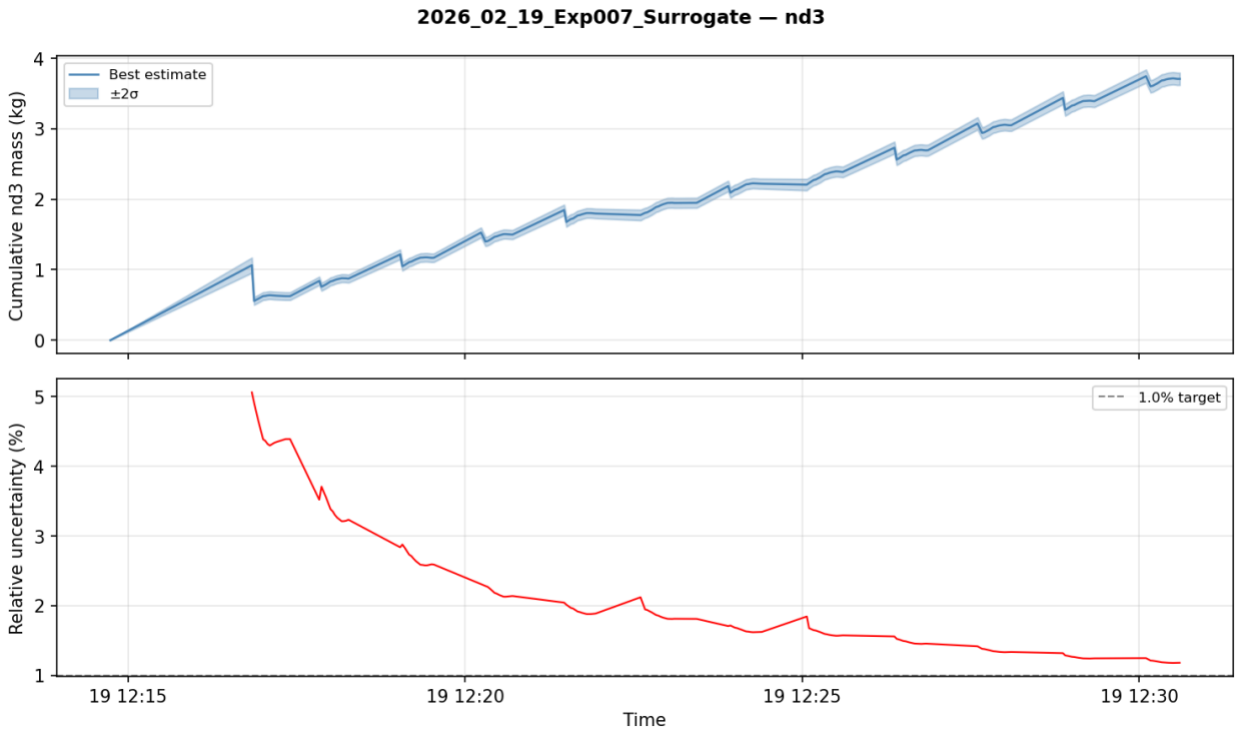


Figure 32. Trial 4 – Repetition 2 Nd^{3+} cumulative mass transferred (top) and relative standard uncertainty (bottom).

Table 19. Trial 4 – Repetition 2 uncertainty budget for Nd^{3+} mass transfer.

Source	Category	Var	Std.	% of total
uv_vis_T01_rmsep	PLS model (RMSEP)	0.0007	0.026	92.84
uv_vis_T03_rmsep	PLS model (RMSEP)	5.4e-05	0.0073	7.08
uv_vis_T01_mc_std	PLS spectral noise	5.4e-07	0.00073	0.07
uv_vis_T03_mc_std	PLS spectral noise	2.8e-08	0.00016	0.003
nd3_flowmeter_systematic	Flowmeter	5.6e-11	7.4e-06	7.3e-06
nd3_concentration_drift	Concentration drift	3.0e-14	1.7e-07	3.9e-09
nd3_flowmeter_random	Flowmeter	2.1e-14	1.4e-07	2.8e-09

The remaining two trials (labeled in red) have significantly higher relative uncertainty (48.77% and 17.80%) and require further investigation. Rather than denoting a failure of the system, the high uncertainty in Trial 10 – Replication 1 and Trial 9 – Replication 2 represents the power of the uncertainty analysis tools. Both of these trials indicate that the Lab measurement category is the dominant form of uncertainty. Further inspection of the trials reveals that all concentration measurements were masked in these two trials, leading to a high level of uncertainty.

6.2 Overview of the mass transfer uncertainty analysis for NO_3^-

Table 20 provides an overview of the combined standard uncertainty (kg) and the relative combined standard uncertainty (%) for the NO_3^- mass transfer trials. The mass transfer was measured using Coriolis flowmeter-integrated mass measurements. The concentration predictions were computed from the spectra measured by Tracks T01 and T03 and the predicted concentrations were combined using inverse-variance weighting. The resulting combined concentration predictions were resampled using the forward fill integration strategy. Invalid concentrations were masked using a combination of the power fluidics phase mask, the Q-residual threshold mask, the concentration bound mask, and the concentration spike mask.

Table 20. NO_3^- estimated transferred mass and relative uncertainty.

Trial	Rep.	Solution	Mass (kg)	$u_c(m)$ (kg)	$u_r(m)$ (%)	Success	Dominant category
1	1	Surrogate	1024.7245	14.4036	1.41	FALSE	Concentration drift
1	2	Surrogate	1040.2300	14.8101	1.42	FALSE	Concentration drift
1	3	Surrogate	1031.7570	16.3134	1.58	FALSE	Concentration drift
2	1	Surrogate	1036.0436	10.2275	0.99	TRUE	Concentration drift
3	1	Surrogate	1023.7193	15.0106	1.47	FALSE	Concentration drift
4	1	Surrogate	328.5220	7.2858	2.22	FALSE	Concentration drift
4	2	Surrogate	330.1017	5.4196	1.64	FALSE	PLS spectral noise
4	3	Surrogate	337.7208	7.1882	2.13	FALSE	PLS spectral noise
5	1	Surrogate	352.4493	9.7396	2.76	FALSE	Concentration drift
5	2	Surrogate	335.6920	10.4979	3.13	FALSE	Concentration drift
5	3	Surrogate	332.3107	9.9362	2.99	FALSE	Concentration drift
6	1	Surrogate	430.4113	5.4575	1.27	FALSE	PLS spectral noise
7	1	Dilution 1	407.9795	5.9381	1.46	FALSE	Concentration drift
7	2	Dilution 1	577.5044	5.9364	1.03	FALSE	Concentration drift
7	3	Dilution 1	811.5576	8.5304	1.05	FALSE	Concentration drift
8	1	Dilution 1	796.4409	4.4722	0.56	TRUE	PLS spectral noise
8	2	Dilution 1	799.4412	7.8731	0.98	TRUE	Concentration drift
9	1	Dilution 1	109.6411	1.2659	1.15	FALSE	PLS spectral noise
9	2	Dilution 1	269.6531	2.8564	1.06	FALSE	Concentration drift
9	3	Dilution 2	272.7721	1.4275	0.52	TRUE	PLS spectral noise
10	1	Dilution 1	272.9228	8.7642	3.21	FALSE	Concentration drift
10	2	Dilution 1	4.1074	0.3058	7.45	FALSE	Concentration drift
10	3	Dilution 2	276.2303	5.9243	2.14	FALSE	Concentration drift
10	4	Dilution 2	276.1540	4.7404	1.72	FALSE	PLS spectral noise
11	1	Dilution 2	583.0001	5.8521	1.00	FALSE	PLS spectral noise
11	2	Dilution 2	250.9185	2.2570	0.90	TRUE	PLS spectral noise
11	3	Dilution 2	647.1405	5.9589	0.92	TRUE	PLS spectral noise
12	1	Dilution 2	642.7951	8.5580	1.33	FALSE	Concentration drift
12	2	Dilution 2	642.5340	5.3583	0.83	TRUE	Concentration drift
13	1	Dilution 2	217.8228	4.1472	1.90	FALSE	Concentration drift

13	2	Dilution 2	218.2789	2.8494	1.31	FALSE	PLS spectral noise
13	3	Dilution 2	218.3558	2.1517	0.99	TRUE	PLS spectral noise
14	1	Dilution 2	221.6436	6.4188	2.90	FALSE	Concentration drift
14	2	Dilution 2	223.1559	5.3772	2.41	FALSE	Concentration drift
14	3	Dilution 2	96.6262	4.6346	4.80	FALSE	Concentration drift
15	1	Dilution 2	215.7663	2.4846	1.15	FALSE	PLS spectral noise
15	2	Dilution 2	121.7473	2.6764	2.20	FALSE	PLS spectral noise
16	1	Dilution 2	179.8455	3.1387	1.75	FALSE	PLS spectral noise
16	2	Dilution 2	201.8778	3.9598	1.96	FALSE	Concentration drift

The results for the NO_3^- analyte show less trials that overtly meet the success criterion. Again, the column labeled 'Success' indicates trials that pass the $\leq 1\%$ relative uncertainty target. The success criterion was met for 8/39 (20.5%) of the trials/replications. For the NO_3^- mass transfers, the two most common dominant sources of uncertainty are concentration drift and PLS spectral noise. These dominant forms of uncertainty suggest that invalid spectra may not have been appropriately masked in the cases where the PLS spectral noise dominates, and too many valid spectra may have been masked in scenarios where the concentration drift uncertainty dominates. Another possibility is that the concentration drift rate used for NO_3^- has been estimated too high.

There are twenty-one trials/replications for which the success criterion is not met for the NO_3^- analyte. Of these missed targets, 19/39 (48.7%) of trials (labeled in blue) have a relative standard uncertainty that is between 1% and 2%. The remaining 12/39 (30.8%) of trials (labeled in red) have higher relative uncertainty (between 1.01% and 7.45).

In both of the trials with the highest uncertainty, the mass of sodium nitrate that was measured to have been transferred is significantly less than the estimated mass transferred for the other replications of the same trials. In Trial 10 – Replication 2, the relative uncertainty is estimated to be 7.45% and only 4.1074 kg of NO_3^- was estimated to have been transferred vs. 272.9228 kg and 276.2303 kg for Replications 1 and 3, respectively. Similarly, in Trial 14 – Replication 3, the estimated relative uncertainty is 4.80% and only 96.6262 kg of NO_3^- was estimated to have been transferred vs. 221.6436 kg and 223.1559 kg for Replications 1 and 2, respectively. If the true mass transferred in each of these cases is similar to the other replications, the relative uncertainty is significantly underestimated. However, in Table 21 we will see that each of these trials does indeed have a smaller total mass transfer. Upon further inspection of the uncertainty budget, we can see the real culprit is that all concentration measurements were masked in these two trials, leading to a high uncertainty.

6.3 Overview of the total mass transfer uncertainty analysis

Table 21 provides an overview of the combined standard uncertainty (kg) and the relative combined standard uncertainty (%) for total solution mass transfer trials. The mass transfer was measured using Coriolis flowmeter-integrated mass measurements. No concentration predictions were computed because the total mass transfer was measured.

We can see from this Table 21 that when the Coriolis flowmeter is used for incremental mass measurements of the entire solution, the only dominant form of uncertainty is the systematic

uncertainty of the flowmeter that is described by the manufacturer's specifications, and because this uncertainty is below the target value, all trials meet the target. The total mass transfer can still provide useful insights, however, because for example, the two trials with the highest uncertainty with respect to NO_3^- can be seen to exhibit anomalous behavior in the total mass transfer as well. Both Trial 10 – Replication 2 and Trial 14 – Replication 3 report mass transfers that are orders of magnitude smaller than the other replications for the same trials. On the other hand, the trials with the highest uncertainty with respect to Nd^{3+} seem to show nominal behavior with respect to the total mass transfer.

Table 21. Estimated total transferred mass and relative uncertainty.

Trial	Rep.	Solution	Mass (kg)	$u_c(m)$ (kg)	$u_r(m)$ (%)	Success	Dominant category
1	1	Surrogate	5402.1000	10.8048	0.20	TRUE	flowmeter_systematic
1	2	Surrogate	5418.4688	10.8375	0.20	TRUE	flowmeter_systematic
1	3	Surrogate	5411.7425	10.8240	0.20	TRUE	flowmeter_systematic
2	1	Surrogate	5379.0485	10.7585	0.20	TRUE	flowmeter_systematic
3	1	Surrogate	5386.6508	10.7738	0.20	TRUE	flowmeter_systematic
4	1	Surrogate	1722.3917	3.4453	0.20	TRUE	flowmeter_systematic
4	2	Surrogate	1740.7363	3.4820	0.20	TRUE	flowmeter_systematic
4	3	Surrogate	1783.2688	3.5671	0.20	TRUE	flowmeter_systematic
5	1	Surrogate	1837.6181	3.6758	0.20	TRUE	flowmeter_systematic
5	2	Surrogate	1746.7213	3.4940	0.20	TRUE	flowmeter_systematic
5	3	Surrogate	1734.7721	3.4701	0.20	TRUE	flowmeter_systematic
6	1	Surrogate	2270.4076	4.5412	0.20	TRUE	flowmeter_systematic
7	1	Dilution 1	2596.2338	5.1930	0.20	TRUE	flowmeter_systematic
7	2	Dilution 1	3624.6088	7.2498	0.20	TRUE	flowmeter_systematic
7	3	Dilution 1	5095.6133	10.1918	0.20	TRUE	flowmeter_systematic
8	1	Dilution 1	4963.4876	9.9273	0.20	TRUE	flowmeter_systematic
8	2	Dilution 1	5216.6878	10.4339	0.20	TRUE	flowmeter_systematic
9	1	Dilution 1	695.9708	1.3925	0.20	TRUE	flowmeter_systematic
9	2	Dilution 1	1735.3277	3.4712	0.20	TRUE	flowmeter_systematic
9	3	Dilution 2	1830.8562	3.6623	0.20	TRUE	flowmeter_systematic
10	1	Dilution 1	1695.6039	3.3918	0.20	TRUE	flowmeter_systematic
10	2	Dilution 1	174.9860	0.3505	0.20	TRUE	flowmeter_systematic
10	3	Dilution 2	1720.6360	3.4418	0.20	TRUE	flowmeter_systematic
10	4	Dilution 2	1728.2230	3.4570	0.20	TRUE	flowmeter_systematic
11	1	Dilution 2	4554.5977	9.1097	0.20	TRUE	flowmeter_systematic
11	2	Dilution 2	1988.8391	3.9782	0.20	TRUE	flowmeter_systematic
11	3	Dilution 2	5017.9490	10.0364	0.20	TRUE	flowmeter_systematic
12	1	Dilution 2	5062.3093	10.1251	0.20	TRUE	flowmeter_systematic
12	2	Dilution 2	4987.8481	9.9761	0.20	TRUE	flowmeter_systematic
13	1	Dilution 2	1706.5458	3.4136	0.20	TRUE	flowmeter_systematic
13	2	Dilution 2	1699.9677	3.4005	0.20	TRUE	flowmeter_systematic

13	3	Dilution 2	1704.3531	3.4093	0.20	TRUE	flowmeter_systematic
14	1	Dilution 2	1714.5906	3.4297	0.20	TRUE	flowmeter_systematic
14	2	Dilution 2	1710.8822	3.4223	0.20	TRUE	flowmeter_systematic
14	3	Dilution 2	741.3680	1.4832	0.20	TRUE	flowmeter_systematic
15	1	Dilution 2	1684.9281	3.3704	0.20	TRUE	flowmeter_systematic
15	2	Dilution 2	937.2467	1.8749	0.20	TRUE	flowmeter_systematic
16	1	Dilution 2	1381.1704	2.7629	0.20	TRUE	flowmeter_systematic
16	2	Dilution 2	1528.3599	3.0571	0.20	TRUE	flowmeter_systematic

6.4 Mass measurement comparison

Three sensors (the floor scale under Tank 1, the floor scale under Tank 2, and the Coriolis flowmeter) can each be used to make independent measurements of the total mass transferred. Additionally, any of these measurements can be combined with any other using inverse variance weighting to produce a combined estimate of mass transfer, often with lower uncertainty. In this section, using the Trial 3, Replicate 1 as an example, we can examine the different methods for measuring mass transfer, and different masks for detecting invalid concentration predictions.

In Figure 33 and Figure 34 (lefthand plots) we see the estimated mass transfer of Nd^{3+} and NO_3^-, respectively, computed with no concentration mask. The 4 bars on the right, labeled as "average concentration", denote estimates of the mass transfer where the total mass delta is computed as the final mass minus the initial mass, and the concentration is the average concentration estimated using the immersion probes throughout the duration of the trial. These estimates assume that the concentration is constant and the solution is homogenous, which are appropriate assumptions for generating a reference value in these illustrative examples, but may not be true in practice. The other bars, labeled as "incremental", denote the methods being examined by this project. They compute the mass transfer by the incremental change mass at each time step.

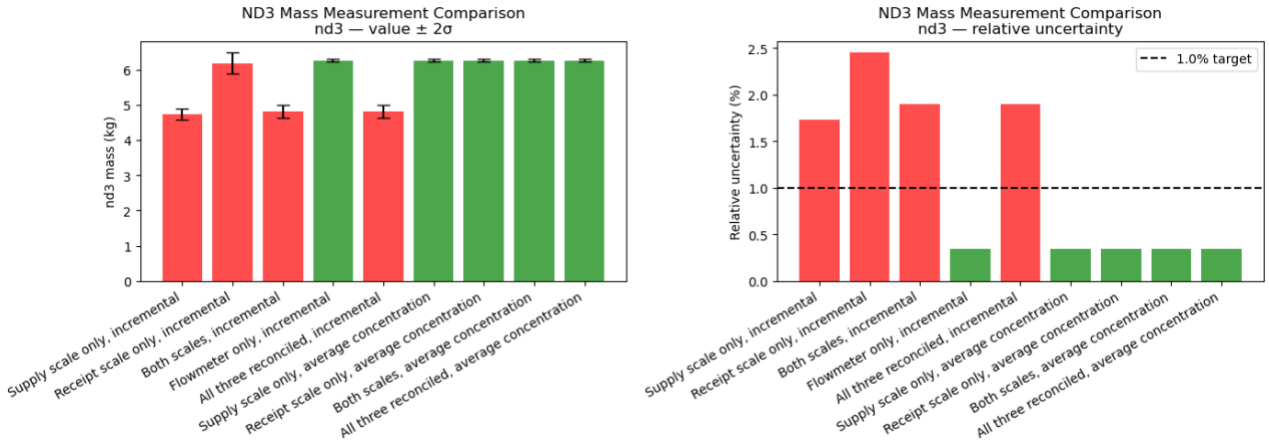


Figure 33. Mass measurement options for Nd^{3+} using no mask (left) and associated relative uncertainty (right).

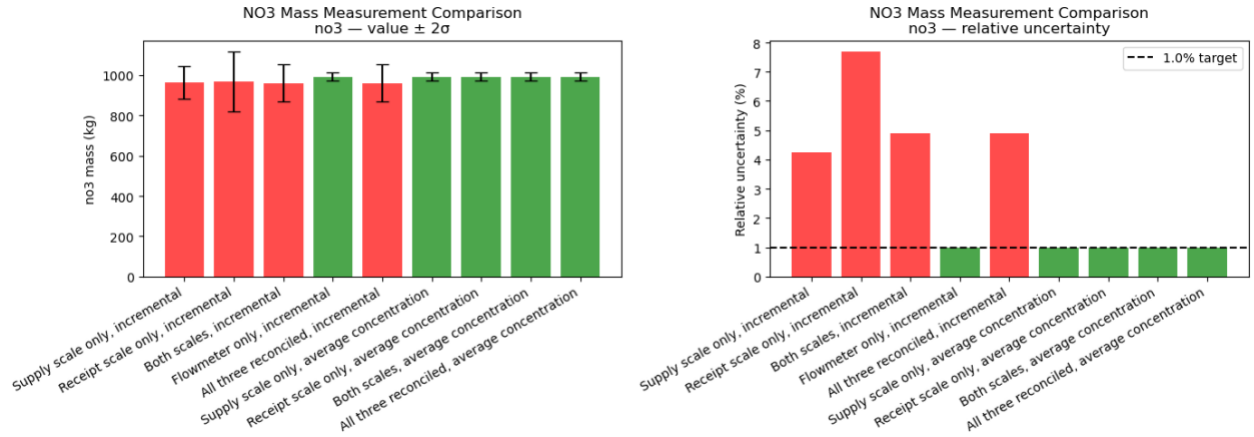


Figure 34. Mass measurement options for NO_3^- using no mask (left) and associated relative uncertainty (right).

We can see that the "incremental" estimates that include the supply scale, WIT-200, significantly underestimate the transferred mass of Nd^{3+} and fail to meet the success criterion, as shown in the righthand plot of Figure 33. On the other hand, for NO_3^-, all methods that include the floor scales have high uncertainty, even though their estimated values are relatively close to the reference values. The only incremental method that meets the success criterion and approximates the reference values for both analytes is the flowmeter method.

Based on these comparisons, we present results using the flowmeter incremental mass measurement method. Additional plots showing the mass transfer and relative uncertainty using the various masking strategies can be seen in Appendix B.

6.5 Example UQ Output

The data analysis software developed as part of this project to perform material accountancy and uncertainty quantification generates log files for each trial that document the complete uncertainty budget of the trial. An example log file for Trial 3, Replication 1, where the target is met for Nd^{3+} but not met for NO_3^-, is provided in this section.

```
======================================================================
MASS BALANCE EXPERIMENT — Transfer_Run_Exp5
Experiment number: 5.0
Rows processed:    33627
Tracks present:    ['T05_uv_vis', 'T01_uv_vis', 'T03_uv_vis', 'T05_raman', 'T01_raman', 'T03_raman']
Pump cycles:       36
Elapsed time:      19.0s
WIT-200 calibration: CalibrationCurve(WIT-200): 42 points, range [778, 5019] kg, LOO-RMSE=0.463 kg
WIT-300 calibration: CalibrationCurve(WIT-300): 35 points, range [613, 4318] kg, LOO-RMSE=0.418 kg
======================================================================
```

Liquid mass balance

Supply delta: 5058.0992 ± 6.0703 kg (0.12%)

(averaged over 100 start and 100 end readings)

Receipt delta: 5075.4616 ± 5.6651 kg (0.11%)

(averaged over 100 start and 100 end readings)

Flow integral: 5386.6508 ± 10.7738 kg (0.20%)

Discrepancy: -17.3624 ± 8.3031 kg (47.82%)

Consistent: YES

Best estimate: 5067.3792 ± 4.1417 kg (0.08%)

Analyte mass balance — nd3

Flow-integrated: 6.4511 ± 0.0342 kg (0.53%)

Scale-weighted: 6.1228 ± 0.0282 kg (0.46%)

Best estimate: 6.2556 ± 0.0218 kg (0.35%)

1% target: PASS ✓

Valid spectra: 452 (100.0% of unique timestamps)

Strategy breakdown:

Mean concentration: 0.0012 ± 0.0000 kg/L (0.45%)

Analyte mass balance — no3

Flow-integrated: 1023.7193 ± 15.0106 kg (1.47%)

Scale-weighted: 967.0192 ± 13.0685 kg (1.35%)

Best estimate: 991.4662 ± 9.8564 kg (0.99%)

1% target: PASS ✓

Valid spectra: 353 (100.0% of unique timestamps)

Strategy breakdown:

Mean concentration: 0.1908 ± 0.0026 kg/L (1.35%)

==========

EXPERIMENT RECONCILIATION SUMMARY

==========

Reconciliation — liquid_mass (kg)

Label	Value	Std	Rel%	Weight%
flowmeter (AIT-250)	5386.650783	10.773826	0.200%	100.0%

```
  Best estimate                5386.650783  10.773826   0.200%
  Birge ratio:     0.000 (threshold 2.0) — CONSISTENT ✓
  Chi-squared:     0.000 (dof=0)
  1% target:       PASS ✓

Reconciliation — nd3_mass (kg)
  Label                        Value       Std     Rel%  Weight%
  ------------------------------------------------------------------------
  nd3_flow_integrated              6.451125   0.034232   0.531%   100.0%
  ------------------------------------------------------------------------
  Best estimate                    6.451125   0.034232   0.531%
  Birge ratio:     0.000 (threshold 2.0) — CONSISTENT ✓
  Chi-squared:     0.000 (dof=0)
  1% target:       PASS ✓

Reconciliation — no3_mass (kg)
  Label                        Value       Std     Rel%  Weight%
  ------------------------------------------------------------------------
  no3_flow_integrated           1023.719320  15.010572   1.466%   100.0%
  ------------------------------------------------------------------------
  Best estimate                1023.719320  15.010572   1.466%
  Birge ratio:     0.000 (threshold 2.0) — CONSISTENT ✓
  Chi-squared:     0.000 (dof=0)
  1% target:       FAIL ✗
========================================================================

1% uncertainty target (relative std ≤ 1.0%):
  nd3: 0.531%  PASS ✓
  no3: 1.466%  FAIL ✗
========================================================================

================================================================================
UNCERTAINTY BUDGET REPORT   (target: ≤ 1.0%)
================================================================================

Uncertainty Budget — liquid_mass (kg)
  Best estimate:  5386.65 ± 10.7738 kg (0.200%)
```

1.0% target: PASS ✓

Source	Category	Std	%Var
flowmeter_systematic	Flowmeter	10.773302	99.99%
flowmeter_random	Flowmeter	0.106305	0.01%
TOTAL		10.773826	100.00%

Category totals:

Flowmeter	10.773826	100.00%

Uncertainty Budget — nd3_mass (kg)

Best estimate: 6.45113 ± 0.0342322 kg (0.531%)

1.0% target: PASS ✓

Source	Category	Std	%Var
uv_vis_T01_rmsep	PLS model (RMSEP)	0.034009	98.70%
uv_vis_T03_rmsep	PLS model (RMSEP)	0.003784	1.22%
uv_vis_T01_mc_std	PLS spectral noise	0.000934	0.07%
uv_vis_T03_mc_std	PLS spectral noise	0.000091	0.00%
nd3_flowmeter_systematic	Flowmeter	0.000017	0.00%
nd3_flowmeter_random	Flowmeter	0.000000	0.00%
nd3_concentration_drift	Concentration drift	0.000000	0.00%
TOTAL		0.034232	100.00%

Category totals:

PLS model (RMSEP)	0.034219	99.92%
PLS spectral noise	0.000938	0.08%
Flowmeter	0.000017	0.00%

```
  Concentration drift              0.000000   0.00%

Uncertainty Budget — no3_mass (kg)
  Best estimate:  1023.72 ± 15.0106 kg (1.466%)
  1.0% target: FAIL ✗

  Source                     Category                Std     %Var
  ──────────────────────────────────────────────────────────────────────
  no3_concentration_drift    Concentration drift     12.265488  66.77%
  raman_T01_mc_std           PLS spectral noise       5.900292  15.45%
  raman_T03_mc_std           PLS spectral noise       5.700259  14.42%
  no3_flowmeter_systematic   Flowmeter                2.057452   1.88%
  raman_T01_rmsep            PLS model (RMSEP)        1.768885   1.39%
  raman_T03_rmsep            PLS model (RMSEP)        0.454095   0.09%
  no3_flowmeter_random       Flowmeter                0.020403   0.00%
  ──────────────────────────────────────────────────────────────────────
  TOTAL                                              15.010572 100.00%

  Category totals:
    Concentration drift          12.265488  66.77%
    PLS spectral noise            8.204047  29.87%
    Flowmeter                     2.057553   1.88%
    PLS model (RMSEP)             1.826241   1.48%

================================================================================
FINAL RESULT:
  liquid_mass        5386.65 ± 10.7738 kg  (0.200%)  PASS ✓
  nd3_mass           6.45113 ± 0.0342322 kg  (0.531%)  PASS ✓
  no3_mass           1023.72 ± 15.0106 kg  (1.466%)  FAIL ✗

  Overall: ONE OR MORE FAIL ✗
```

6.6 Analysis of Monte Carlo Simulations

Trial 10 – Replication 4 was used to explore the relationship between the incremental mass difference in supply tank; incremental mass difference in receipt tank, and the concentration of NO_3^- and Nd^{3+} predicted using Raman and UV-vis chemometric models, respectively. This trial represents a transfer of the Dilution 2 solution from the supply tank to the receipt tank.

In the figures that follow, the same data is repeated in three pairs of plots. Each pair includes one figure to represent the concentration of NO_3^- and one to represent Nd^{3+}. The difference between the three pairs of figures is that the data are color-coded in each pair of figures according to different masking strategies. Figure 35 and Figure 36 encode a masking strategy based on the Q-residual. Figure 37 and Figure 38 use the associated Hotelling T^2 statistic, and Figure 39 and Figure 40 color-coded according to the drive phase for the power fluidics pump.

For each pair of plots the relationship between the incremental mass difference of the supply tank (top row) and receipt tank (bottom row) is compared to the time since the beginning of the trial (left column) and predicted analyte concentration (right column). The concentration of Nd^{3+} and NO_3^- as measured by the laboratory standard addition is represented as dashed line in each plot. When the flow cells are full, and the analytes NO_3^- or Nd^{3+} are present in the flow cells, the concentration predictions concentrate around these dashed lines, as we can see in Figure 35 and Figure 36 (right column). However, when the incremental mass difference is small, the analytes are not present in the flow cells. As a result, the variance of analyte concentration predictions is much greater when the incremental mass difference is close to 0. The mass balance of receipt tanks depicts a stronger relation to presence or absence of analyte NO_3^- and Nd^{3+} in tracks.

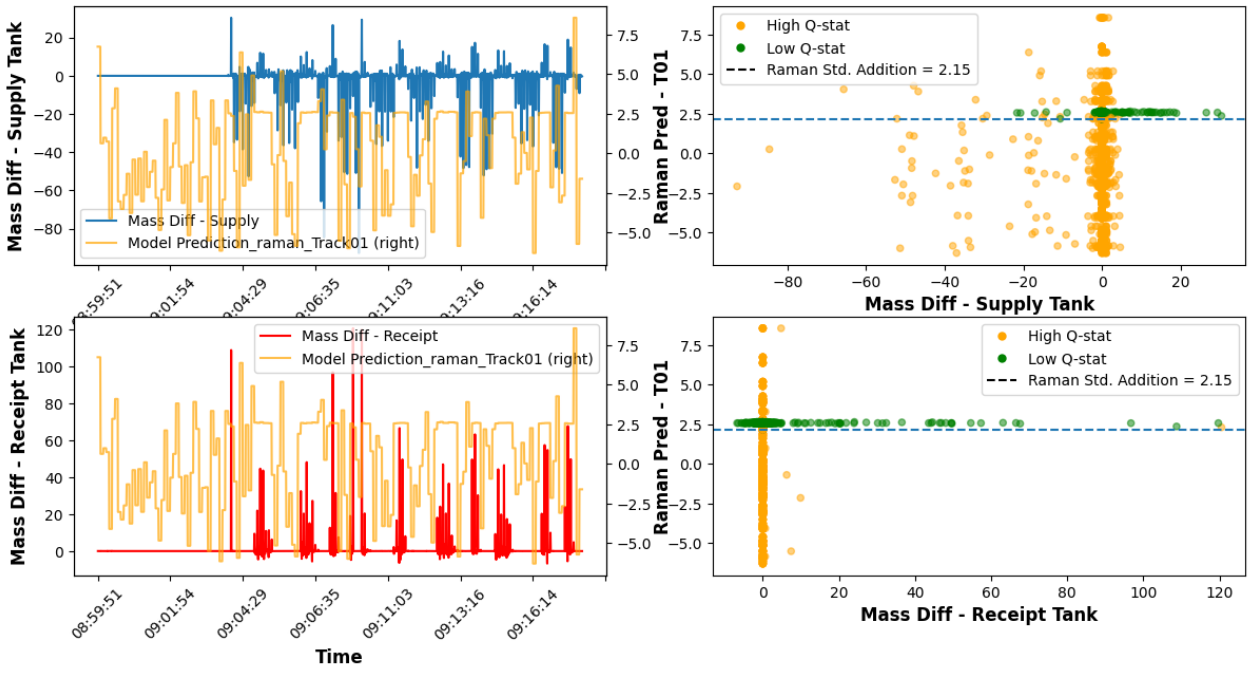


Figure 35. Q-residual analysis for NO_3^-.

The color-coded points in the right column of in Figure 35 and Figure 36 indicate high or low values of the Q-residual statistic. We see that the points colored green, which all have high Q-residual scores, all approximate the analyte concentrations measured by the lab standard addition much better than the points with a low Q-residual score. On the other hand, when the incremental mass difference is 0 or negative, the concentration predictions are far from the laboratory-measured concentrations and have much greater variance.

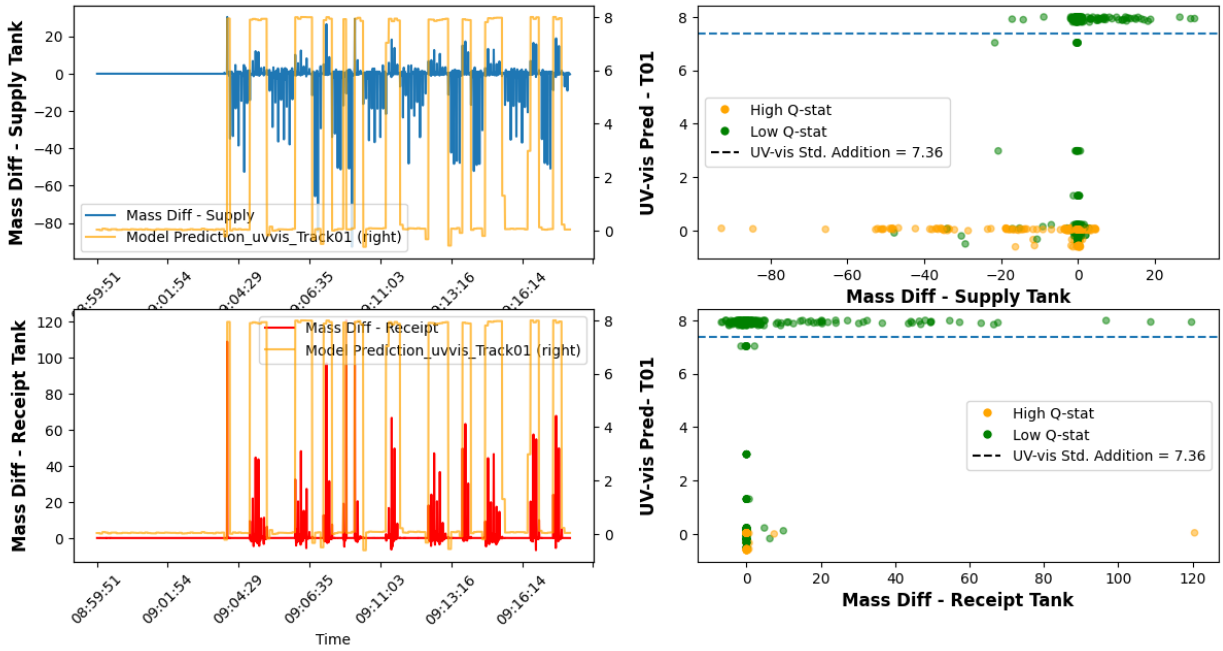


Figure 36. Q-residual analysis for Nd^{3+}.

We see similar trends in Figure 37 and Figure 38 with respect to the associated Hotelling T^2 statistic, and with respect to the drive phase of the power fluidics pump in Figure 39 and Figure 40, (where Drive – 0 means PFOOS system was in the charge or drain phases, and Drive – 1 means PFOOS system was in the drive phase). This indicates that any of these three strategies would be useful in masking invalid concentration predictions and reducing overall uncertainty.

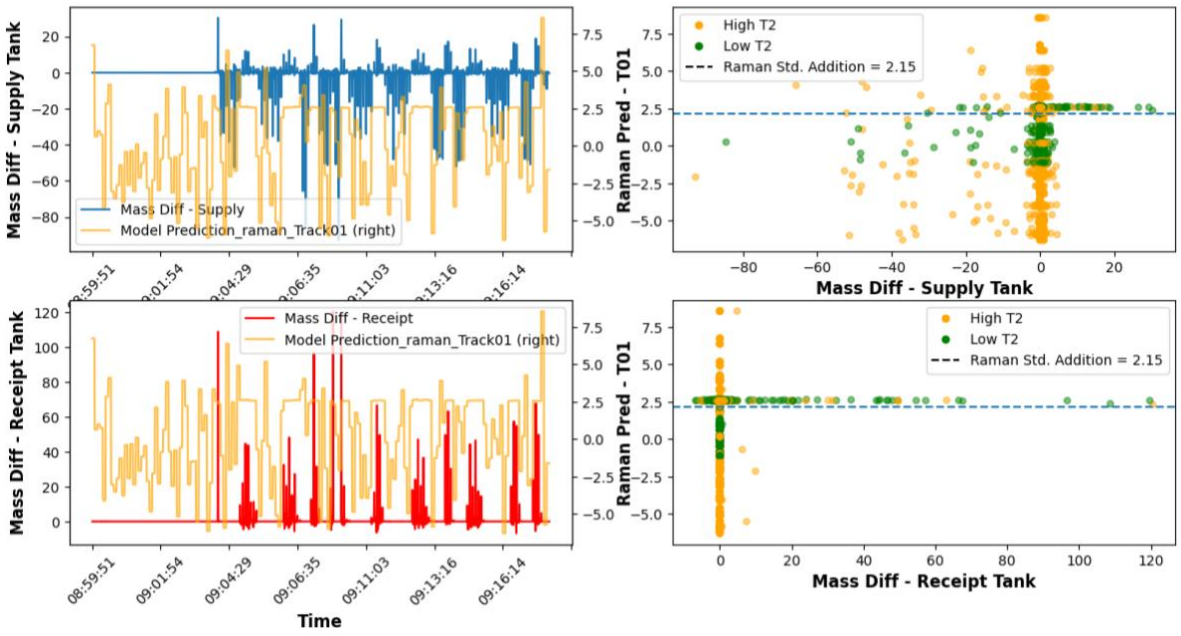


Figure 37. Hotelling T^2 statistic analysis for NO_3^-.

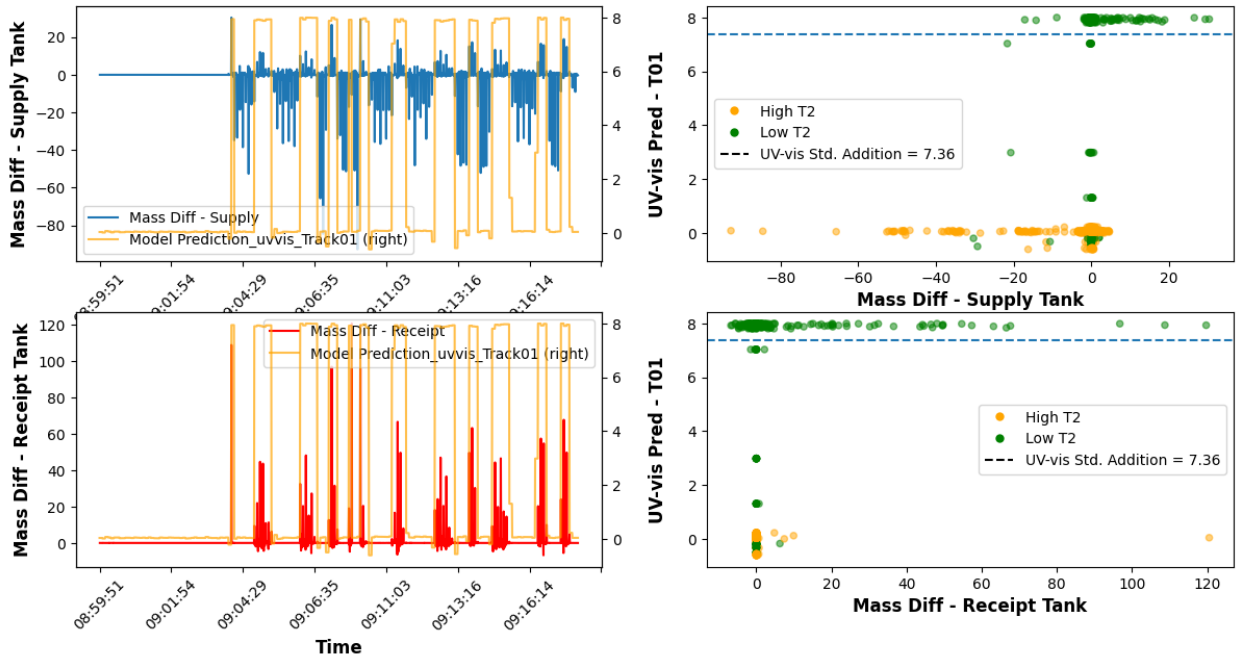


Figure 38. Hotelling T^2statistic analysis for Nd^{3+}.

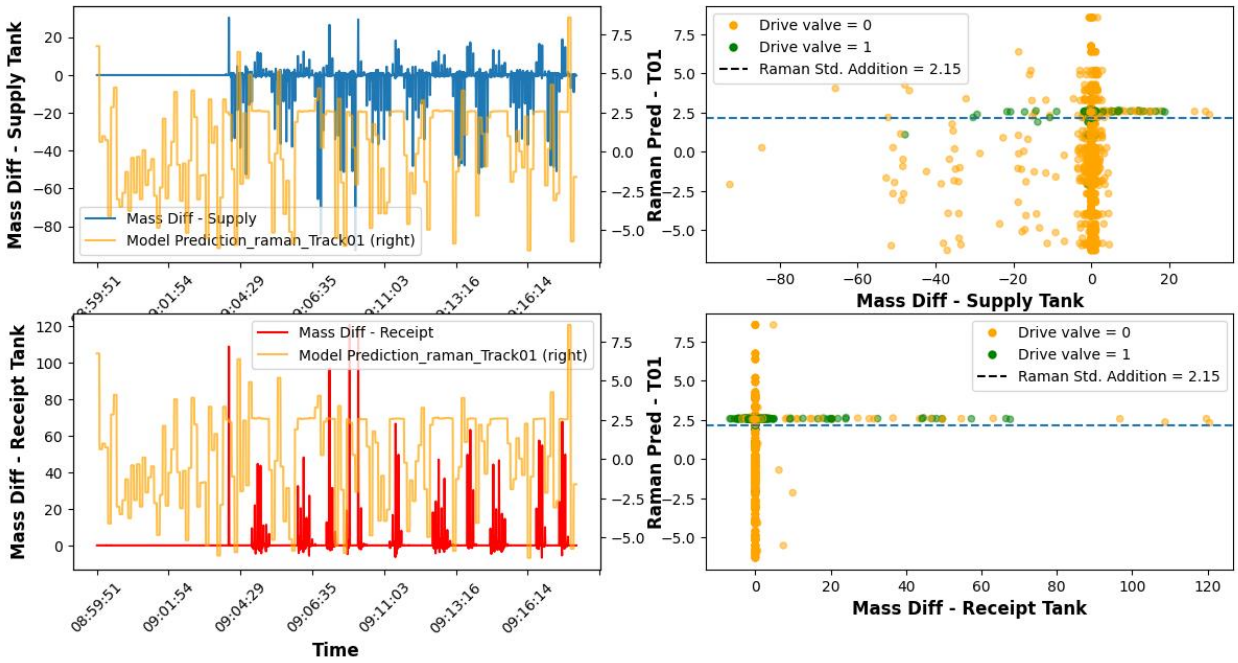


Figure 39. Drive phase mask analysis for NO_3^-.

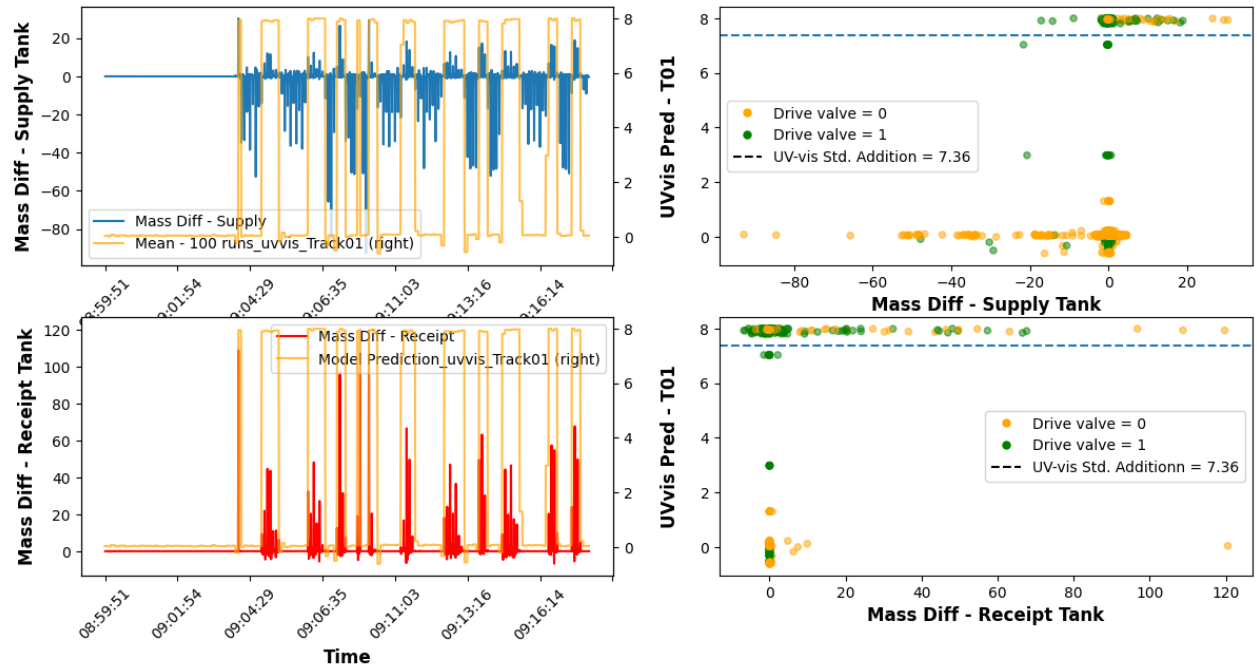


Figure 40. Drive phase mask analysis for Nd^{3+}.

7.0 Conclusions and Next Steps

This project demonstrated the feasibility of integrating online monitoring (OLM) with NuVision Engineering's Power Fluidics pilot-scale test rig to perform real-time material mass balances for used nuclear fuel reprocessing. The primary objective was to determine whether mass-balance uncertainty could be maintained within ±1% of the actual value. The demonstration achieved this goal under the defined operating conditions and assumptions. Importantly, the work also clarified which process and measurement assumptions most strongly influence uncertainty and must be validated for future industrial deployment.

The project combined optical spectroscopy with independent measurements of total solution mass. Visible absorbance spectroscopy was used to quantify neodymium (Nd), a nonradioactive surrogate for transuranic elements such as plutonium, while Raman spectroscopy was used to monitor nitrate as a surrogate for nitric acid. Chemometric models converted optical signals into real-time concentration measurements. These data were combined with total-mass measurements obtained either from floor scales beneath receipt tanks or from an inline flowmeter, enabling calculation of mass balances for individual chemical species. Comparisons of the two mass-measurement approaches provided insight into their relative contributions to overall uncertainty.

Several notable technical advancements were achieved:

- **Pilot-scale sensor development and integration:** The team designed, built, and demonstrated optical sensors for both flowing process streams and immersion in feed and receipt tanks. A novel flow-cell configuration was designed to enable switching between cells for referencing, maintenance, and component replacement, improving system flexibility and maintainability.

- **Real-time data analysis:** Automated data-handling and chemometric tools were developed to quantify chemical concentrations from optical measurements in real time. These tools were adapted to the flow behavior and operating characteristics of the Power Fluidics system, extending methods previously demonstrated primarily at bench scale.

- **Multi-stream data fusion:** The project developed data-fusion and uncertainty-analysis tools that combined concentration, flow, and total-mass measurements to calculate mass balances. This work advanced understanding of how sensor performance, process hold-up, flow behavior, calibration, and environmental conditions affect uncertainty.

- **Model transfer and maintainability:** Chemometric models developed using one flow cell were successfully extended to additional flow cells and in-tank probes. This demonstrated an initial pathway toward transferable, "plug-and-play" calibration models and model-maintenance approaches needed for broader industrial deployment.

- **Representative pilot-scale demonstration:** Integration of PNNL's optical monitoring capabilities with NuVision's Power Fluidics platform demonstrated that the combined system can support real-time process monitoring and material accountancy in a representative aqueous-processing environment.

The results support OLM as a potentially cost-effective tool for improving process control, material accountancy, and upset avoidance in future fuel-recycling facilities. The work is particularly relevant as interest grows in recycling used nuclear fuel to address accumulating inventories, support advanced reactor fuel cycles, and reduce waste-management challenges. Although the ±1% target was met, the result depends on assumptions regarding process progression, material hold-up, sensor calibration, flow behavior, and other operating conditions. Validating and reducing the uncertainty associated with these assumptions is therefore the most important technical finding and a key requirement for industry adoption.

Recommended Immediate Next Steps:

1. **Improve process measurement accuracy** by redesigning the flow cells and flowmeter configuration to ensure they remain completely filled during operation. Repeating selected PFOOS experiments under these improved conditions will eliminate the need to discount blank data and further reduce measurement uncertainty.

2. **Progress development of an auto-calibration optical sensor** to facilitate its deployment in a shielded environment without the need for backup systems.

3. **Automate data acquisition and analysis** by developing an integrated data management architecture that minimizes the extensive manual intervention required during the PFOOS project. While largely invisible to program demonstrations, this capability is expected to significantly reduce data processing time, improve repeatability, and lower the overall cost of future deployments.

Recommended Medium-Term Next Steps:

1. **Advance automated calibration and data-science tools** to reduce deployment complexity, support calibration transfer across sensors, and enable autonomous detection and correction of sensor drift.

2. **Conduct additional pilot-scale testing** across a wider range of flow rates, concentrations, temperatures, process conditions, and transient events to validate the assumptions used in the uncertainty framework. These efforts should also include further quantifying material hold-up and process timing effects, which can materially influence real-time mass-balance accuracy.

3. **Harden the optical sensors and Power Fluidics platform** for radiation exposure, corrosive environments, maintenance constraints, and variable operating conditions.

4. **Develop deployment guidance and performance requirements** that connect demonstrated uncertainty levels with safeguards, process-control, and industrial operating needs.

Overall, the project met its primary performance objective while delivering important sensor, modeling, integration, and uncertainty-analysis advances that establish a foundation for accelerating OLM deployment in nuclear fuel-reprocessing applications.

8.0 References

Albert, Daniel R. 2020. "Monte Carlo Uncertainty Propagation with the NIST Uncertainty Machine." *Journal of Chemical Education*: 1491–1494.

Allegrini, Franco, and Alejandro C. Olivieri. 2014. "IUPAC-Consistent Approach to the Limit of Detection in Partial Least-Squares Calibration." *Analytical Chemistry* 86 (15): 7858–7866. https://doi.org/10.1021/ac501786u.

Arm, S. T., C. W Enderlin, and A. Lines. 2023. *Online Optical Spectroscopy Information Supporting Decision to Proceed to Design.* PNNL-34951 (Richland, Washington).

Birge, Raymond T. 1932. "The calculation of errors by the method of least squares." *Physical Review*: 207.

Bodnar, Olha, and Elster Clemens. 2014. "On the adjustment of inconsistent data using the Birge ratio." *Metrologia*: 516–521.

Branch, Shirmir D., Heather M. Felmy, Adan Schafer Medina, Samuel A. Bryan, and Amanda M. Lines. 2023. "Exploring the Complex Chemistry of Uranium within Molten Chloride Salts." *Industrial & Engineering Chemistry Research* 62 (37): 14901–14909. https://doi.org/10.1021/acs.iecr.3c02005.

Bryan, S. A. , T.G. Levitskaia, and S. N. Schlahta. 2008. "Raman Based Process Monitor For Continuous Real-Time Analysis of High Level Radioactive Waste Components." Waste Management WM2008 Conference, Phoenix, AZ, February 24 –28, 2008.

Bryan, S. A., T. G. Levitskaia, A. M. Johnsen, C. R. Orton, and J. M. Peterson. 2011. "Spectroscopic monitoring of spent nuclear fuel reprocessing streams: an evaluation of spent fuel solutions via Raman, visible, and near-infrared spectroscopy." *Radiochimica Acta* 99 (9): 563–571. https://doi.org/10.1524/ract.2011.1865. <Go to ISI>://WOS:000294789600005.

Bryan, S. A., T. G. Levitskaia, and S. I. Sinkov. 2004. *Chemical and Radiochemical Stability of the Process Monitor System used in the Raman Probe System Project; Report #47187.* (Pacific Northwest National Laboratory, Richland WA 99352).

Bryan, S. A., T. G. Levitskaia, S. I. Sinkov, S. N. Schlahta, and J. M. Shaver. 2006. "Raman based process monitor for continuous real-time analysis of high level radioactive waste components." *Abstracts of Papers of the American Chemical Society* 232: 852–852.

Bryan, S.A. 2008. Raman Analysis of Aqueous Solutions, PNNL Procedure RPG-CMC-240. Pacific Northwest National Laboratory, Richland, Washington.

Bryan, Samuel A., Tatiana G. Levitskaia, Amanda M. Lines, Frances N. Smith, Gary B. Josephson, and Job M. Bello. 2013. "Dual-Remote Raman Technology for In-Situ Identification of Tank Waste." WM Symposia 2013: International Collaboration and Continuous Improvement, Phoenix, Arizona.

Clifford, A. J., H. E. Lackey, G. L. Nelson, S. A. Bryan, and A. M. Lines. 2021. "Raman Spectroscopy Coupled with Chemometric Analysis for Speciation and Quantitative Analysis of Aqueous Phosphoric Acid Systems." *Anal Chem* 93 (14): 5890–5896. https://doi.org/10.1021/acs.analchem.1c00244.

de Jong, Sijmen. 1993. "SIMPLS: An alternative approach to partial least squares regression." *Chemometrics and Intelligent Laboratory Systems* 18 (3): 251–263. https://doi.org/10.1016/0169-7439(93)85002-X.

Edwards M.K., P.P. Schonewill, R.W. Shimskey, C. M. Niver, S.A. Bryan, R.A. Peterson, and C. Smith. 2011. "Real Time Raman Analysis of Near Tank Treatment System Process Streams." 17th Symposium on Separation Science & Technology for Energy Applications, Gatlinburg, Tennessee, PNWD-SA-9504.

"Evaluation of measurement data—Guide to the expression of uncertainty in measurement." 2008. *JCGM*: 1–116.

Felmy, H. M., A. J. Clifford, A. S. Medina, R. M. Cox, J. M. Wilson, A. M. Lines, and S. A. Bryan. 2021. "On-Line Monitoring of Gas-Phase Molecular Iodine Using Raman and Fluorescence Spectroscopy Paired with Chemometric Analysis." *Environ Sci Technol*. https://doi.org/10.1021/acs.est.0c06137.

Felmy, Heather M., Nathan P. Bessen, Hope E. Lackey, Samuel A. Bryan, and Amanda M. Lines. 2023. "Quantification of Uranium in Complex Acid Media: Understanding Speciation and Mitigating for Band Shifts." *ACS Omega* 8 (44): 41696–41707. https://doi.org/10.1021/acsomega.3c06007.

Felmy, Heather M., Nikolas T. C. Boily, Adan Schafer Medina, Poki Tse, Amy M. Westesen, Job M. Bello, Samuel A. Bryan, and Amanda M. Lines. 2026. "Raman Spectroscopic In Situ Monitoring of Highly Turbid Media." *Analytical Chemistry* 98 (11): 8594–8604. https://doi.org/10.1021/acs.analchem.6c00332.

Felmy, Heather M., Hope E. Lackey, Adan Schafer Medina, Michael J. Minette, Samuel A. Bryan, and Amanda M. Lines. 2022. "Leveraging Multiple Raman Excitation Wavelength Systems for Process Monitoring of Nuclear Waste Streams." *ACS ES&T Water* 2 (3): 465–473. https://doi.org/10.1021/acsestwater.1c00408.

Fritsch, Frederick N., and Judy Butland. 1984. "A method for constructing local monotone piecewise cubic interpolants." *SIAM journal on scientific and statistical computing*: 300–304.

Fuller, W. A. 1987. *Measurement error models,*. New York, N.Y.: John Wiley.

Gardenier, George H., Feng Gui, and James N. Demas. 2011. "Error Propagation Made Easy—Or at Least Easier." *Journal of Chemical Education*: 916–920.

Kacker, Raghu N., Rüdiger Kessel, and Klaus-Dieter Sommer. 2010. "Assessing differences between results determined according to the guide to the expression of uncertainty in measurement." *Journal of research of the national institute of Standards and Technology*: 453.

Kurath, DE. 2009. Pretreatment Engineering Platform: Phase 1 Final Test Report, Pacific Northwest National Laboratory, Richland, WA, PNNL-18894 WTP-RPT-197, Rev 0.

Lackey, H. E., G. L. Nelson, A. M. Lines, and S. A. Bryan. 2020. "Reimagining pH Measurement: Utilizing Raman Spectroscopy for Enhanced Accuracy in Phosphoric Acid Systems." *Analytical Chemistry* 92 (8): 5882–5889. https://doi.org/10.1021/acs.analchem.9b05708.

Lackey, Hope E., Alyssa F. Espley, Savannah M. Potter, Fabrice Lamadie, Manuel Miguirditchian, Gilbert L. Nelson, Samuel A. Bryan, and Amanda M. Lines. 2024. "Quantification of Lanthanides on a PMMA Microfluidic Device with Three Optical Pathlengths Using PCR of UV–Visible, NIR, and Raman Spectroscopy." *ACS Omega* 9 (37): 38548–38556. https://doi.org/10.1021/acsomega.4c03857. https://doi.org/10.1021/acsomega.4c03857.

Lines, A. M., S. R. Adami, S. I. Sinkov, G. J. Lumetta, and S. A. Bryan. 2017. "Multivariate Analysis for Quantification of Plutonium(IV) in Nitric Acid Based on Absorption Spectra." *Analytical Chemistry* 89 (17): 9354–9359. https://doi.org/10.1021/acs.analchem.7b02161. <Go to ISI>://WOS:000410014900106.

Lines, A. M., J. M. Bello, C. Gasbarro, and S. A. Bryan. 2022a. "Combined Raman and Turbidity Probe for Real-Time Analysis of Variable Turbidity Streams." *Analytical Chemistry* 94: 3652−3660. https://doi.org/10.1021/acs.analchem.1c05228.

Lines, A. M., P. Tse, H. M. Felmy, J. M. Wilson, J. Shafer, K. M. Denslow, A. N. Still, C. King, and S. A. Bryan. 2019. "Online, Real-Time Analysis of Highly Complex Processing Streams: Quantification of Analytes in Hanford Tank Sample." *Industrial & Engineering Chemistry Research* 58 (47): 21194–21200. https://doi.org/10.1021/acs.iecr.9b03636.

Lines, Amanda M., Job M. Bello, Christina Gasbarro, and Samuel A. Bryan. 2022b. "Combined Raman and Turbidity Probe for Real-Time Analysis of Variable Turbidity Streams." *Analytical Chemistry* 94 (8): 3652–3660. https://doi.org/10.1021/acs.analchem.1c05228.

Lines, Amanda M., G. B. Hall, S. I. Sinkov, T Levitskaia, N. B. Gallagher, Gregg J. Lumetta, and Samuel A. Bryan. 2020. "Overcoming oxidation state dependent spectral interferences: On-line monitoring of U(VI) reduction to U(IV) via Raman and UV-vis spectroscopy " *Ind. Eng. Chem. Res.* 59: 8894–8901. https://doi.org/10.1021/acs.iecr.9b06706.

Lines, Amanda M., Gabriel B. Hall, Susan Asmussen, Jarrod Allred, Sergey Sinkov, Forrest Heller, Neal Gallagher, Gregg J. Lumetta, and Samuel A. Bryan. 2020a. "Sensor Fusion: Comprehensive Real-Time, On-Line Monitoring for Process Control via Visible, Near-Infrared, and Raman Spectroscopy." *ACS Sensors* 5 (8): 2467–2475. https://doi.org/10.1021/acssensors.0c00659.

---. 2020b. "Sensor Fusion: Comprehensive Real-Time, On-Line Monitoring for Process Control via Visible, Near-Infrared, and Raman Spectroscopy." *ACS Sensors*. https://doi.org/10.1021/acssensors.0c00659.

Lines, Amanda M., Gilbert L. Nelson, Amanda J. Casella, Job M. Bello, Sue B. Clark, and Samuel A. Bryan. 2018. "Multivariate Analysis To Quantify Species in the Presence of Direct Interferents: Micro-Raman Analysis of HNO3 in Microfluidic Devices." *Analytical Chemistry* 90 (4): 2548–2554. https://doi.org/10.1021/acs.analchem.7b03833. https://doi.org/10.1021/acs.analchem.7b03833.

Martens, Harald, and Tormod Næs. 1984. "Multivariate Calibration." In *Chemometrics: Mathematics and Statistics in Chemistry*, edited by Bruce R. Kowalski, 147–156. Dordrecht: Springer Netherlands.

Mohr, Peter J., Barry N. Taylor, and David B. Newell. 2008. "CODATA recommended values of the fundamental physical constants: 2006." *Journal of Physical and Chemical Reference Data*: 1187–1284.

Nee, K., S. A. Bryan, T. G. Levitskaia, J. W. J. Kuo, and M. Nilsson. 2018. "Combinations of NIR, Raman spectroscopy and physicochemical measurements for improved monitoring of solvent extraction processes using hierarchical multivariate analysis models." *Analytica Chimica Acta* 1006: 10–21. https://doi.org/10.1016/j.aca.2017.12.019.

Nelson, G. L., S. E. Asmussen, A. M. Lines, A. J. Casella, D. R. Bottenus, S. B. Clark, and S. A. Bryan. 2018. "Micro-Raman Technology to Interrogate Two-Phase Extraction on a Microfluidic Device." *Analytical Chemistry* 90 (14): 8345–8353. https://doi.org/10.1021/acs.analchem.7b04330.

Nelson, G. L., H. E. Lackey, J. M. Bello, H. M. Felmy, H. B. Bryan, F. Lamadie, S. A. Bryan, and A. M. Lines. 2021. "Enabling Microscale Processing: Combined Raman and Absorbance Spectroscopy for Microfluidic On-Line Monitoring." *Analytical Chemistry* 93 (3): 1643–1651. https://doi.org/10.1021/acs.analchem.0c04225.

Nelson, G. L., A. M. Lines, J. M. Bello, and S. A. Bryan. 2019a. "Online Monitoring of Solutions Within Microfluidic Chips: Simultaneous Raman and UV-Vis Absorption Spectroscopies." *Acs Sensors* 4 (9): 2288–2295. https://doi.org/10.1021/acssensors.9b00736.

Nelson, Gilbert L., Amanda M. Lines, Job M. Bello, and Samuel A. Bryan. 2019b. "Online Monitoring of Solutions Within Microfluidic Chips: Simultaneous Raman and UV–Vis Absorption Spectroscopies." *ACS Sensors* 4 (9): 2288–2295. https://doi.org/10.1021/acssensors.9b00736.

Nelson, Gilbert L., Amanda M. Lines, Amanda J. Casella, Job M. Bello, and Samuel A. Bryan. 2018. "Development and testing of a novel micro-Raman probe and application of calibration method for the quantitative analysis of microfluidic nitric acid streams." *Analyst* 143 (5): 1188–1196. https://doi.org/10.1039/C7AN01761H. http://dx.doi.org/10.1039/C7AN01761H.

Parastar, Hadi, and Dmitry Kirsanov. 2020. "Analytical Figures of Merit for Multisensor Arrays." *ACS Sensors* 5 (2): 580–587. https://doi.org/10.1021/acssensors.9b02531.

Schroll, C. A., S. Chatterjee, T. G. Levitskaia, W. R. Heineman, and S. A. Bryan. 2013. "Electrochemistry and Spectroelectrochemistry of Europium(III) Chloride in 3LiCl-2KCl from 643 to 1123 K." *Analytical Chemistry* 85 (20): 9924–9931. https://doi.org/10.1021/ac402518p. <Go to ISI>://WOS:000326126600070.

Schroll, C. A., A. M. Lines, W. R. Heineman, and S. A. Bryan. 2016. "Absorption spectroscopy for the quantitative prediction of lanthanide concentrations in the 3LiCl-2CsCl eutectic at 723 K." *Analytical Methods* 8 (43): 7731–7738. https://doi.org/10.1039/c6ay01520d. <Go to ISI>://WOS:000387989200002.

Serrano, Thomas, Alyssa F. Espley, Savannah M. Potter, Kenneth A. Ross, PoKi Tse, Nathan P. Bessen, Heather M. Felmy, Hope E. Lackey, Jarrod R. Allred, Brienne N. Seiner, Gregg J. Lumetta, Gilbert L. Nelson, Samuel A. Bryan, and Amanda M. Lines. 2025. "Real-Time Automated pH Control within Batch Processes Relying on Raman pH Measurement." *ACS Omega* 10 (18): 18238–18250. https://doi.org/10.1021/acsomega.4c07963. https://doi.org/10.1021/acsomega.4c07963.

Tennøe, Simen, Geir Halnes, and Gaute T. Einevoll. 2018. "Uncertainpy: A Python Toolbox for Uncertainty Quantification and Sensitivity Analysis in Computational Neuroscience." *Frontiers in Neuroinformatics*.

Tse, Poki, Nathan P. Bessen, Alyssa F. Espley, Heather M. Felmy, Hope E. Lackey, Roberta R. Rodrigues, Aditya H. Parekh, Savannah M. Potter, Gilbert L. Nelson, Jarrod R. Allred, Gabriel B. Hall, Brienne N. Seiner, Gregg J. Lumetta, Samuel A. Bryan, and Amanda M. Lines. 2025. "Spectroscopic Online Monitoring: Using a Multi-Track Visible Spectrometer to Facilitate a Mass Balance Study in a Simulated TALSPEAK Process." *ACS Omega* 10 (12): 11796–11805. https://doi.org/10.1021/acsomega.4c07704. https://doi.org/10.1021/acsomega.4c07704.

Tse, Poki, Nathan P. Bessen, Gabriel B. Hall, Brienne N. Seiner, Gregg J. Lumetta, Samuel A. Bryan, and Amanda M. Lines. 2024. "A Review of Online Monitoring within Used Nuclear Fuel Recycling Processes." *Solvent Extraction and Ion Exchange* 42 (5): 347–380. https://doi.org/10.1080/07366299.2024.2395917.

Tse, Poki, Jenifer Shafer, Samuel A. Bryan, Gilbert L. Nelson, and Amanda M. Lines. 2022. "Measuring Nd(III) Solution Concentration in the Presence of Interfering Er(III) and Cu(II) Ions: A Partial Least Squares Analysis of Ultraviolet–Visible Spectra." *Applied Spectroscopy* 76 (2): 173–183. https://doi.org/10.1364/AS.76.000173.

Appendix A – Supplementary Optical Data

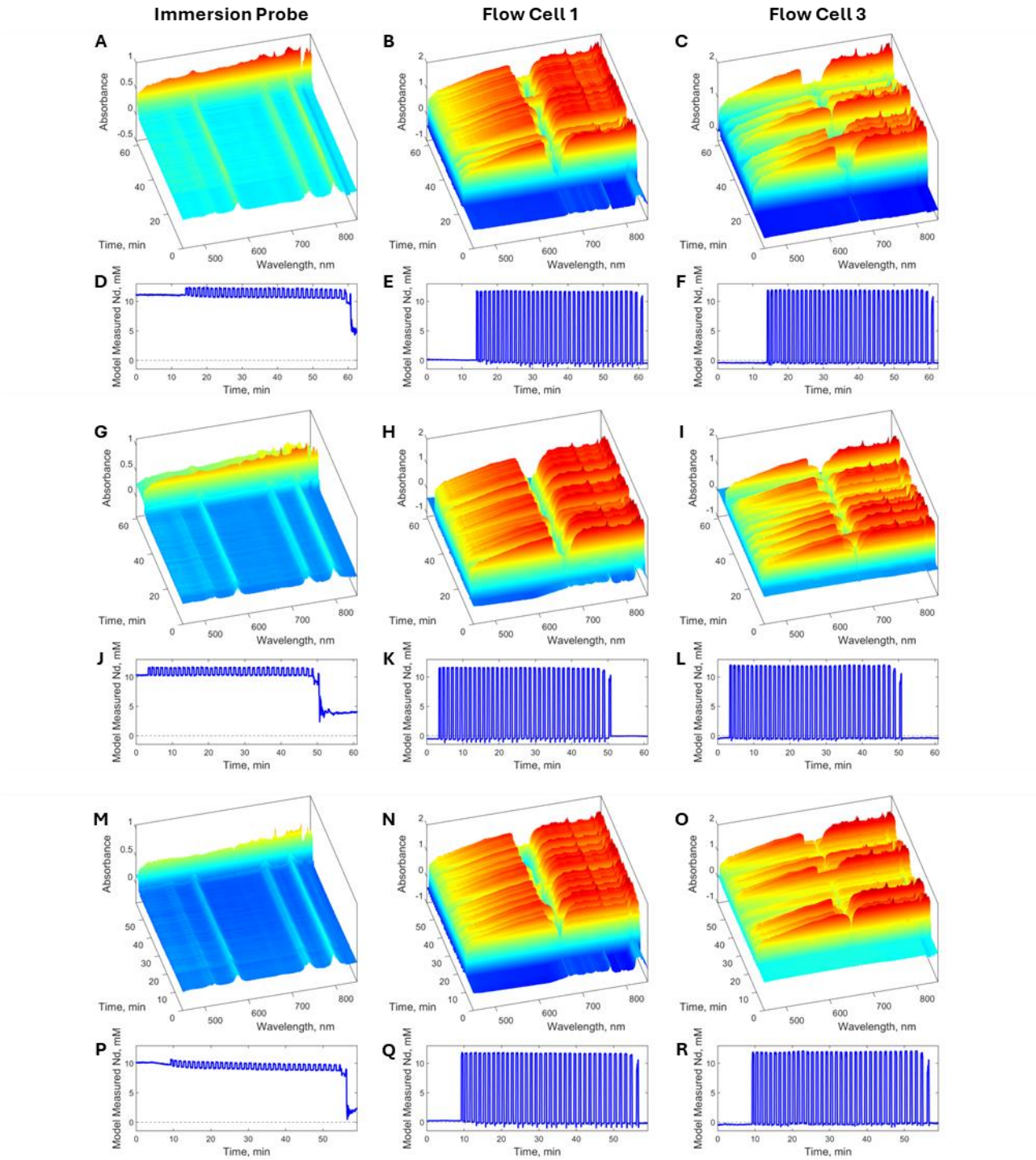


Figure 41. UV-vis Trial 1: Full tank transfer, 2.3 Bar, 3 replicates

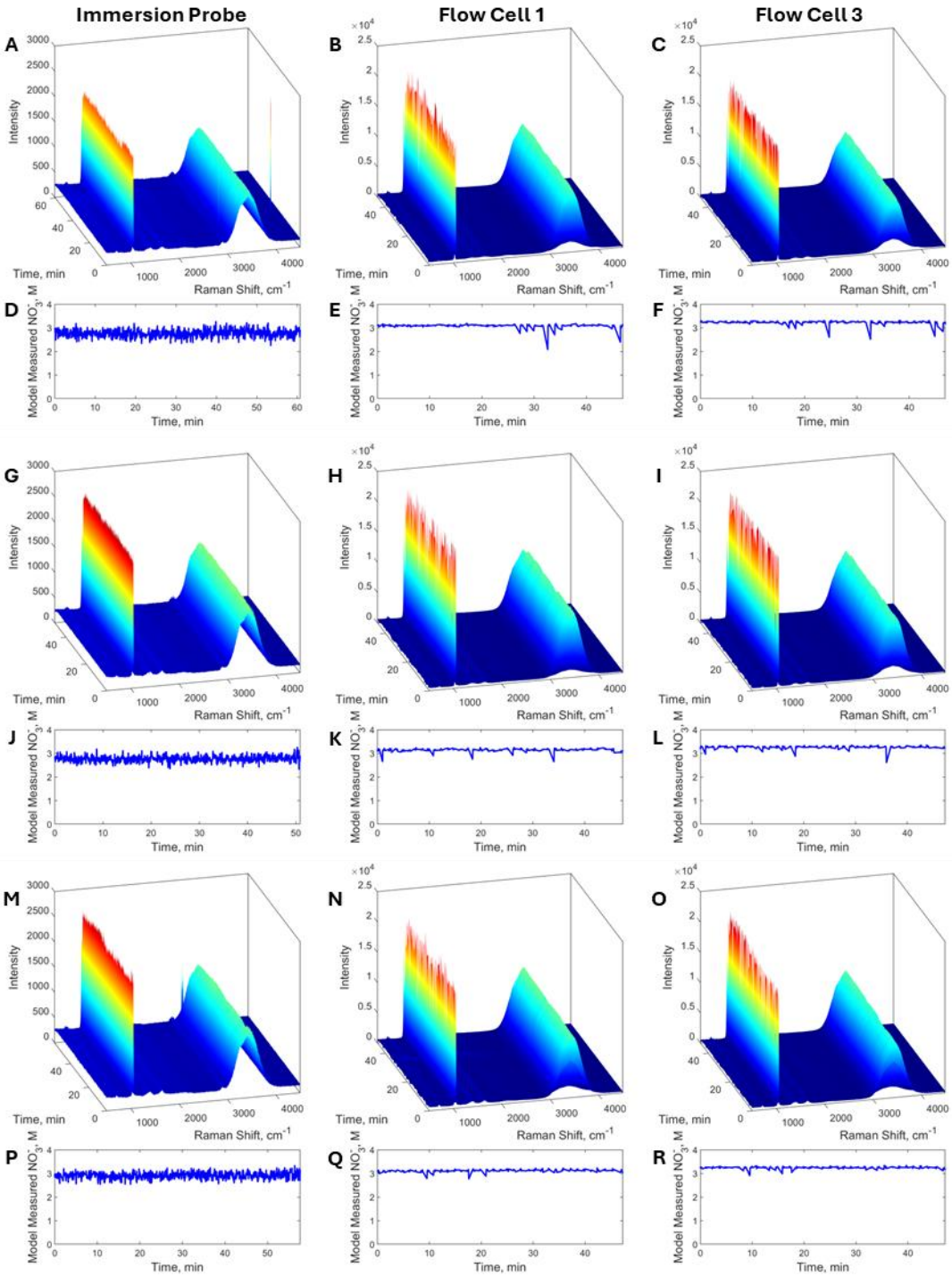


Figure 42. Raman Trial 1: Full tank transfer, 2.3 Bar, 3 replicates

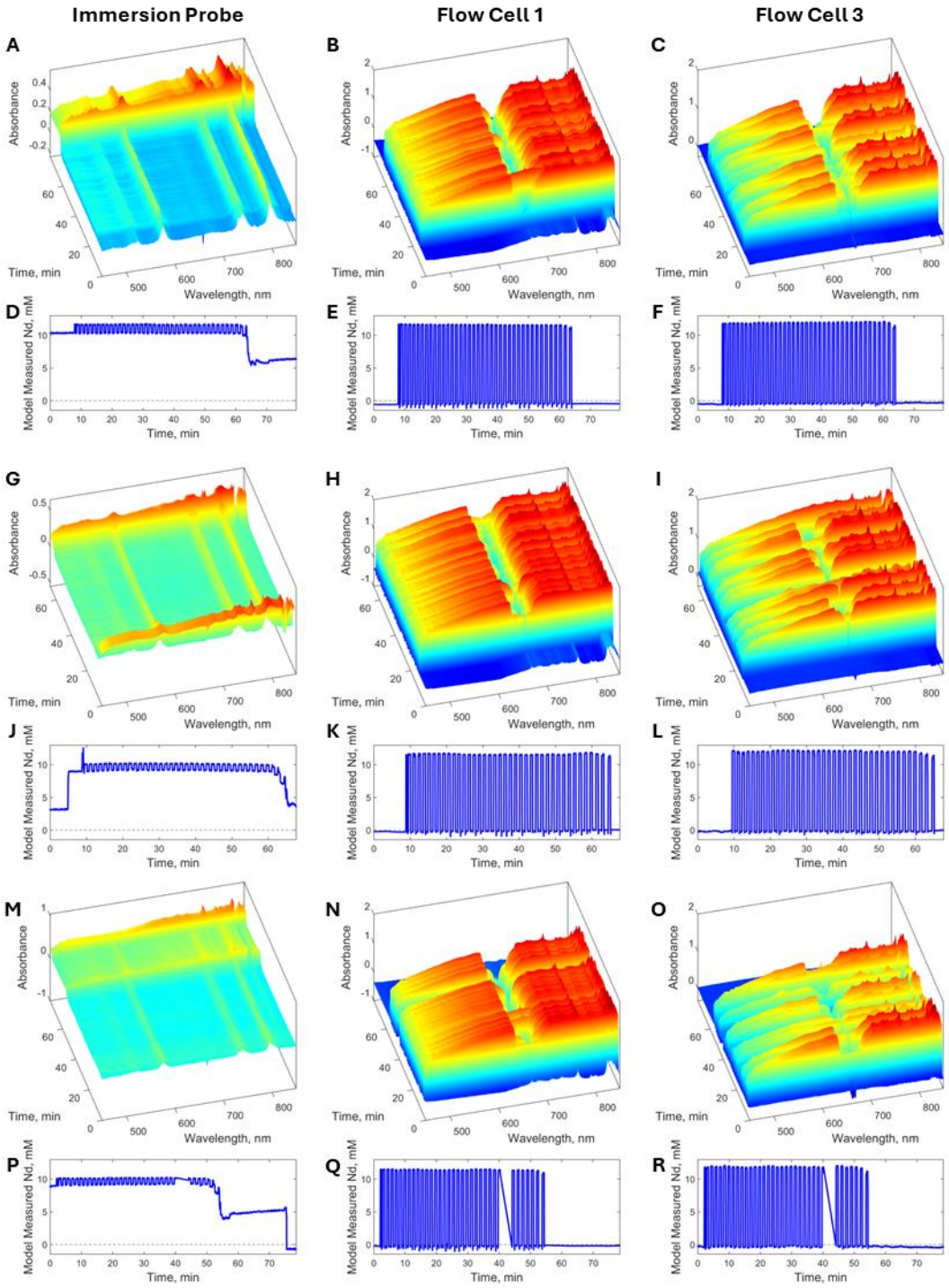


Figure 43. UV-vis Trial 2: Full tank transfer, 1.0 Bar, 3 replicates

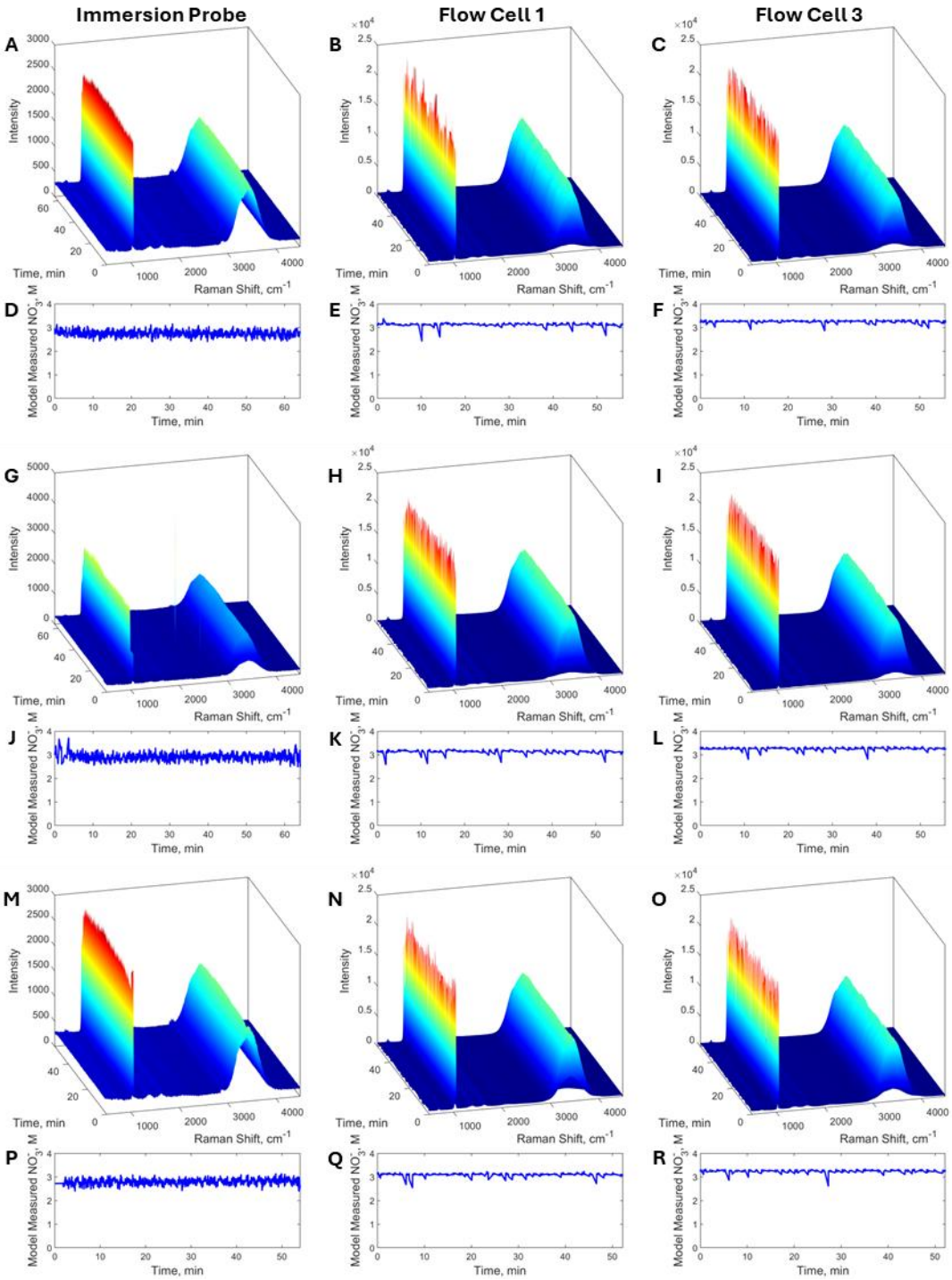


Figure 44. Raman Trial 2: Full tank transfer, 1.0 Bar, 3 replicates

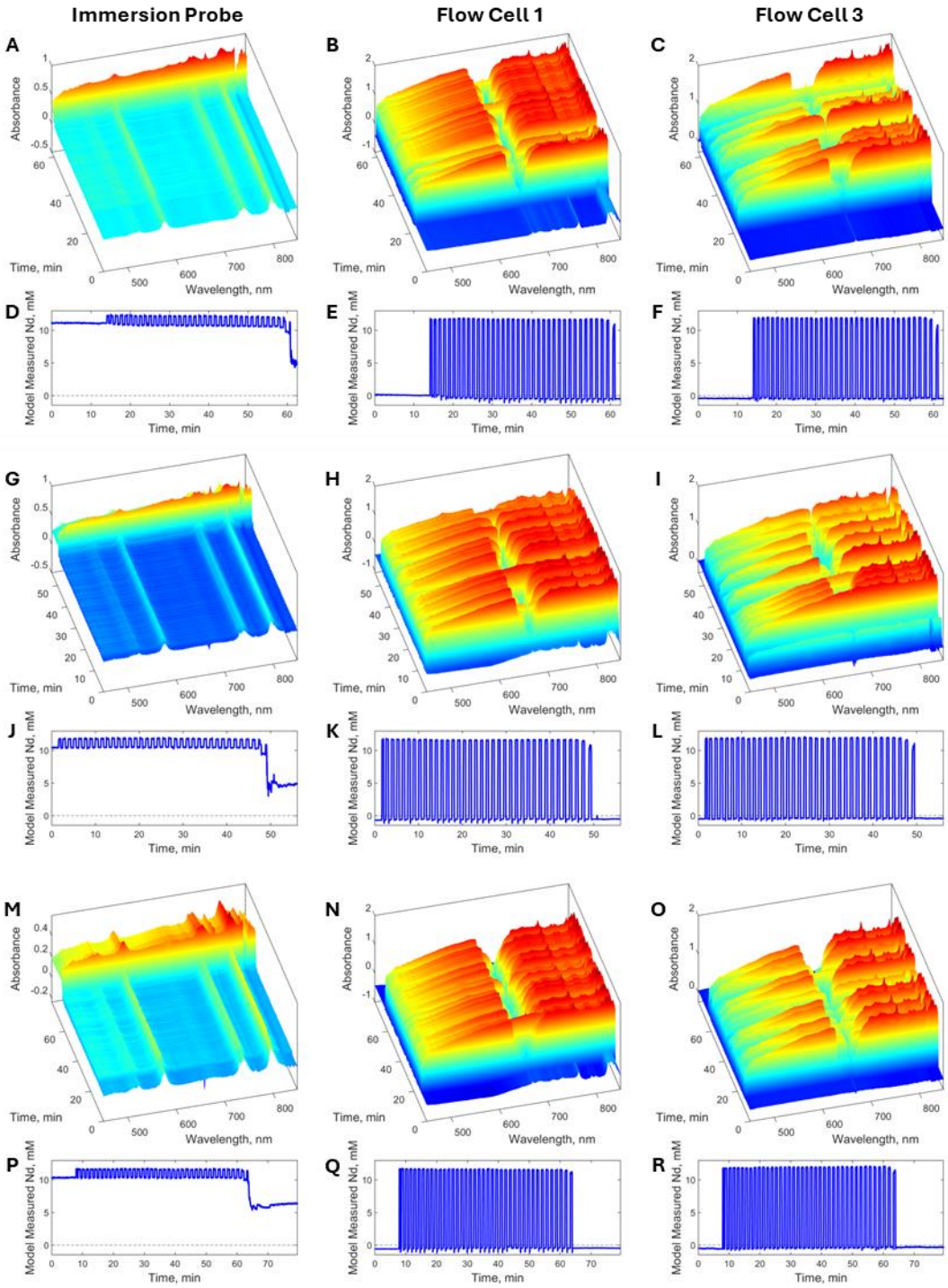


Figure 45. UV-vis Trial 3: Full tank transfer, 2.3 Bar, 2.0 Bar, 1.0 Bar

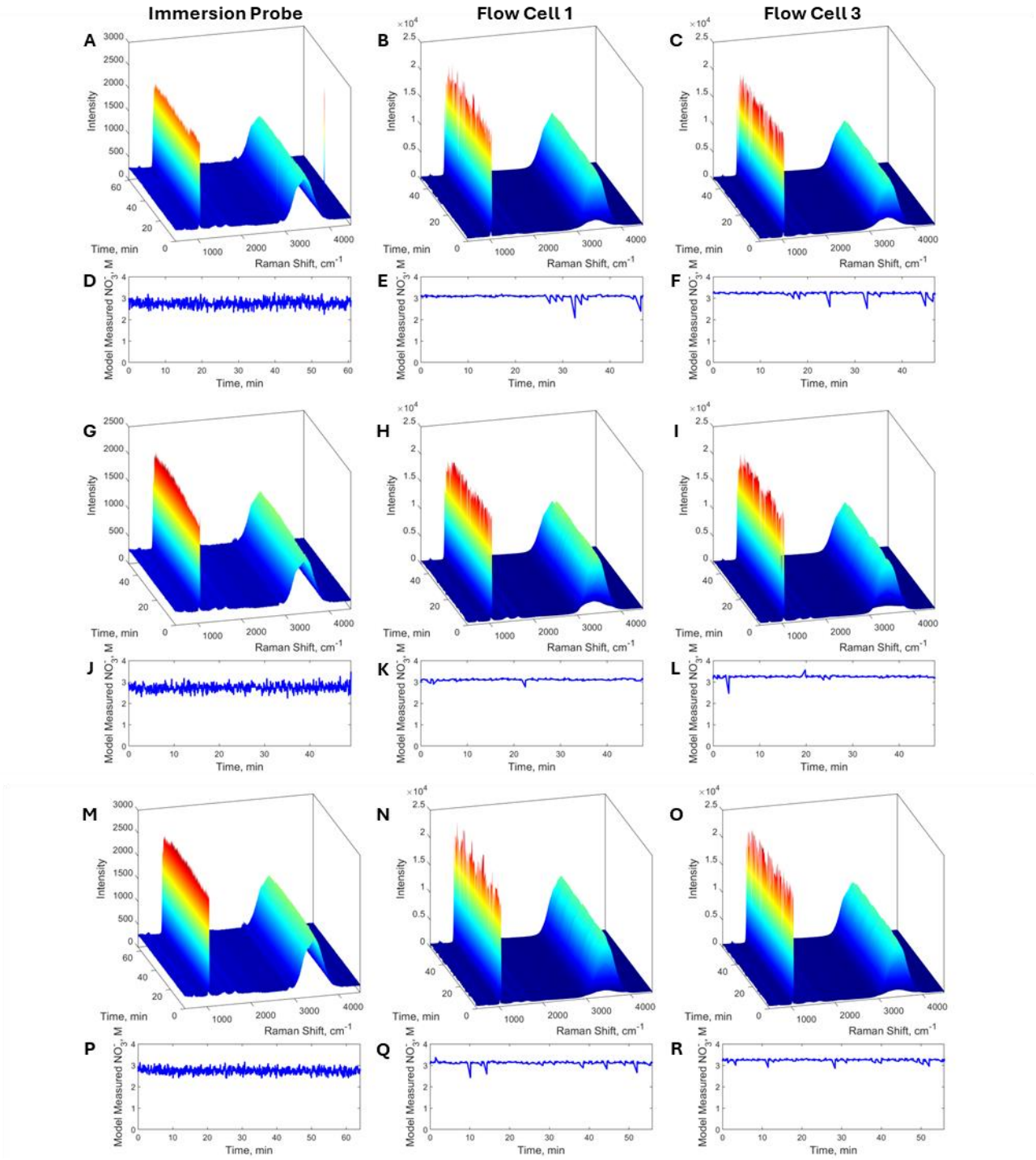


Figure 46. Raman Trial 3: Full tank transfer, 2.3 Bar, 2.0 Bar, 1.0 Bar

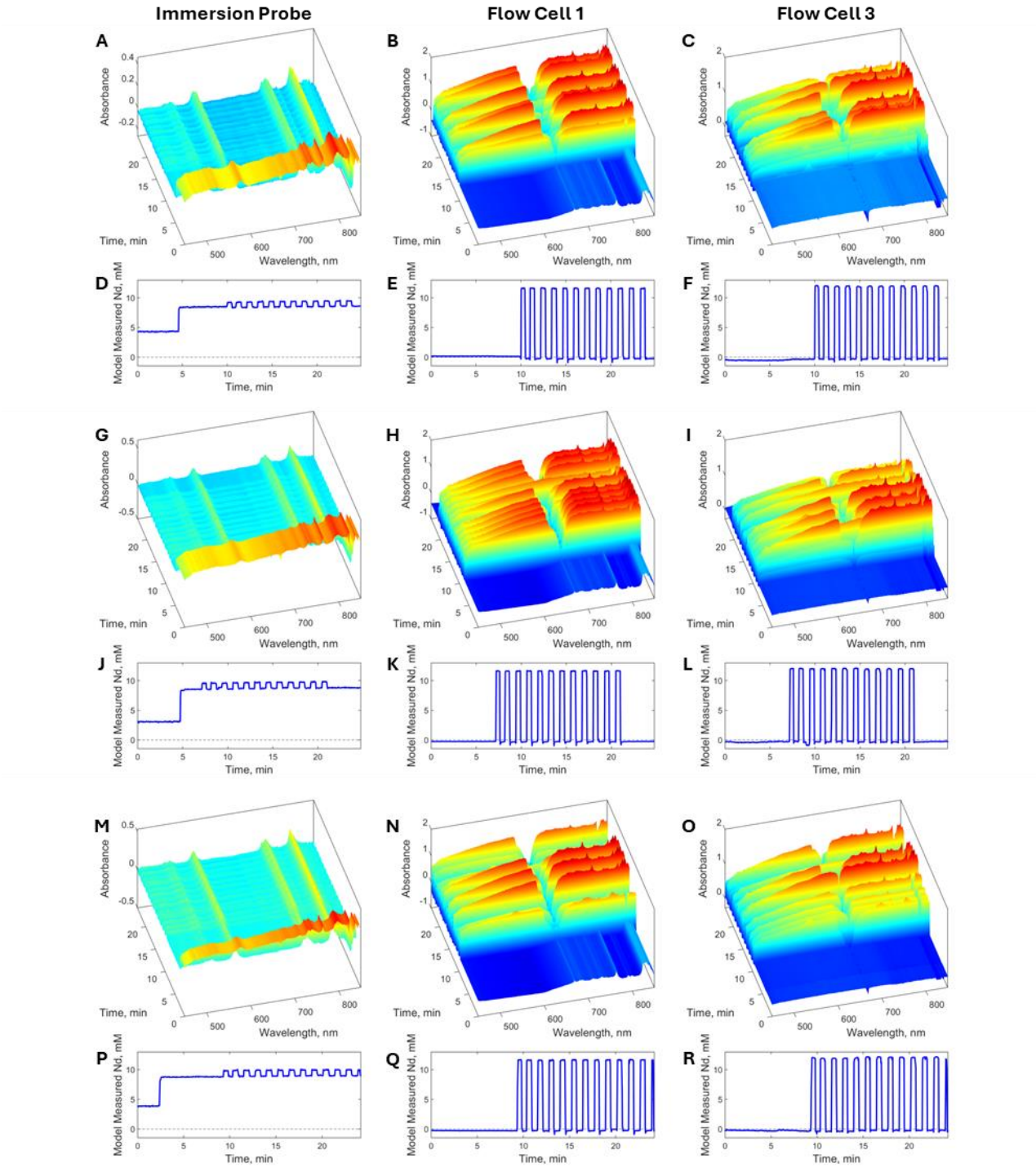


Figure 47. UV-vis Trial 4: First third tank transfer, 2.3 Bar, 2.0 Bar, 1.0 Bar

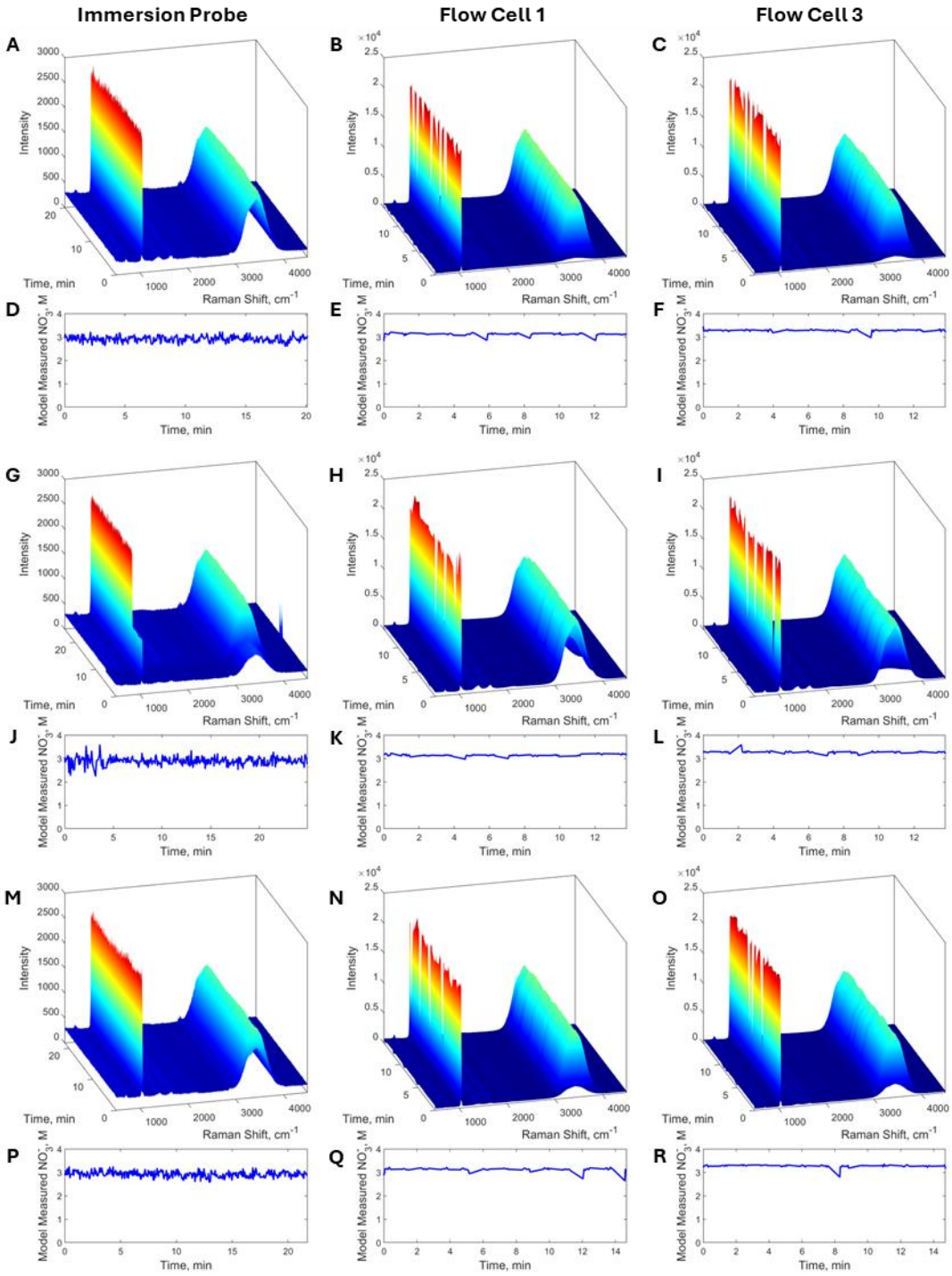


Figure 48. Raman Trial 4: First third tank transfer, 2.3 Bar, 2.0 Bar, 1.0 Bar

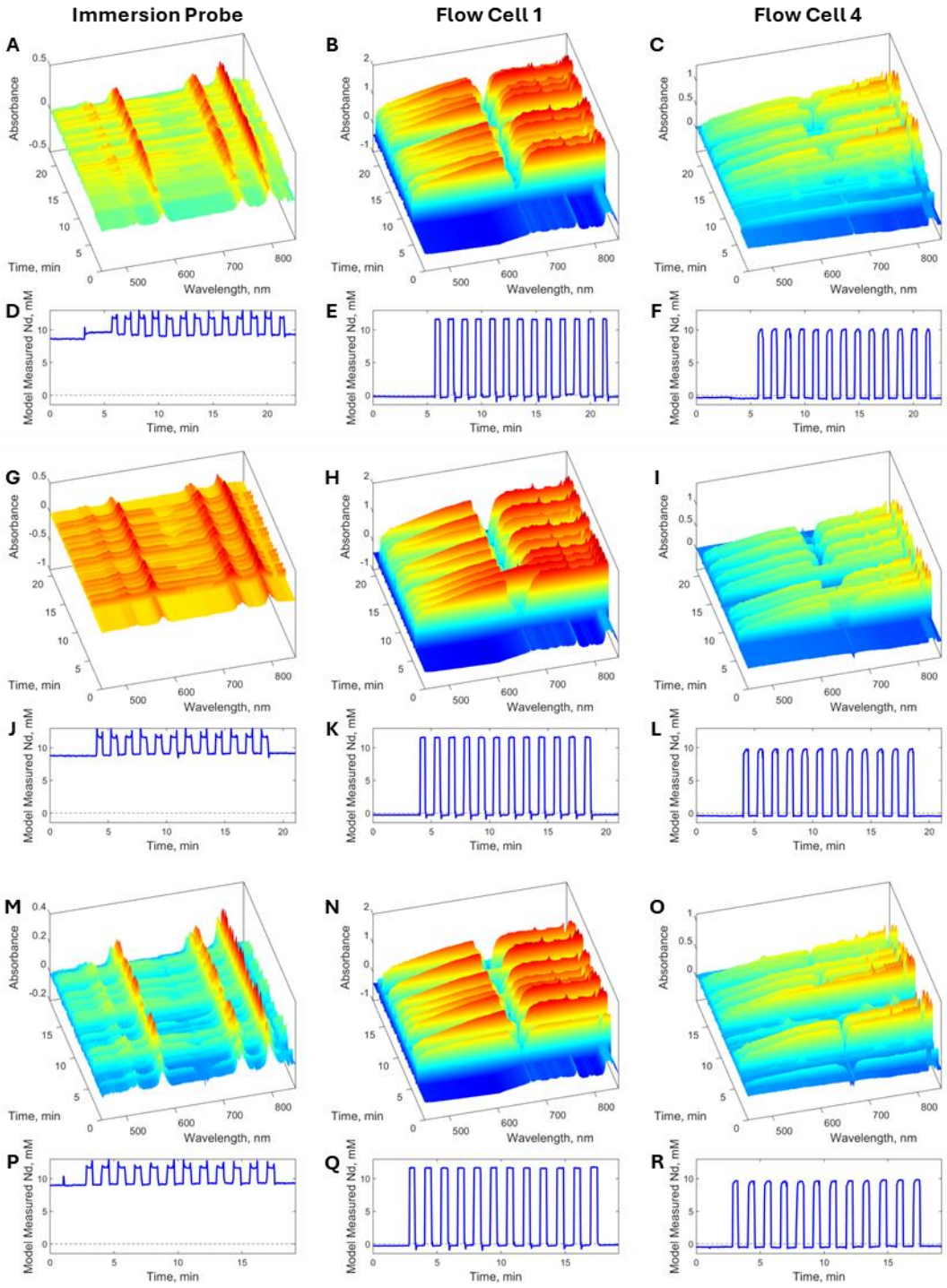


Figure 49. UV-vis Trial 5: Second third tank transfer, 2.3 Bar, 2.0 Bar, 1.0 Bar

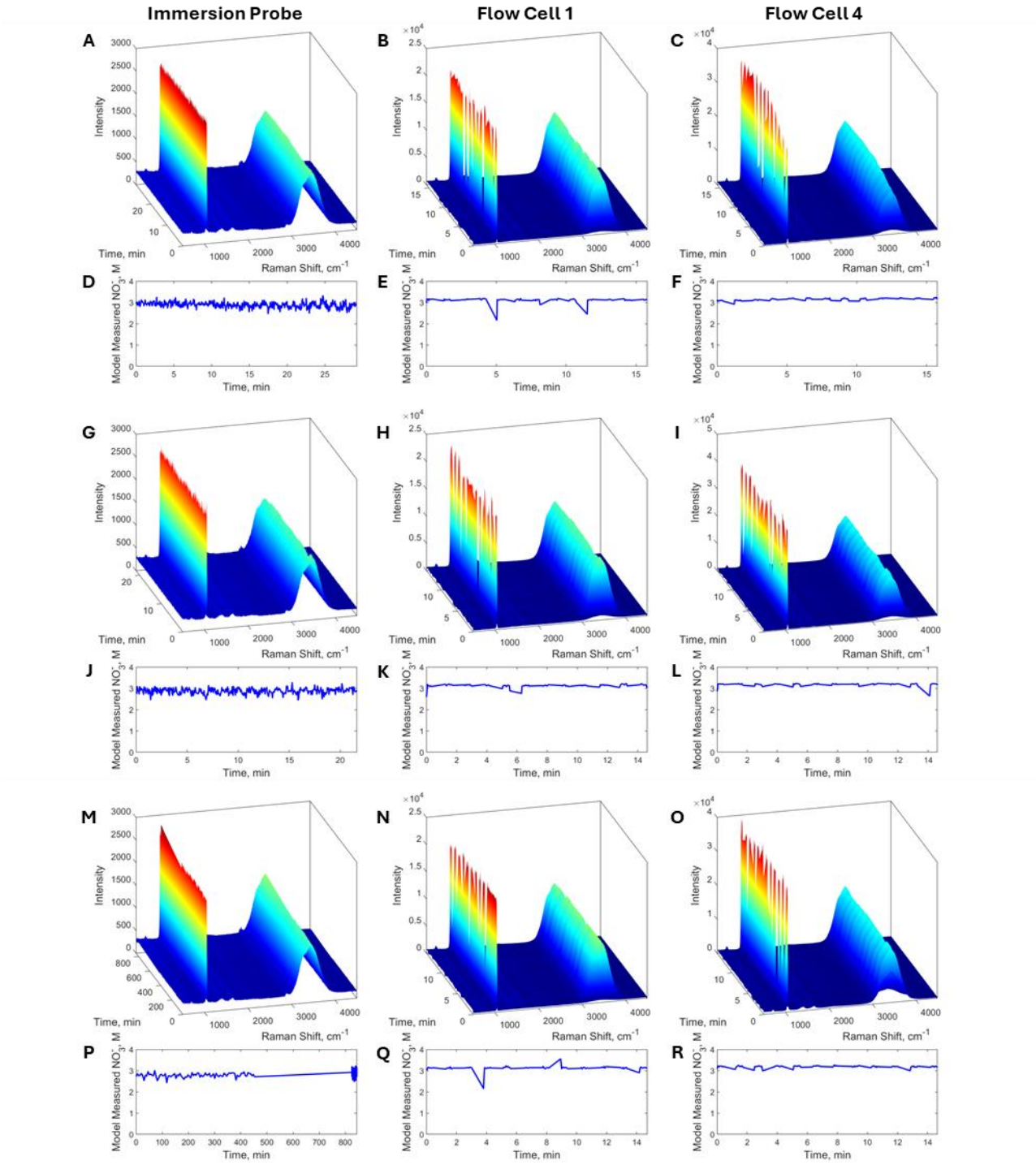


Figure 50. Raman Trial 5: Second third tank transfer, 2.3 Bar, 2.0 Bar, 1.0 Bar

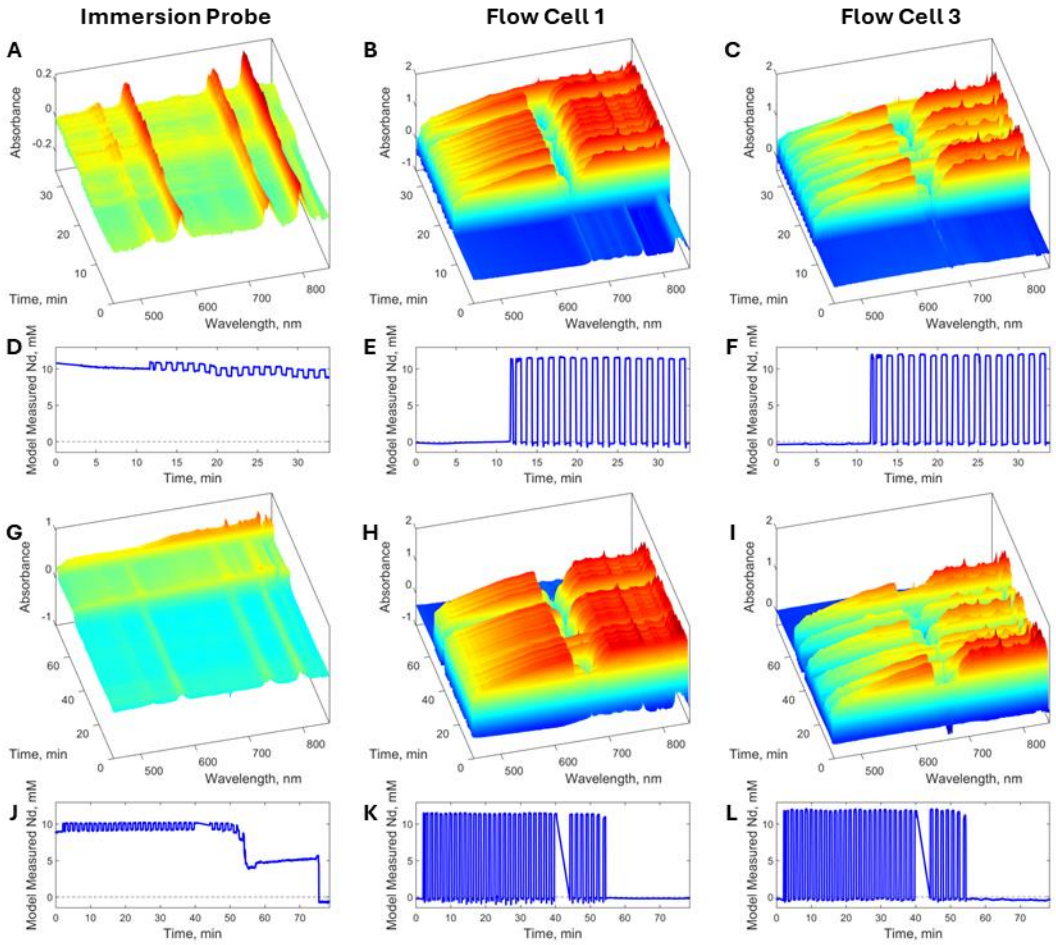


Figure 51. UV-vis Trial 6: Recirc on/off 1.0 Bar

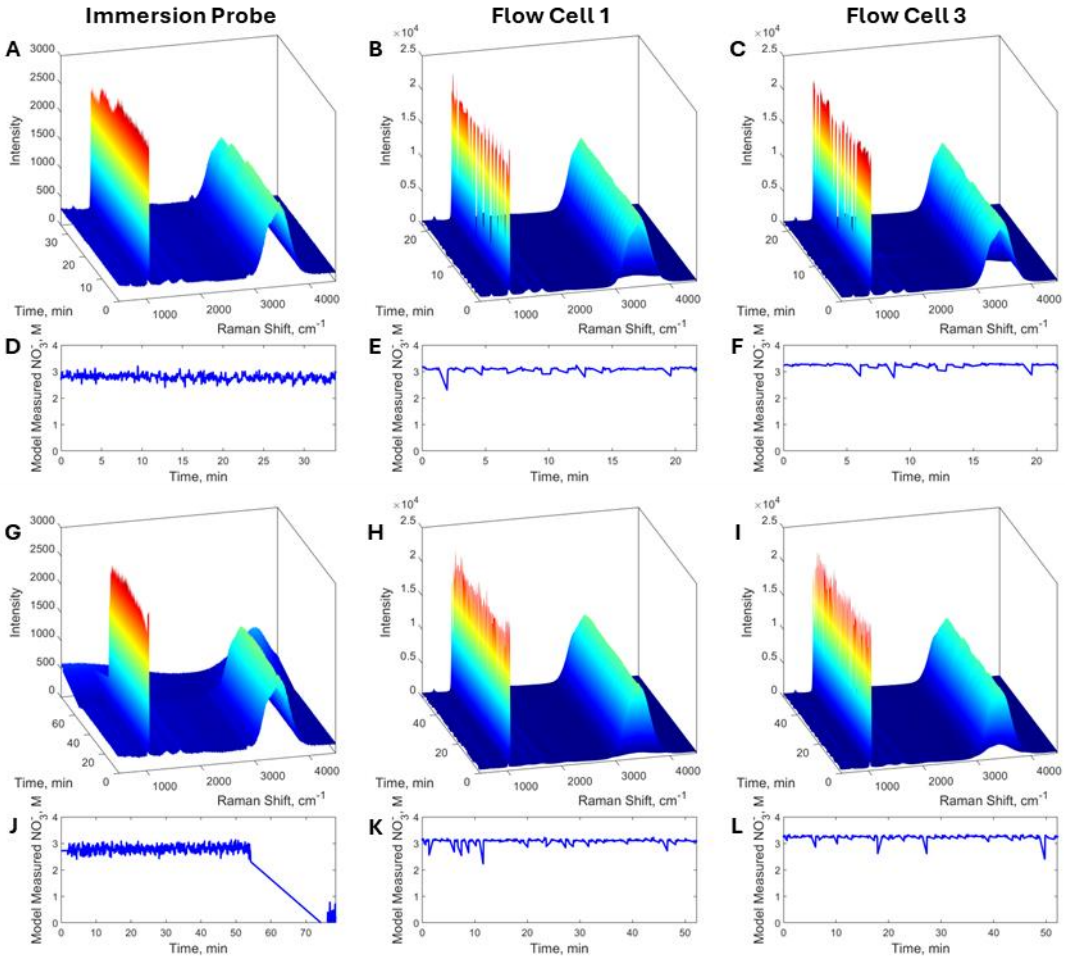


Figure 52. Raman Trial 6: Recirc on/off 1.0 Bar

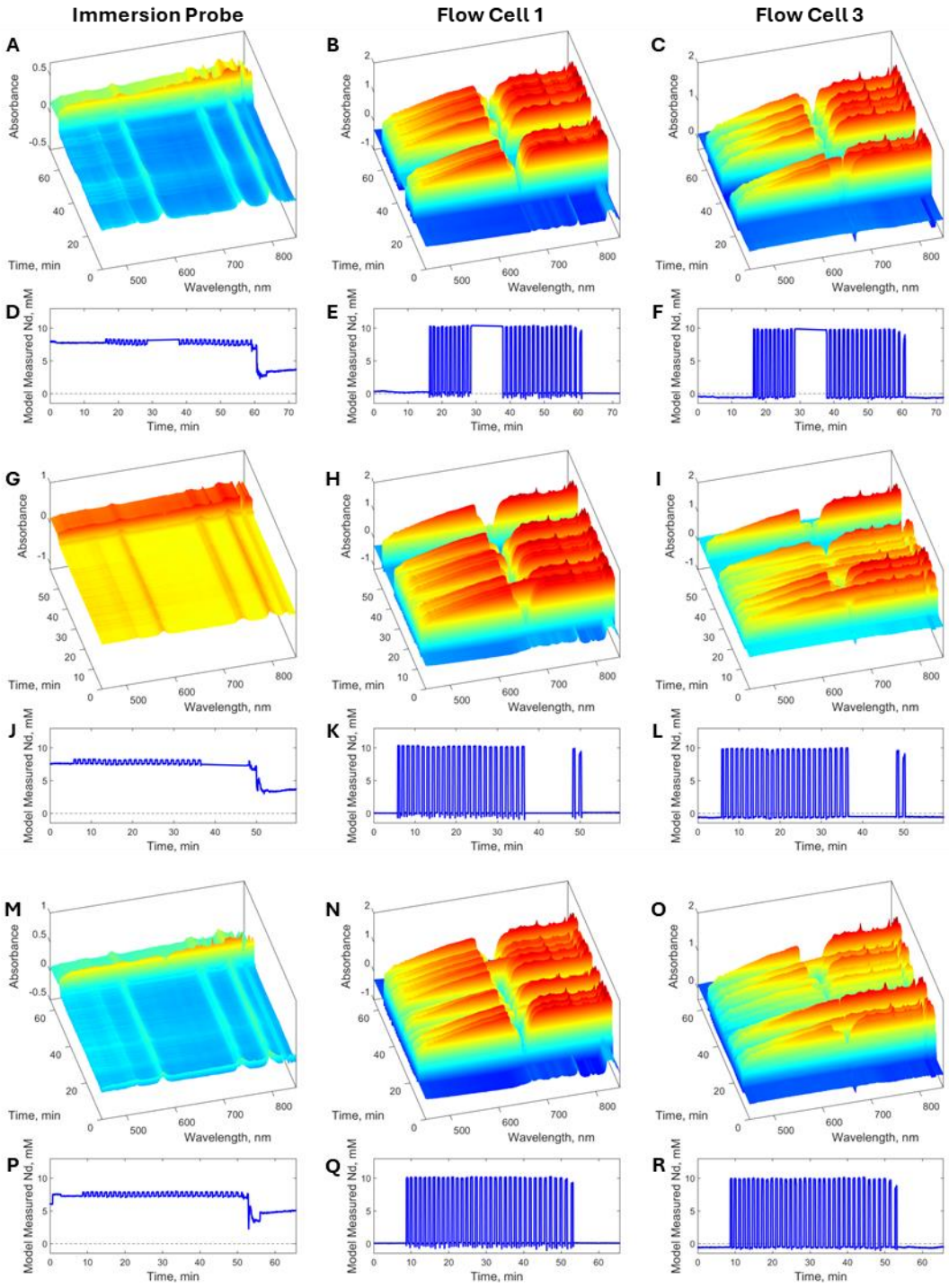


Figure 53. UV-vis Trial 7: Dilution 1, Full tank transfer, 2.3 Bar, 3 replicates

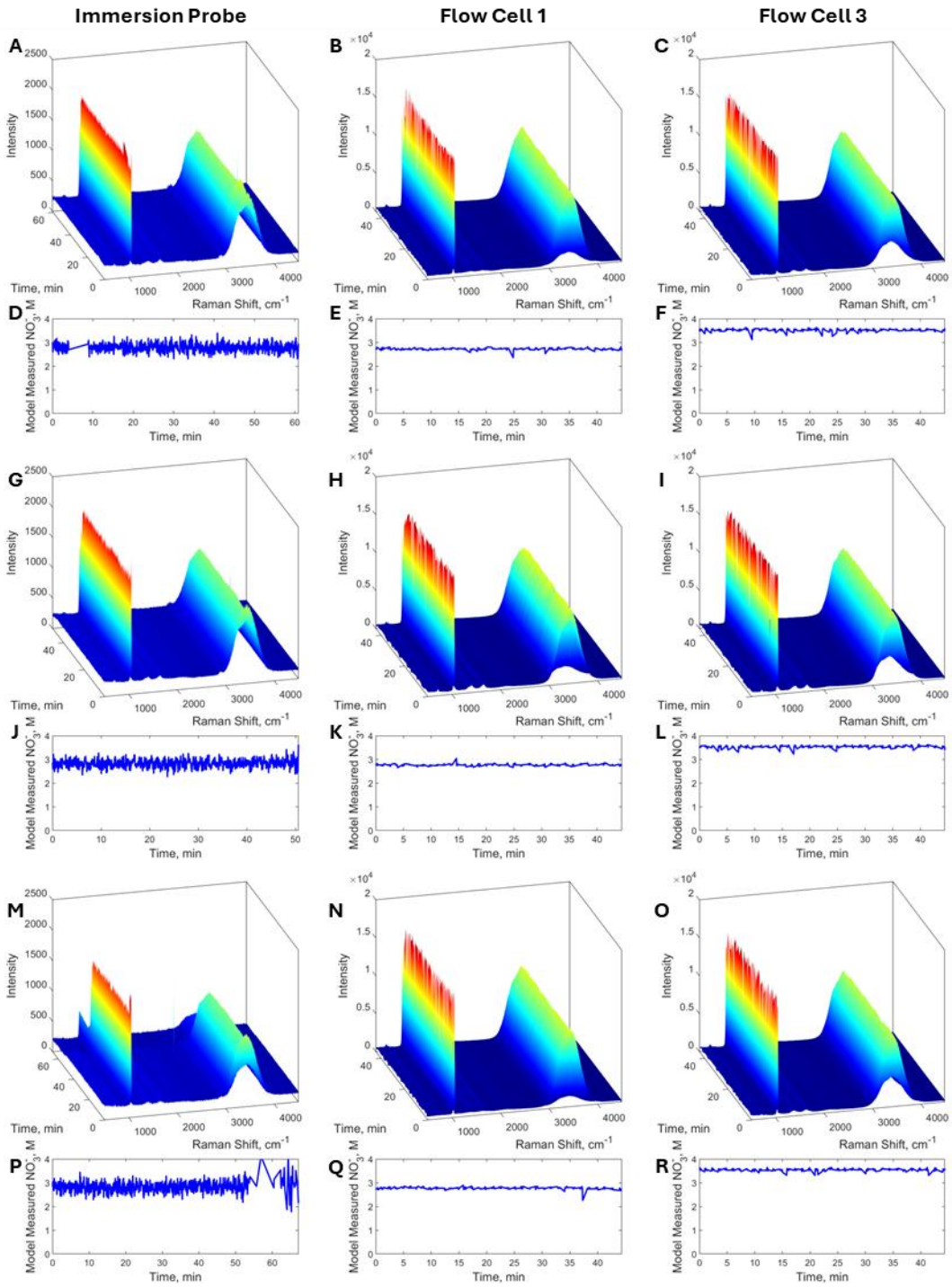


Figure 54. Raman Trial 7: Dilution 1, Full tank transfer, 2.3 Bar, 3 replicates

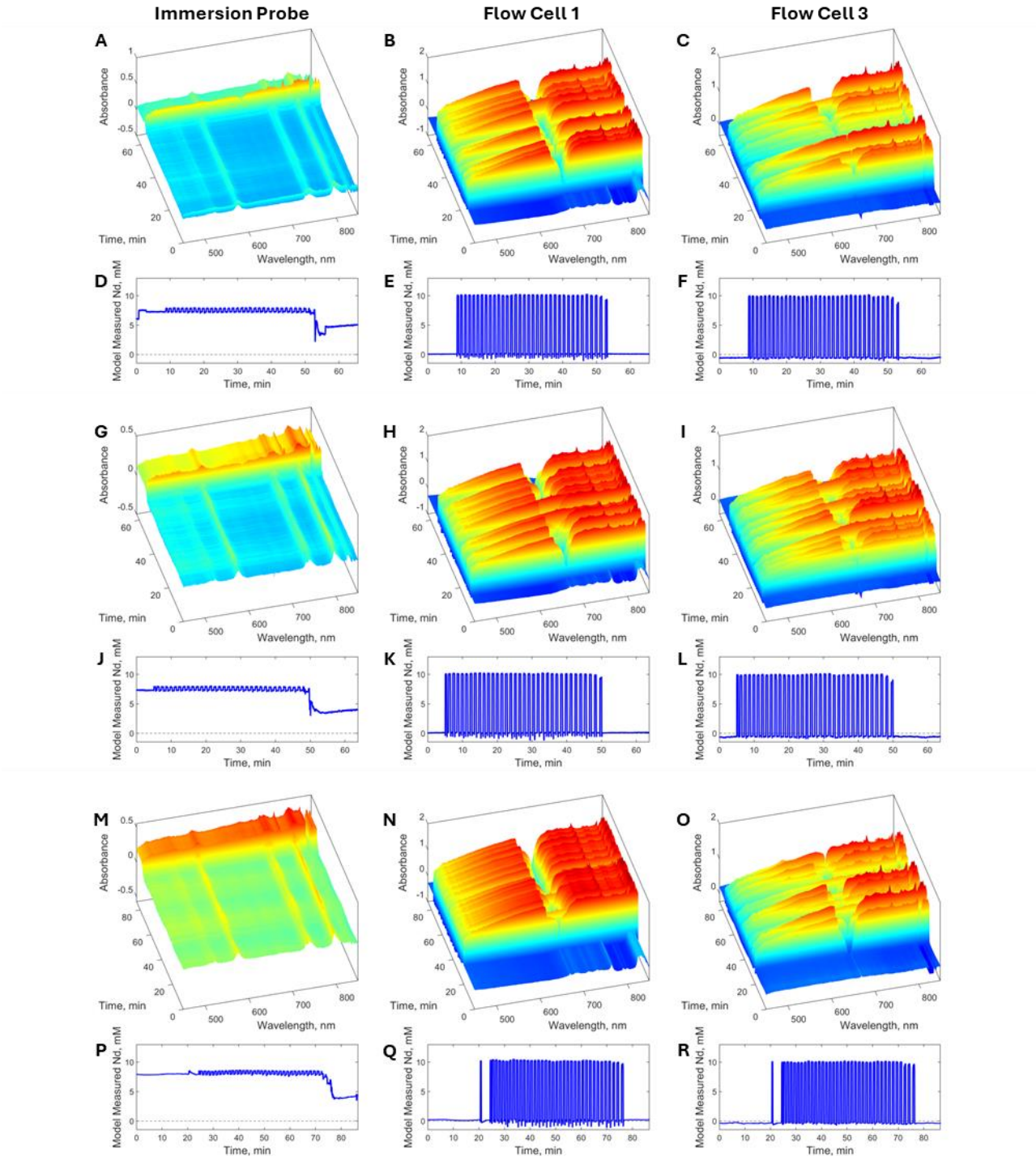


Figure 55. UV-vis Trial 8: Dilution 1, Full tank transfer, 2.3 Bar, 2.0 Bar, 1.0 Bar

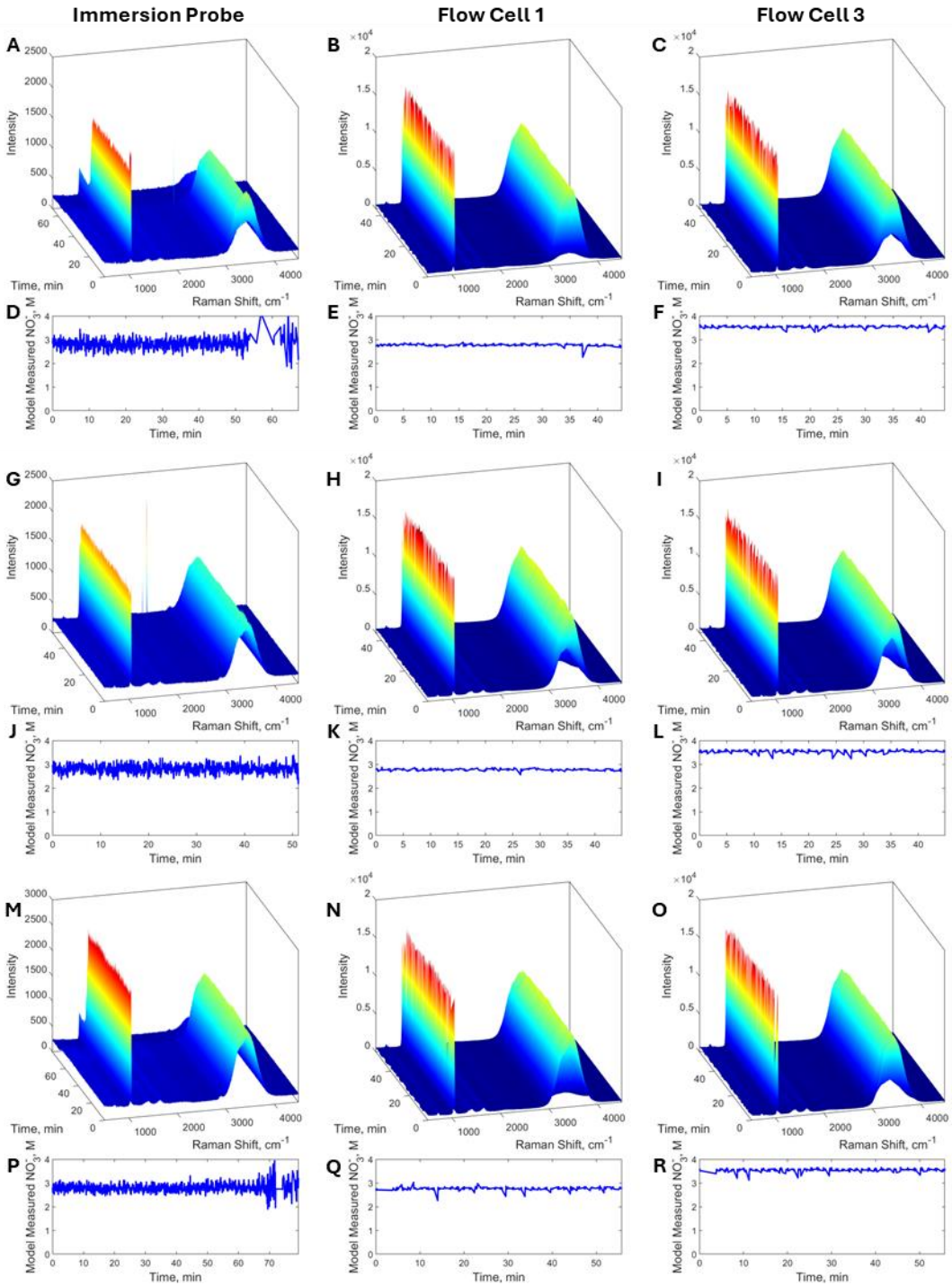


Figure 56. Raman Trial 8: Dilution 1, Full tank transfer, 2.3 Bar, 2.0 Bar, 1.0 Bar

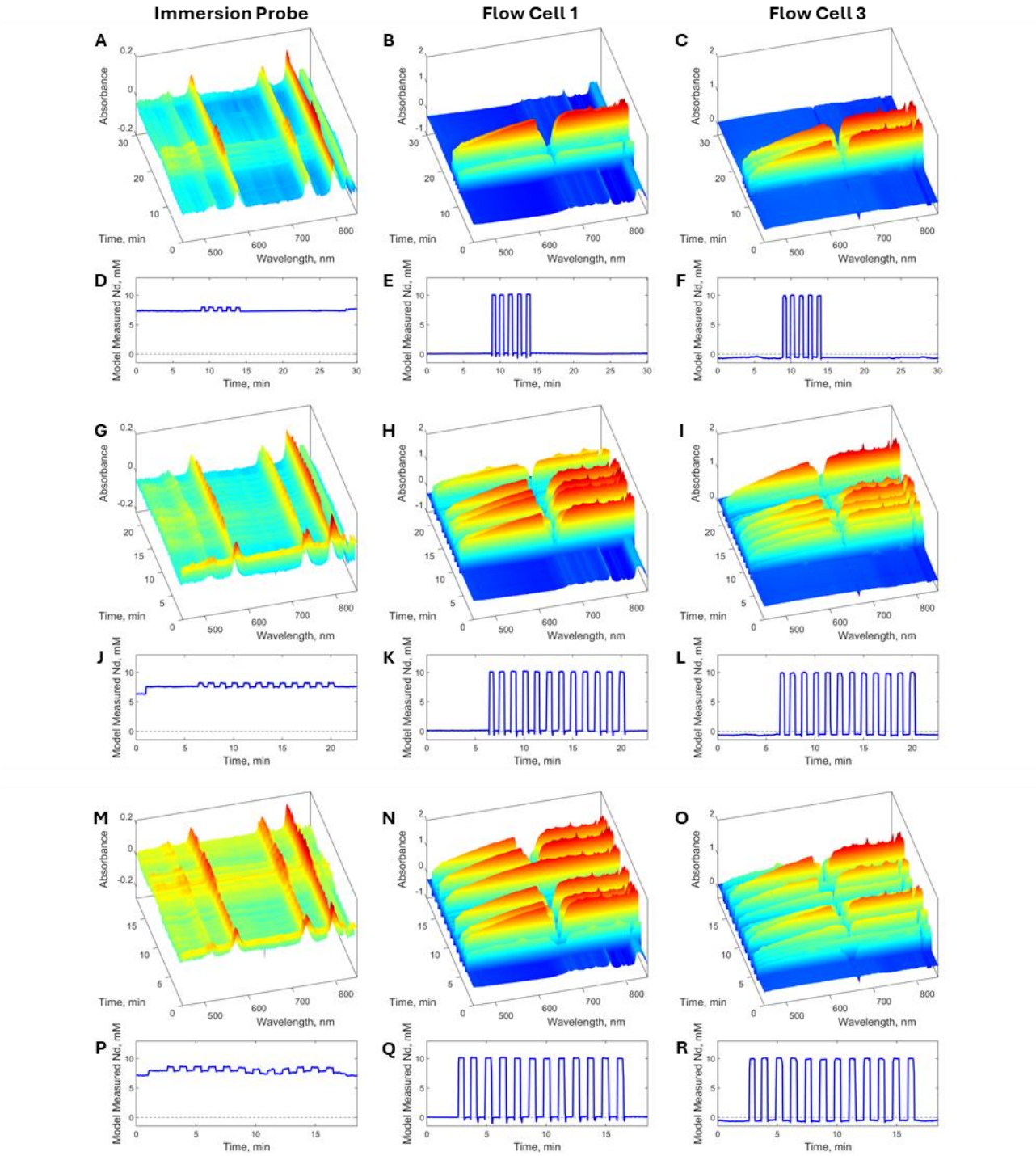


Figure 57. UV-vis Trial 9: Dilution 1, First third tank transfer, 2.3 Bar 3 replicates

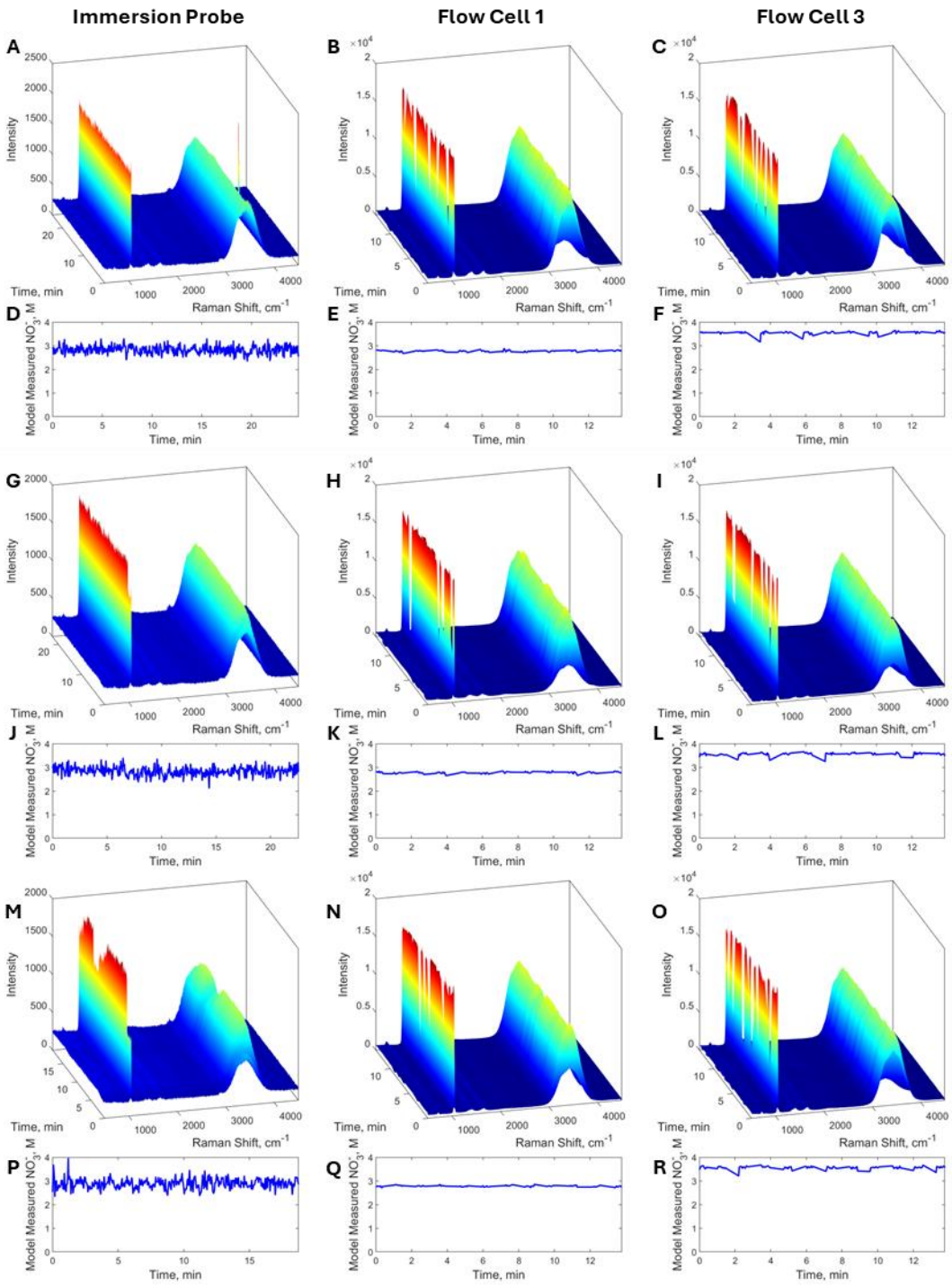


Figure 58. Raman Trial 9: Dilution 1, First third tank transfer, 2.3 Bar 3 replicates

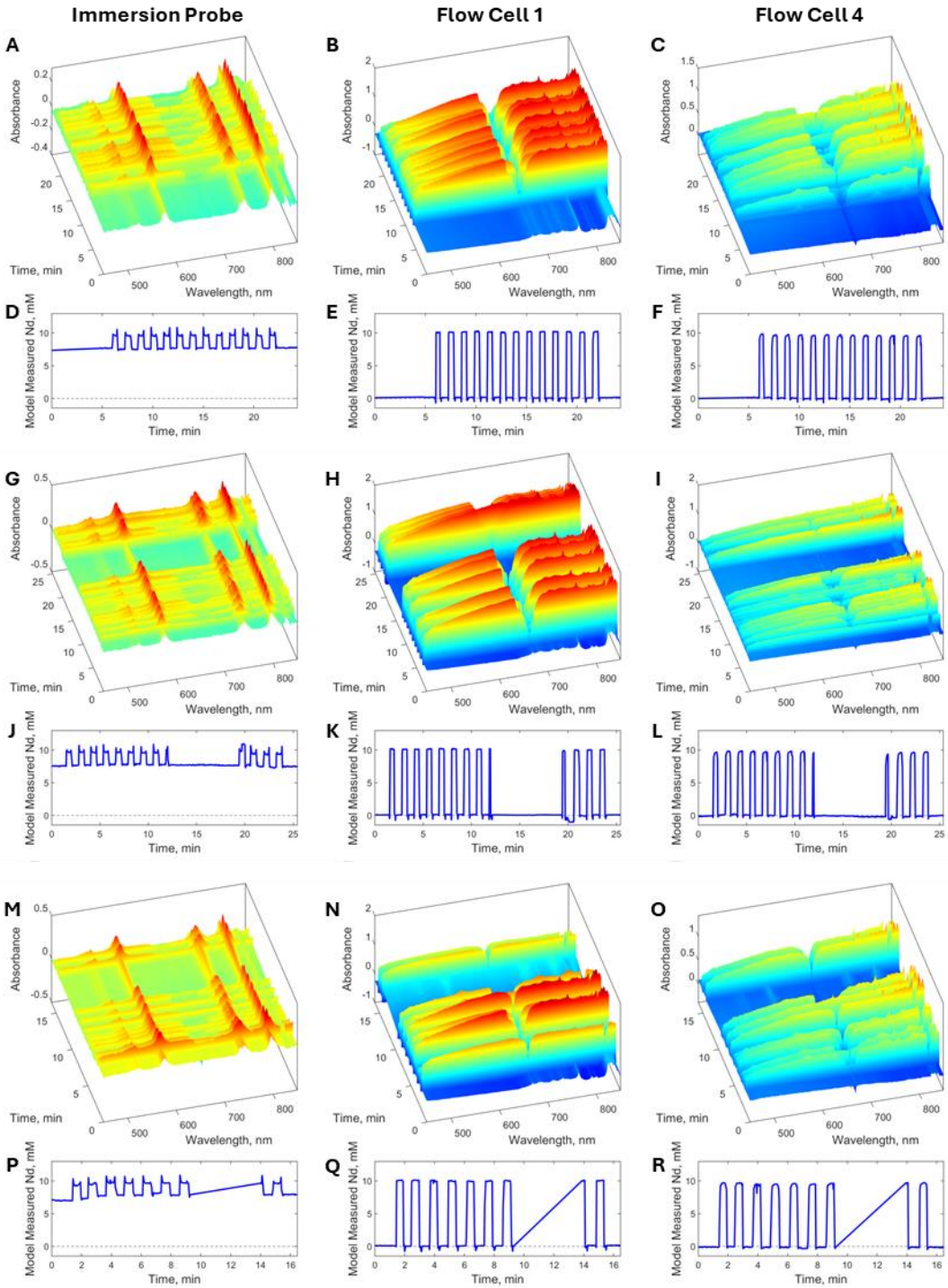


Figure 59. UV-vis Trial 10: Dilution 1, Second third tank transfer, 2.3 Bar 3 replicates

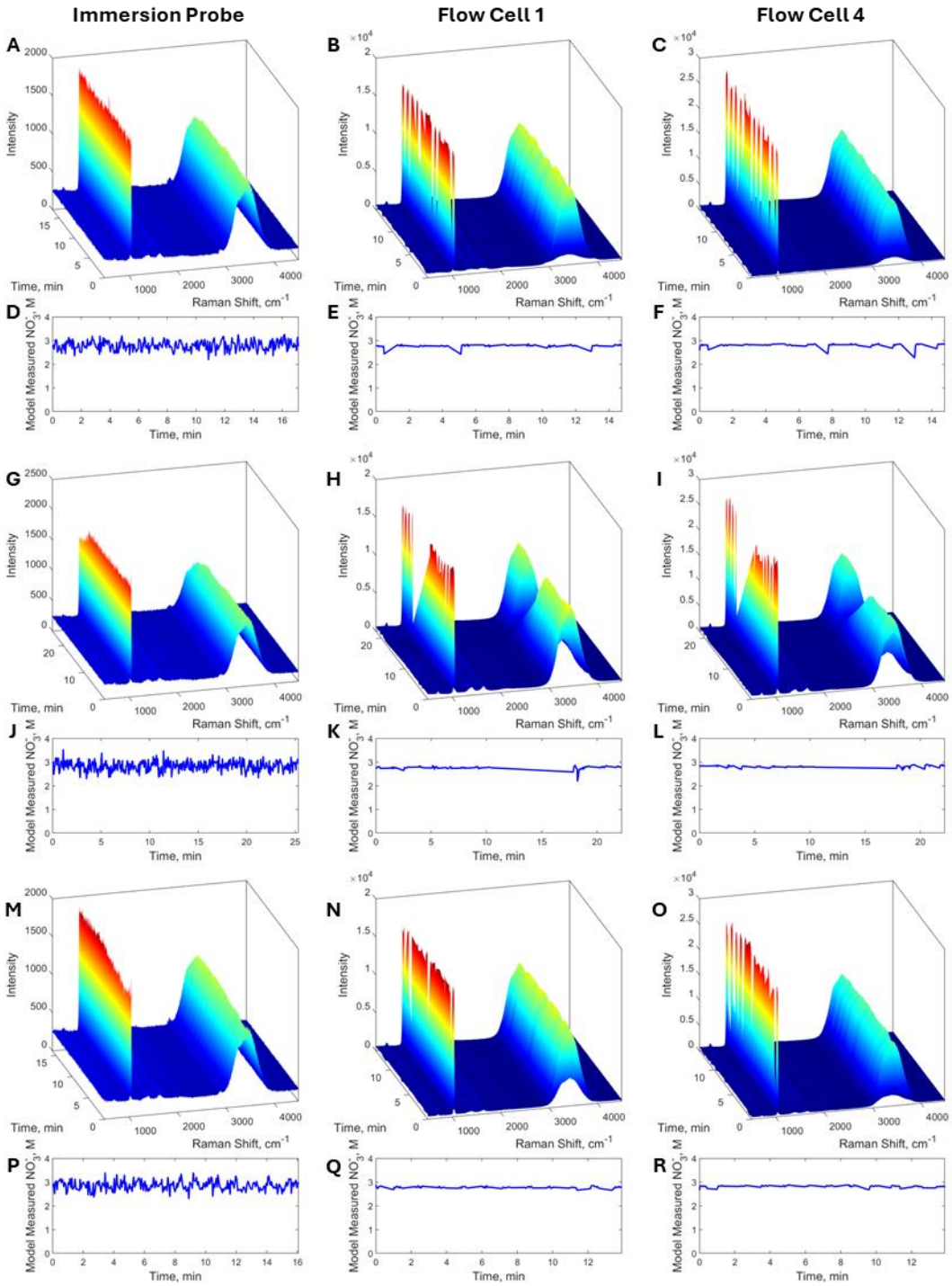


Figure 60. Raman Trial 10: Dilution 1, Second third tank transfer, 2.3 Bar 3 replicates

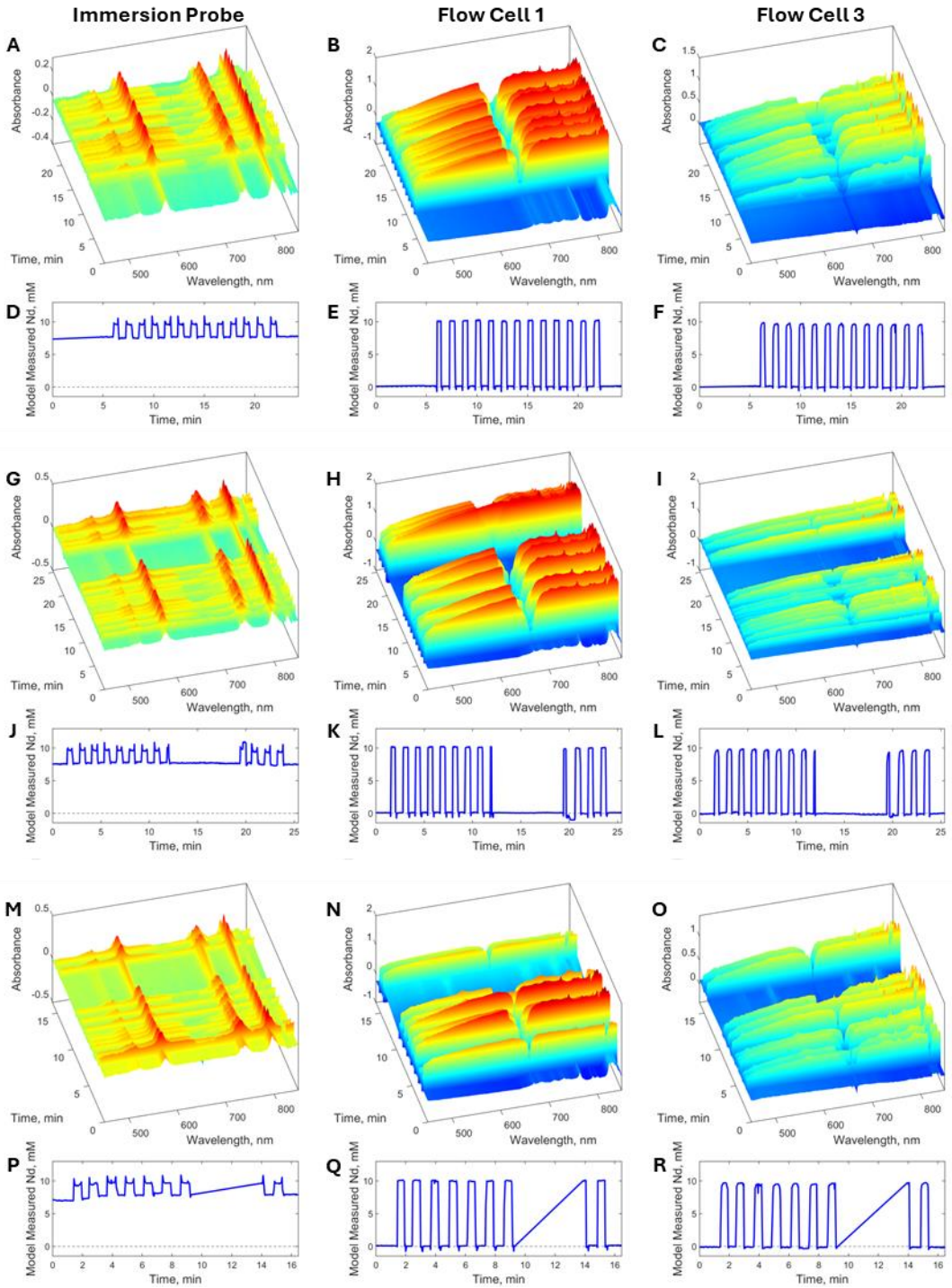


Figure 61. UV-vis Trial 11: Dilution 2, Full tank transfer, 2.3 Bar, 3 replicates

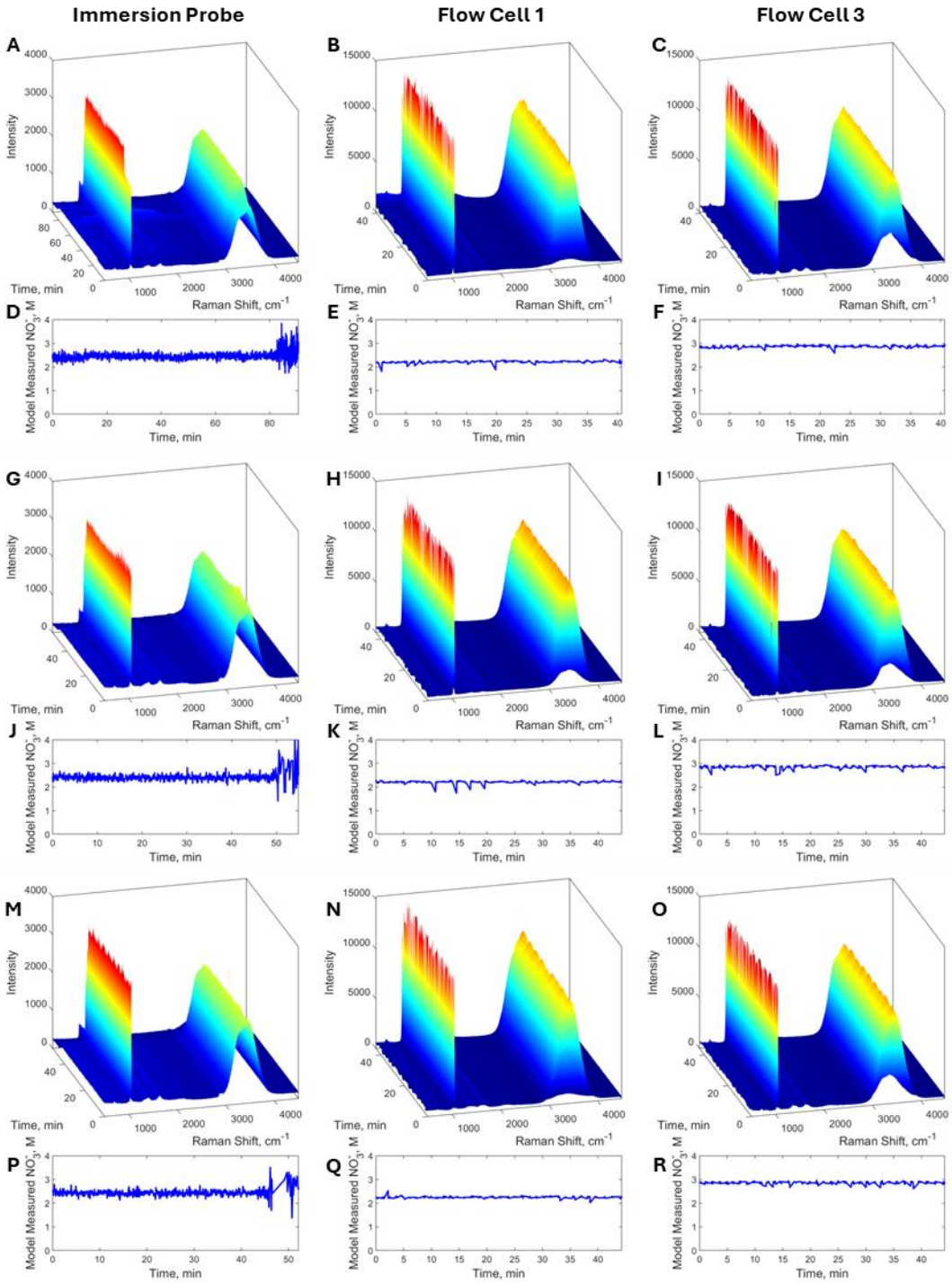


Figure 62. Raman Trial 11: Dilution 2, Full tank transfer, 2.3 Bar, 3 replicates

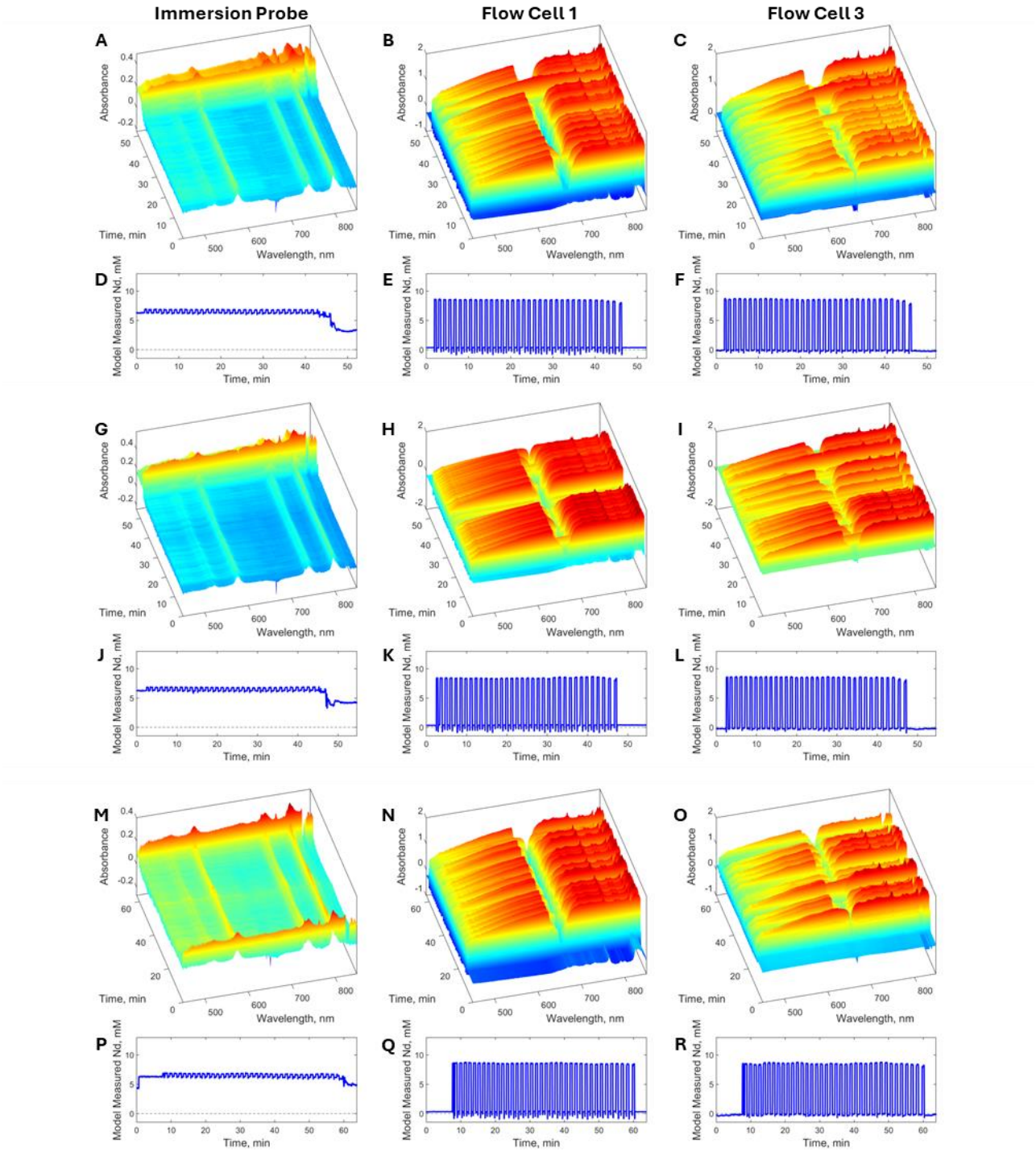


Figure 63. UV-vis Trial 12: Dilution 2, Full tank transfer, 2.3 Bar, 2.0 Bar, 1.0 Bar

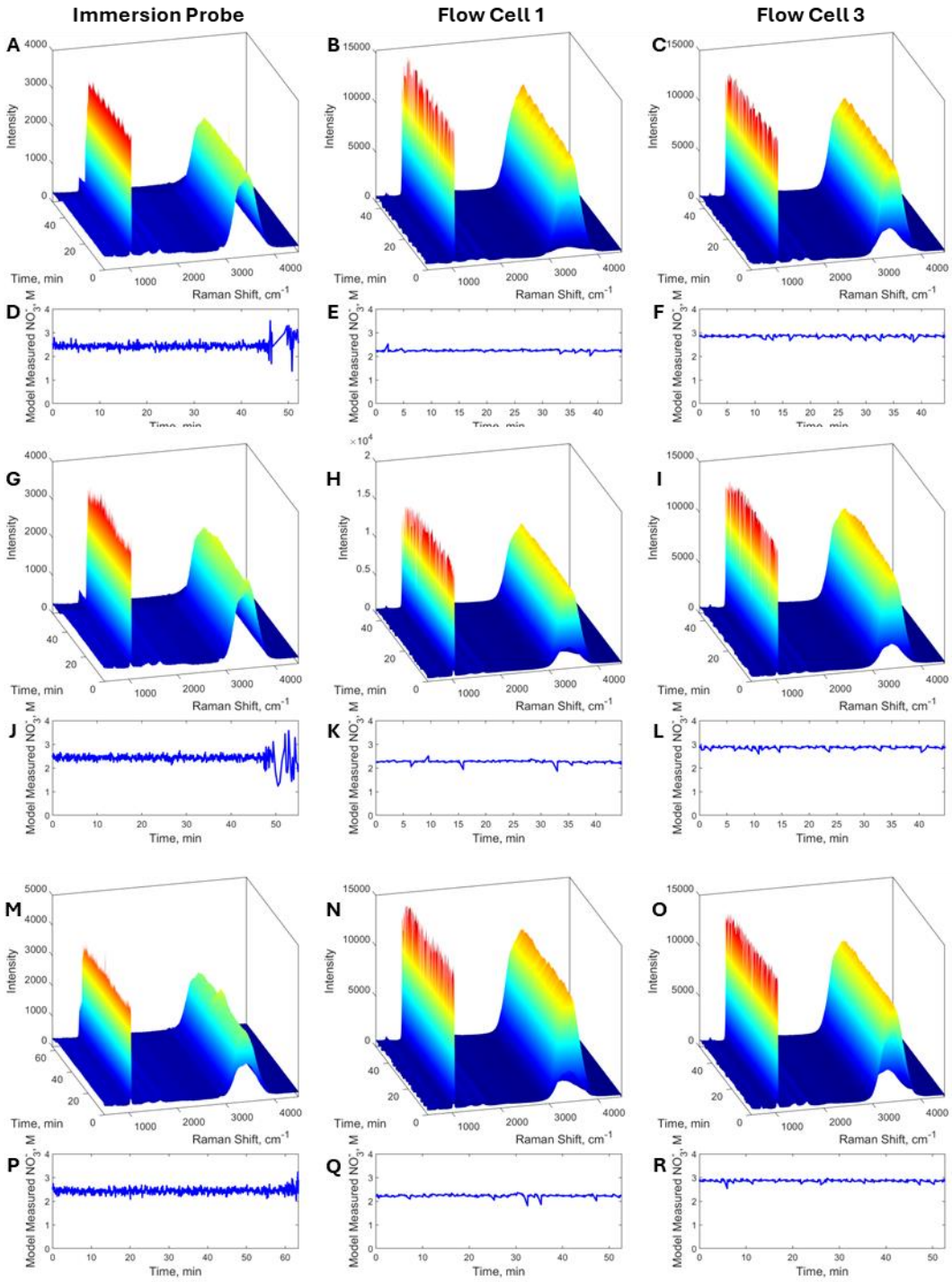


Figure 64. Raman Trial 12: Dilution 2, Full tank transfer, 2.3 Bar, 2.0 Bar, 1.0 Bar

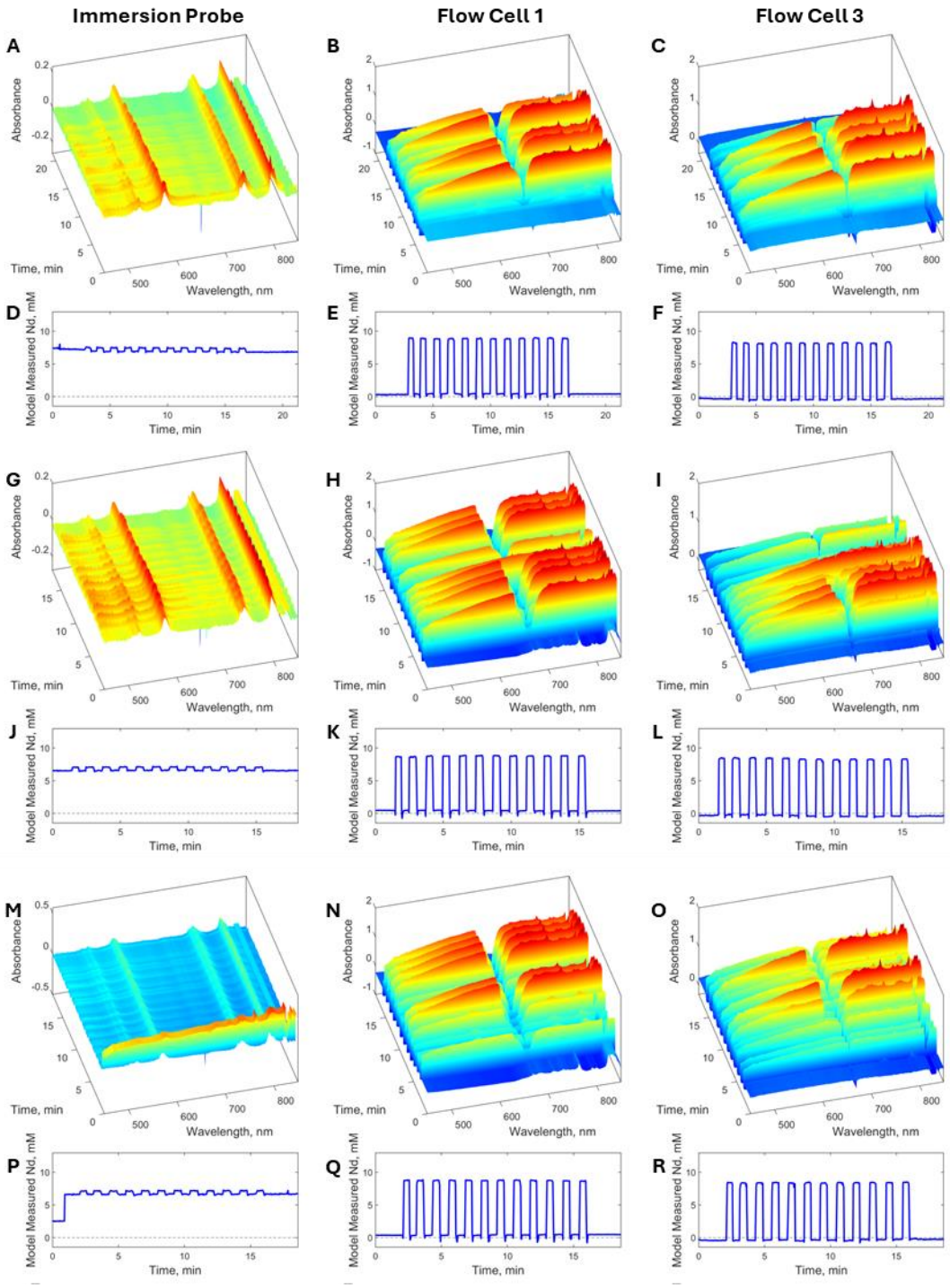


Figure 65. UV-vis Trial 13: Dilution 2, First third tank transfer, 2.3 Bar, 3 replicates

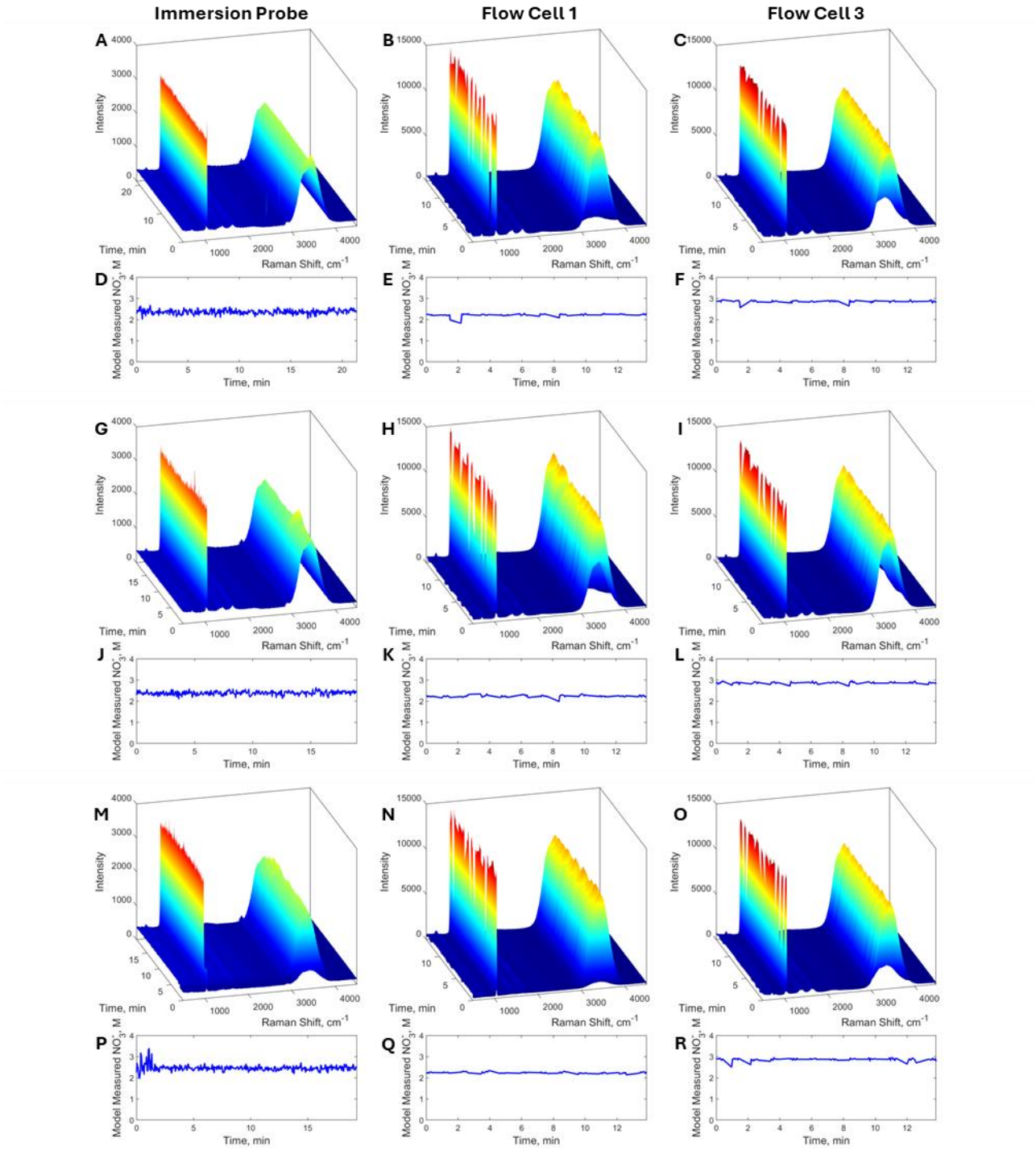


Figure 66. Raman Trial 13: Dilution 2, First third tank transfer, 2.3 Bar, 3 replicates

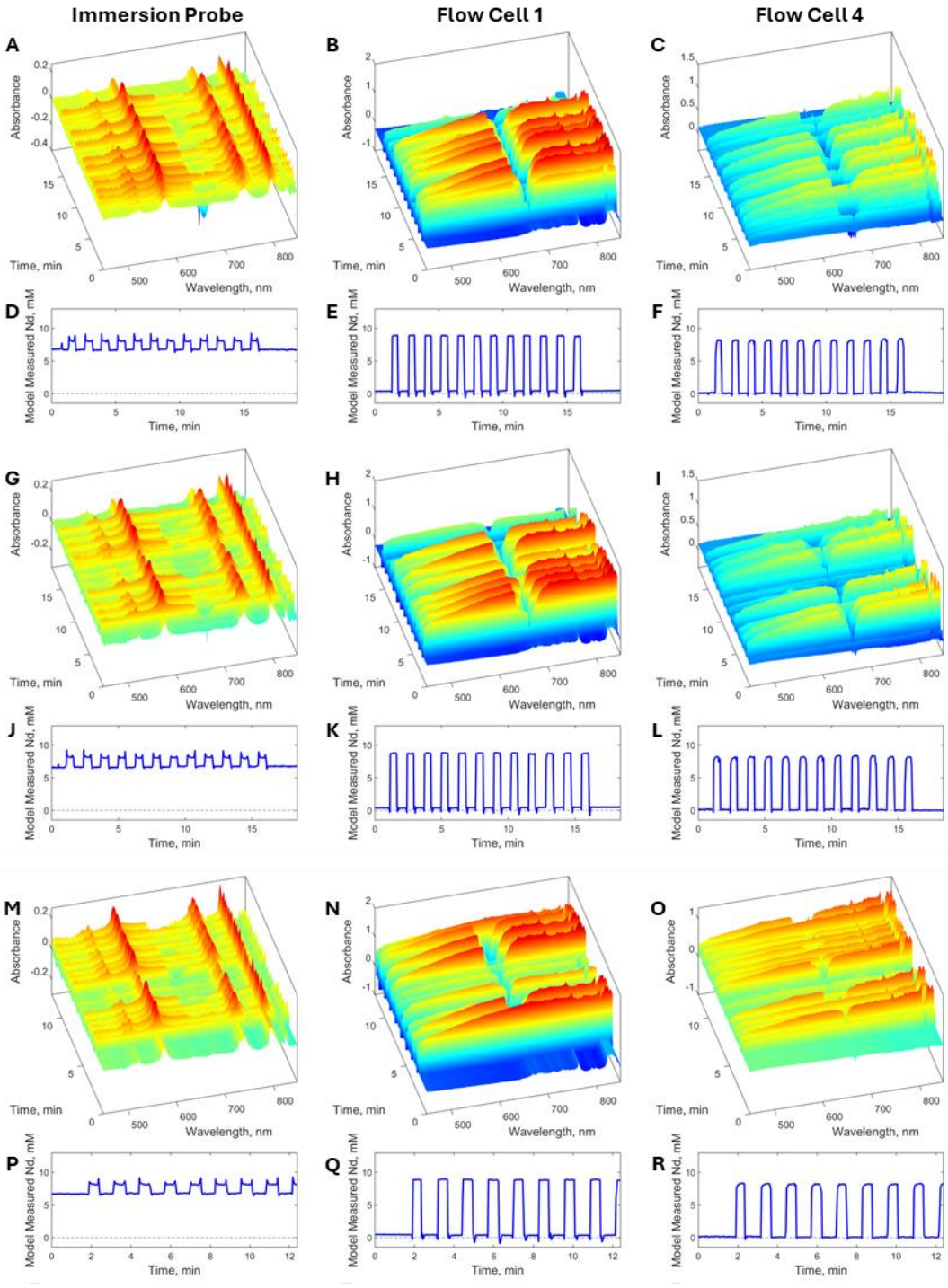


Figure 67. UV-vis Trial 14: Dilution 2, Second third tank transfer, 2.3 Bar, 3 replicates

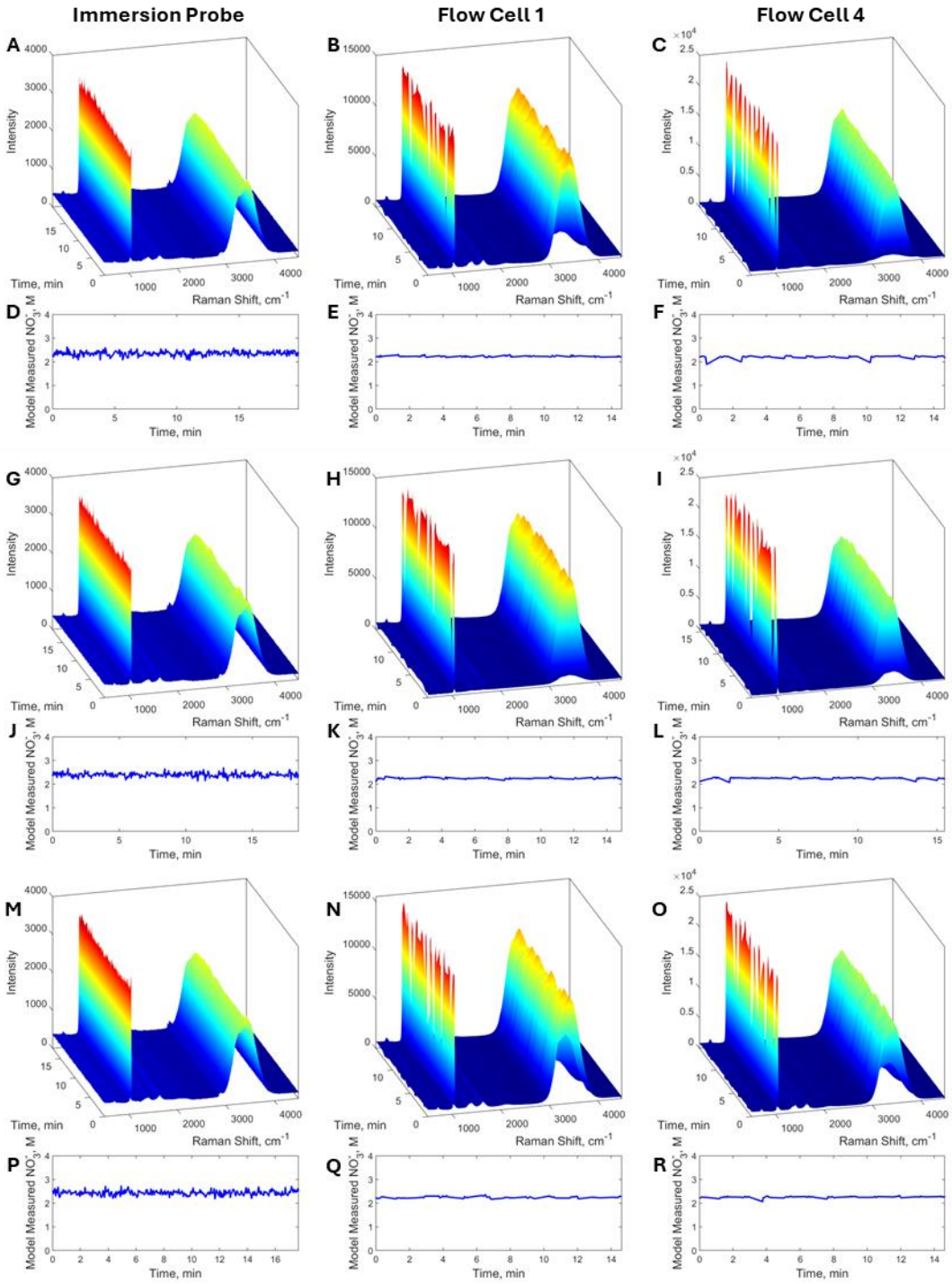


Figure 68. Raman Trial 14: Dilution 2, Second third tank transfer, 2.3 Bar, 3 replicates

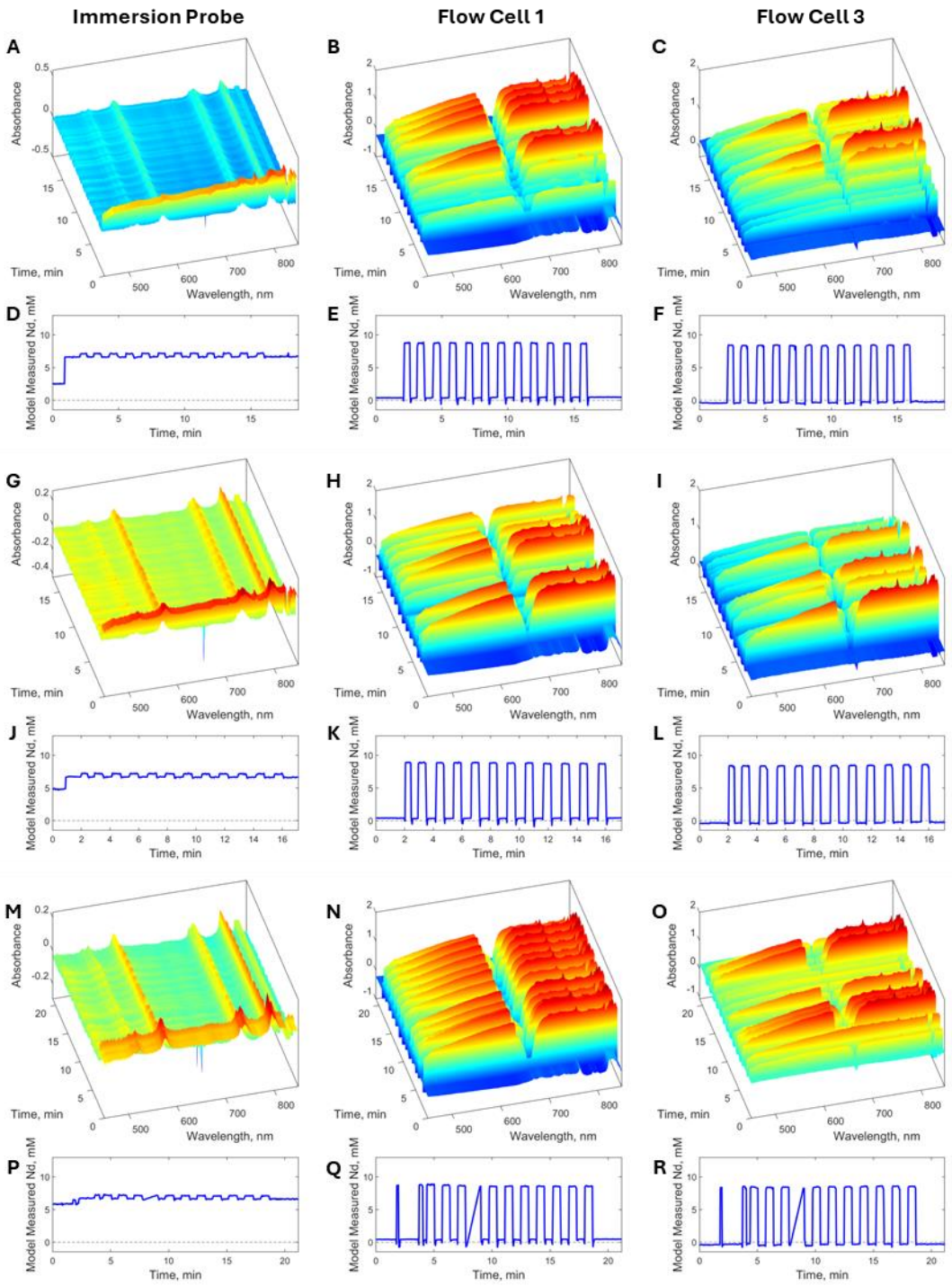


Figure 69. UV-vis Trial 15: Dilution 2, First third tank transfer, 2.3 Bar, 2.0 Bar, 1.0 Bar

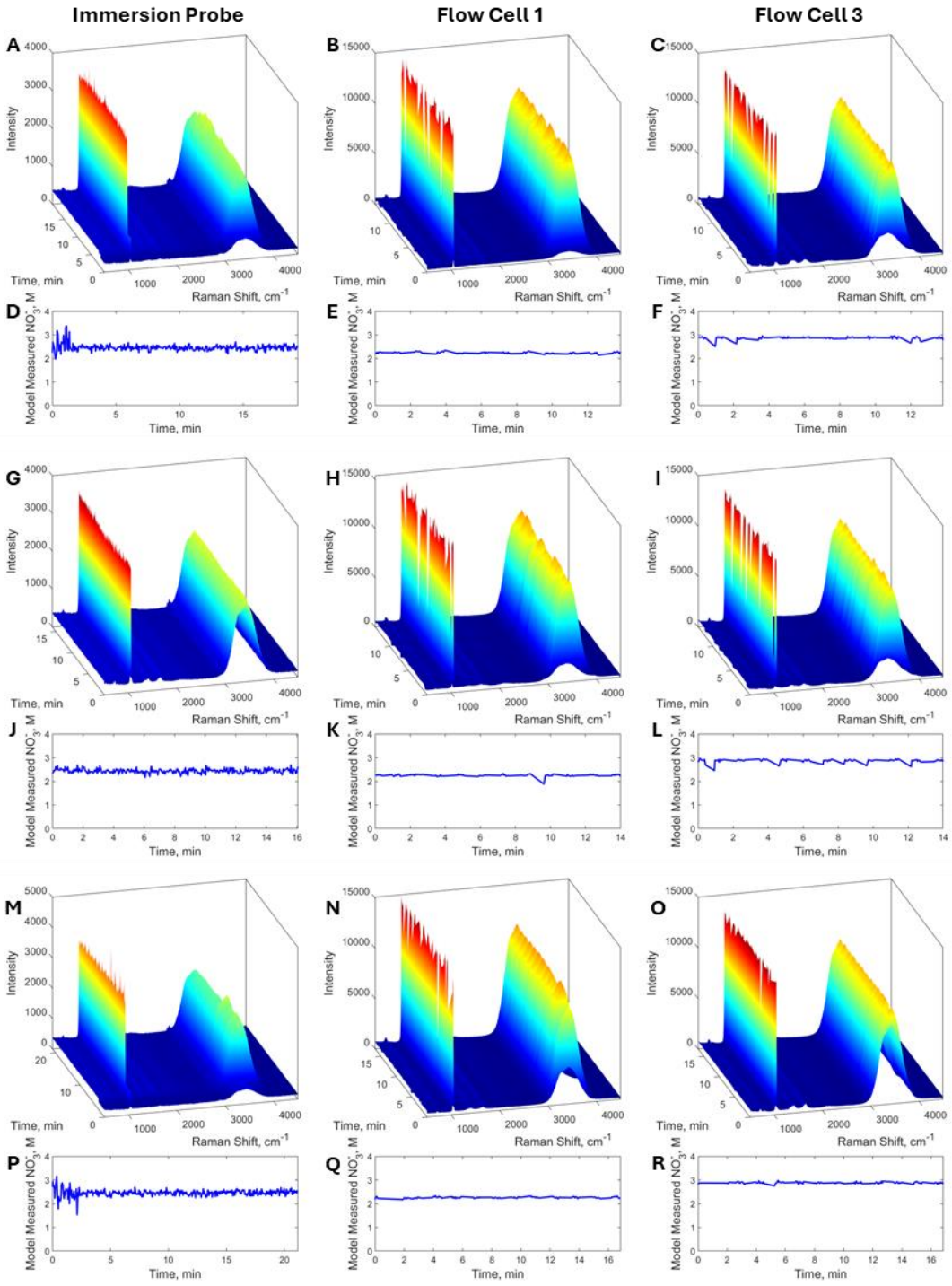


Figure 70. Raman Trial 15: Dilution 2, First third tank transfer, 2.3 Bar, 2.0 Bar, 1.0 Bar

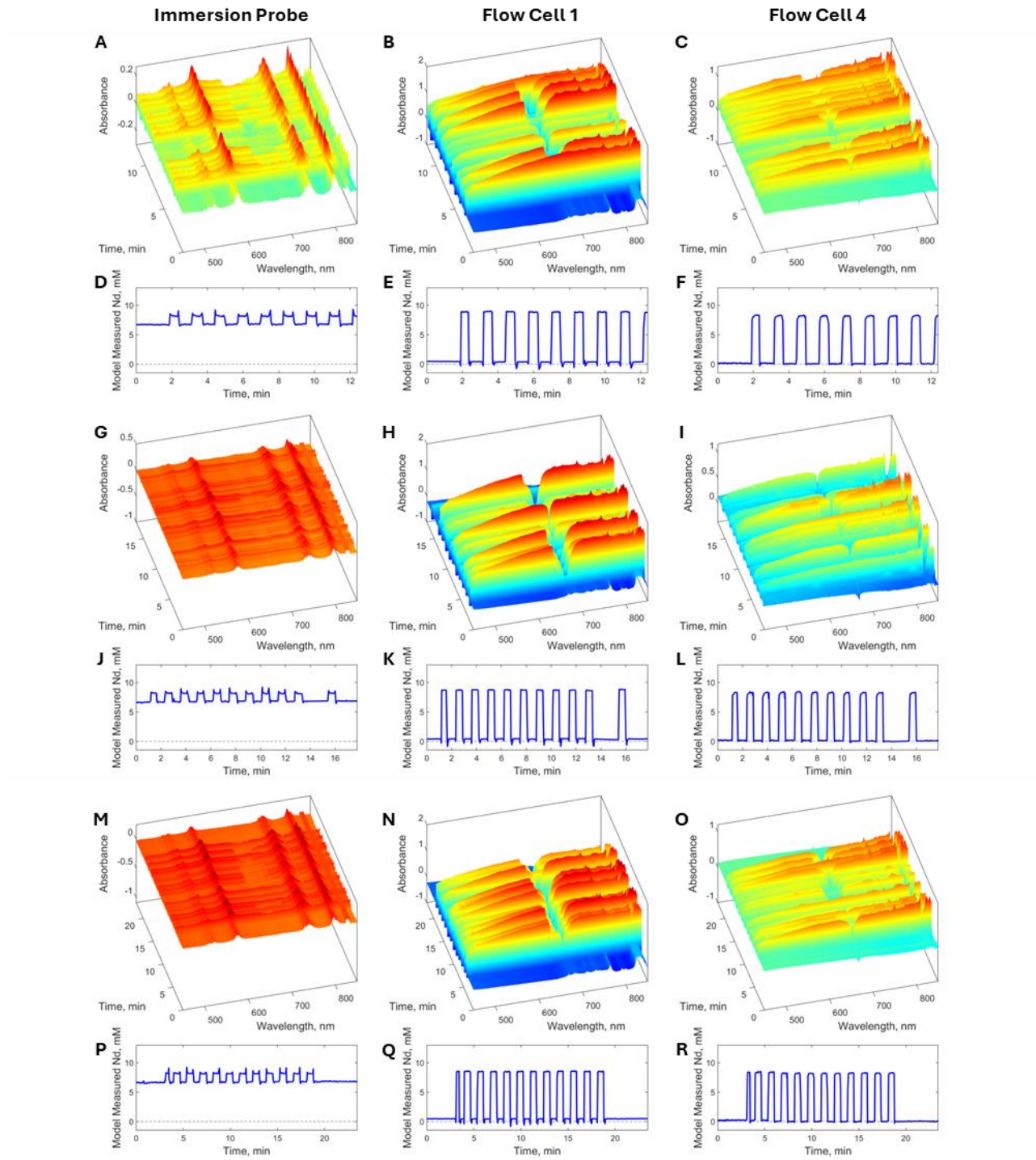


Figure 71. UV-vis Trial 16: Dilution 2, Second third tank transfer, 2.3 Bar, 2.0 Bar, 1.0 Bar

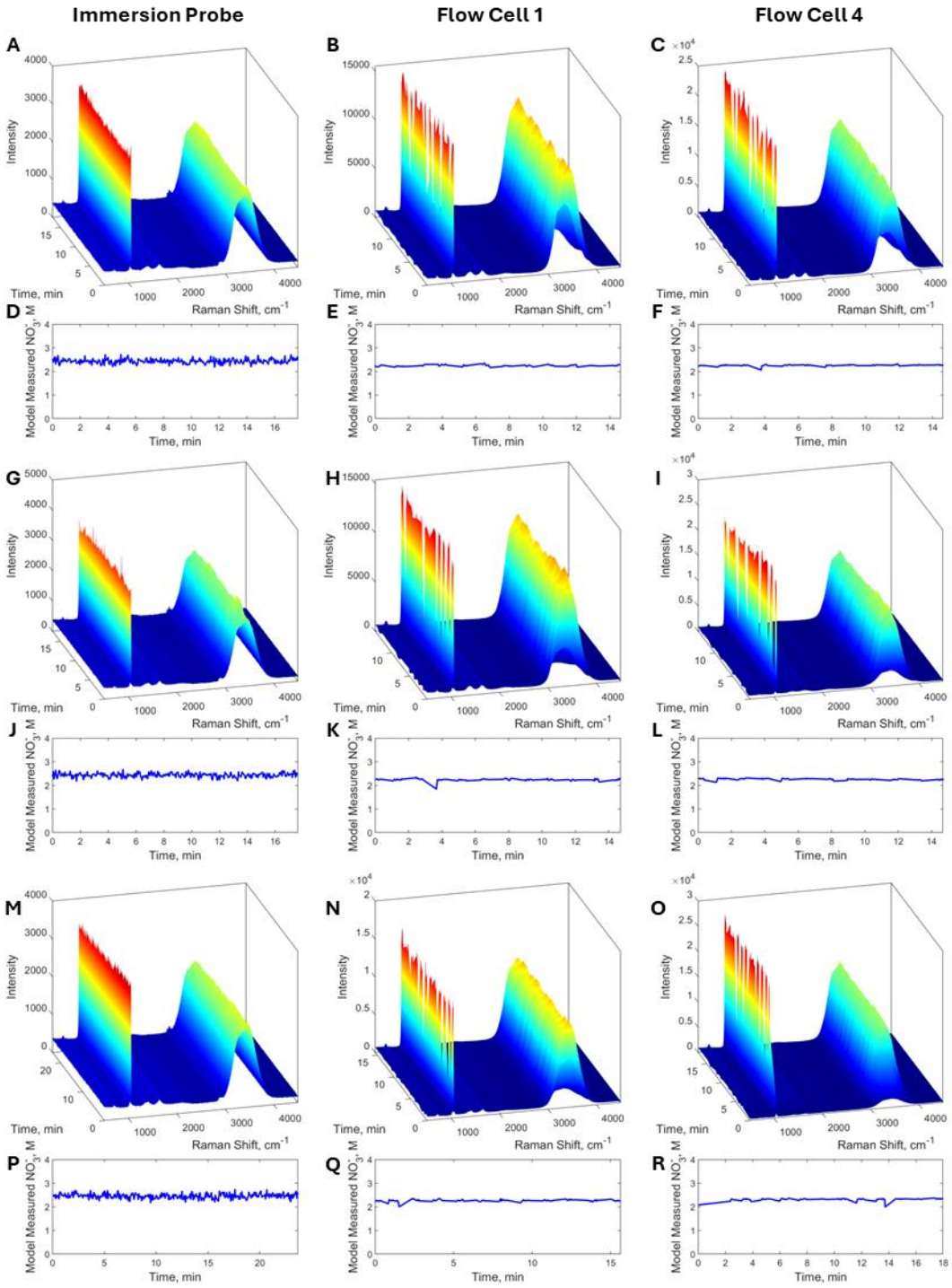


Figure 72. Raman Trial 16: Dilution 2, Second third tank transfer, 2.3 Bar, 2.0 Bar, 1.0 Bar

Appendix B – Additional Uncertainty Analysis

Three sensors (the floor scale under Tank 1, the floor scale under Tank 2, and the Coriolis flowmeter) can each be used to make independent measurements of the total mass transferred. Additionally, any of these measurements can be combined with any other using inverse variance weighting to produce a combined estimate of mass transfer, often with lower uncertainty. Continuing the work of Section 6.4, in this section, using the Trial 3, Replicate 1 as an example, we examine the different methods for measuring mass transfer, and different masks for detecting invalid concentration predictions.

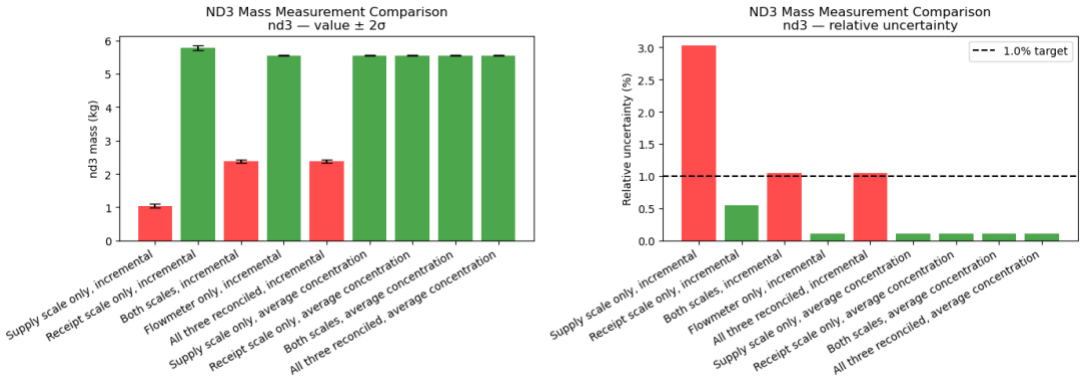


Figure 73. Mass measurement options for Nd^{3+} using the concentration bound and spike mask (left) and associated relative uncertainty (right).

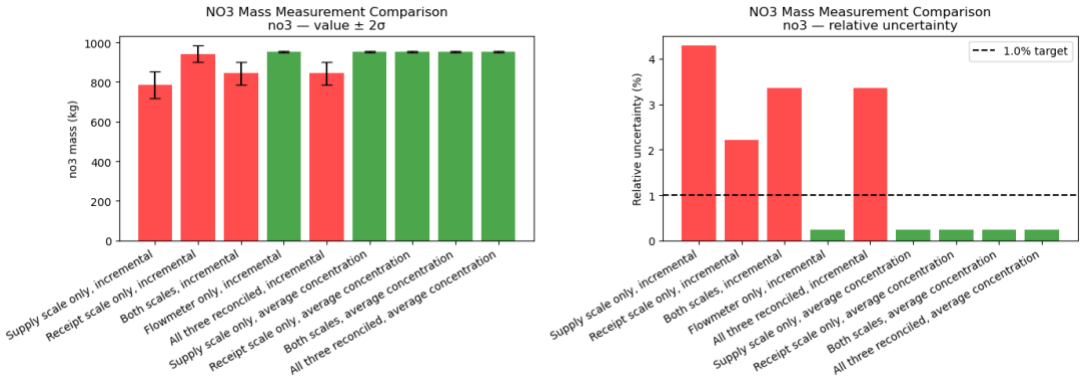


Figure 74. Mass measurement options for NO_3^- using the concentration bound spike mask (left) and associated relative uncertainty (right).

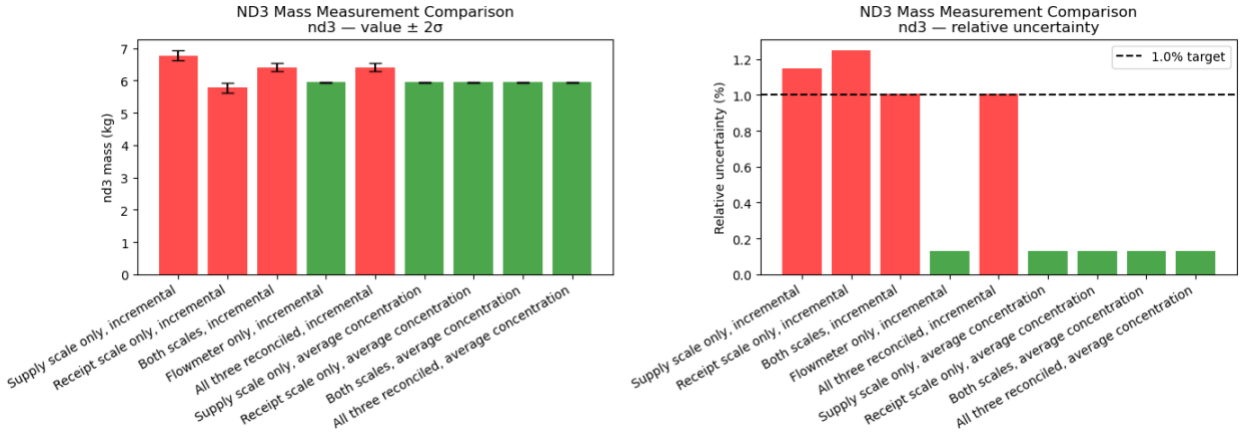


Figure 75. Mass measurement options for Nd^{3+} using the power fluidics phase mask (left) and associated relative uncertainty (right).

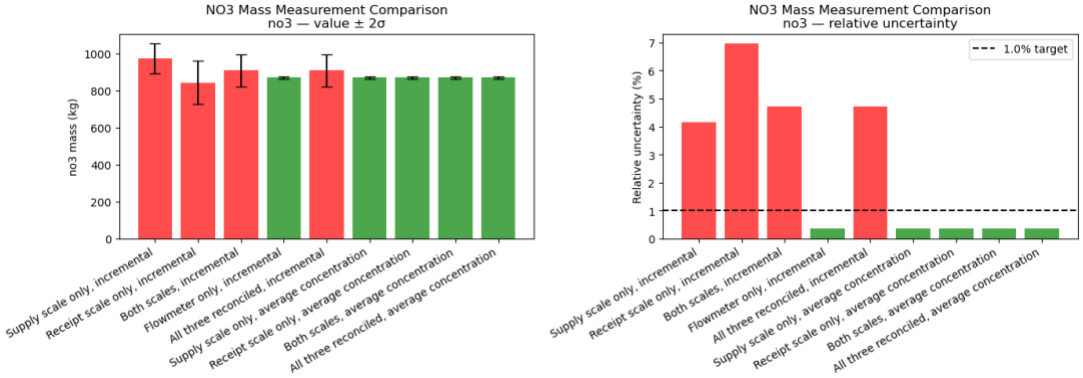


Figure 76. Mass measurement options for NO_3^- using the power fluidics phase mask (left) and associated relative uncertainty (right).

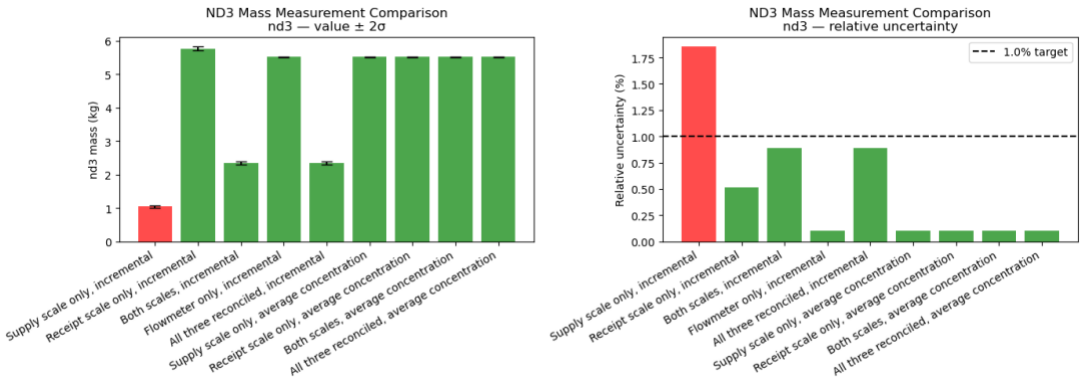


Figure 77. Mass measurement options for Nd^{3+} using the Monte Carlo std. mask (left) and associated relative uncertainty (right).

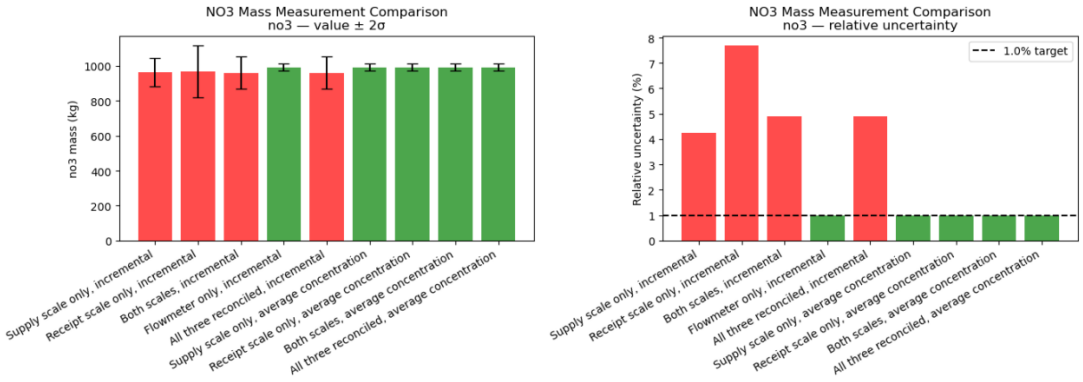


Figure 78. Mass measurement options for NO_3^- using the Monte Carlo std. mask (left) and associated relative uncertainty (right).

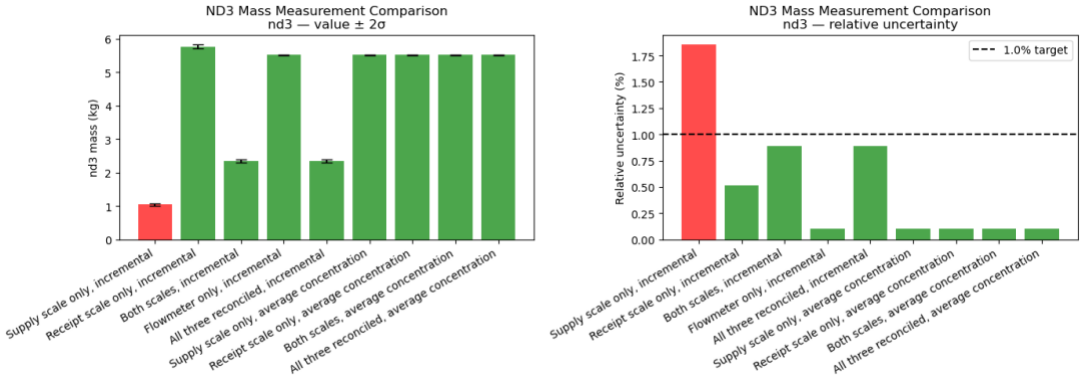


Figure 79. Mass measurement options for Nd^{3+} using the Q-residual threshold mask (left) and associated relative uncertainty (right).

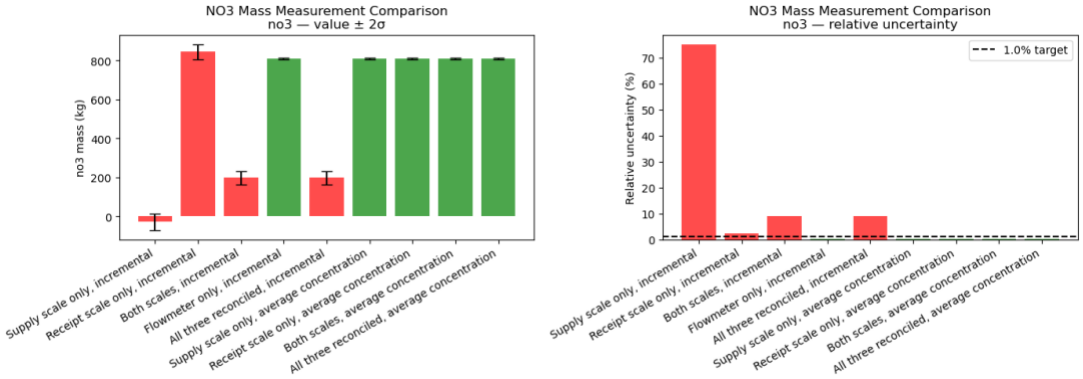


Figure 80. Mass measurement options for NO_3^- using the Q-residual threshold mask (left) and associated relative uncertainty (right).

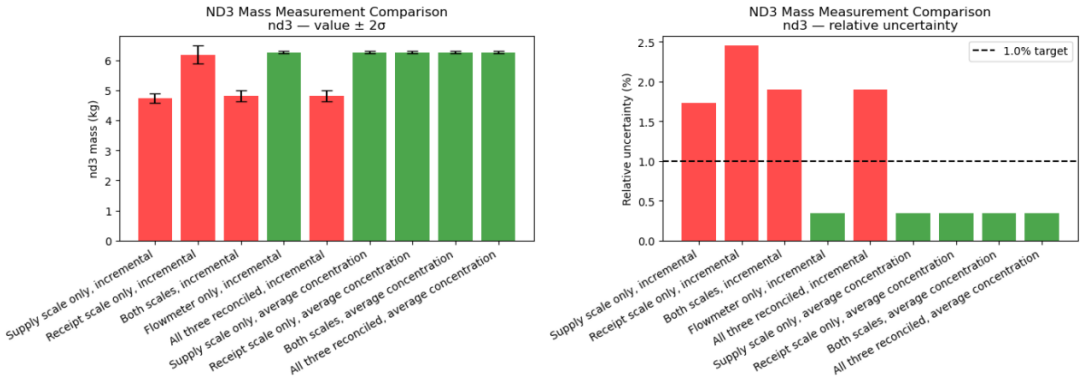


Figure 81. Mass measurement options for Nd^{3+} using the concentration bound, PLS stats, and Monte Carlo std. masks combined (left) and associated relative uncertainty (right).

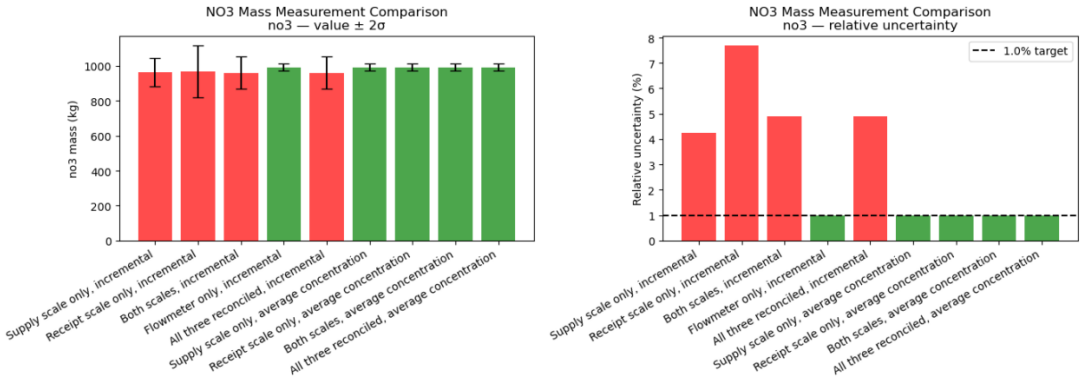


Figure 82. Mass measurement options for NO_3^- using the concentration bound, PLS stats, and Monte Carlo std. masks combined (left) and associated relative uncertainty (right).

Pacific Northwest National Laboratory

902 Battelle Boulevard
P.O. Box 999
Richland, WA 99354

1-888-375-PNNL (7665)

www.pnnl.gov